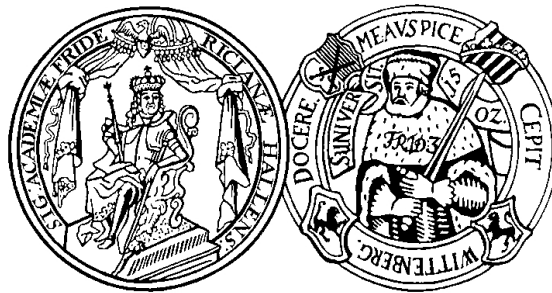# Thermomechanics of photovoltaic modules

Dissertation

zur Erlangung des akademischen Grades
Doktoringenieur (Dr.-Ing.)

vorgelegt dem

Zentrum für Ingenieurwissenschaften
der Martin-Luther-Universität Halle-Wittenberg
als organisatorische Grundeinheit für Forschung und Lehre im Range einer Fakultät
(§ 75 Abs. 1 HSG LSA, § 1 Abs. 1 Grundordnung)

von

Dipl.-Math. techn. Ulrich Eitner
geb. am 01.02.1980 in Meerbusch

1. Gutachter: Herr Prof. Dr.-Ing. habil. Dr.h.c. Holm Altenbach,
                Martin-Luther Universität Halle-Wittenberg

2. Gutachter: Herr Prof. Dr.-Ing. habil. Rolf Brendel,
                Institut für Solarenergieforschung Hameln (ISFH)

Tag der Verteidigung: Montag, 21. März 2011

Contents

Introduction

Motivation

Photovoltaics (PV) is one major pillar in the renewable energy portfolio of wind, water, biomass, solar thermal and geothermal power. Driven by the urgent necessity to reduce CO_2 emissions [84] global energy supply has to be shifted from fossil sources to sustainable energy sources. Political instruments such as feed-in tariffs have been invented and stimulated a vast growth of photovoltaic installations over the past decade, starting from 1.4 GW of world-wide installed power in 2000 to 22.9 GW in 2009 [3].

In order to be able to compete with today's energy production cost there is an ongoing effort in the PV community to reduce the cost per kWh of PV power. The cost of a kWh generated by PV is mainly given by the investment cost of the PV system, its efficiency and its lifetime. As a consequence, the cost may be lowered by reducing the module production cost, by increasing the efficiency of the module and by extending the operational lifetime of the module. Regarding the production on the module level, neither the choice of materials nor the general module concept, which has been developed in the Flat-Plate Solar Array Project [28] in the 1970s and 1980s, has changed since then. However, the cell and the module sizes have grown and the production has reached a high level of automation. The improvement in efficiency is mainly due to the effort made on the cell level. Some manufacturers have also improved the optical properties of the front glass in order to obtain higher conversion levels [13, 86, 88]. The indicator for the lifetime are the warranties that are given by the module manufacturer. They have now reached 25 years on 80% of the module's nominal power (see p.8). This large number is mainly due to continuing reliability studies beginning with modules from early commercial production in the 1980s [132]. As the module design has not significantly changed since then the aging mechanisms are expected to be identical for today's modules. Accelerated aging tests are believed to detect known failures so that manufacturers give promising warranties for their products that passed the qualification testing [7].

Nowadays module manufacturers are confronted with thinner solar cells [133], cells with both contacts at the rear side [23, 69] and the task to further reduce the module cost. In order to face these challenges and maintaining the demanding module warranties at the same time, solutions beyond the conventional module designs have to be explored [12, 33, 45, 46]. In order to assure similar lifetimes for new designs every step in the development process has to be checked with the already existing accelerated aging tests. These tests have emerged from previously observed failures in the field and imitate certain aspects of outdoor exposure [97, 131]. The most critical among these tests are thermal cycling between -40°C and 85°C, mechanical load tests, hail tests and tests involving humidity. Thermal cycling, hail and mechanical load tests adress the thermomechanical stability of the module. It is therefore essential to understand the thermomechanical issues when developing new module concepts or when preparing existing concepts for novel and potentially more fragile cell structures. The mechanical failure of materials is related to mechanical stress or strain, so in order to improve the module design the stress and strain distribution is of primary interest. Even in conventional crystalline modules high mechanical stress may cause cracks in the solar cells or interconnect failures.

Figure 1: Monocrystalline photovoltaic modules.

In microelectronic packaging, a sector where similar materials (silicon, polymers, metals, solders) are used and where challenging mechanical reliability requirements exist (thermal stability, impact resistance, vibration), the experimental and numerical analysis of the thermomechanical behaviour is an integral part in the development process of new products [115, 124, 138]. Although these methods have played a fundamental role in the Flat Plate Solar Array Project between 1976 and 1986 [20, 26, 27, 28], only very recent publications demonstrate their use in the field of PV module engineering. Eikelboom [36] modeled the mechanical behaviour of conductive adhesives for back-contact module concepts. Dietrich [34] set up Finite-Element-models from the cell to the module level in order to identify critical mechanical parameters and to simulate the stress distribution in solar cells after paste firing. We optimized interconnectors for soldered back-contact cells with the help of Finite-Element-simulations [37]. Wiese [128] and Meier [81] focused on the mechanics of copper ribbons by developing a bilinear mechanical material model for the ribbon and simulating it in a laminated module structure. In the development process of back contact modules Gee [47] regards Finite-Element-simulations with appropriate material models as an integral part for the confidence in the reliability of the concept and the ability to maintain the process in production. In general, the quality of the simulation results is highly dependent on an accurate choice of material models and parameters. It is thus necessary to have experimental methods available that verify the simulated data. In the case of thermally induced deformations we successfully applied the technique of digital image correlation [118] to PV module technology [38, 39] where we measured the displacement of the gap between two adjacent solar cells. The same technique was used by Meier [80] to predict the lifetime of a copper ribbon in a PV module. However, there is, to the best of our knowledge, no literature available where the thermal stress and strain distribution is outlined in detail for every material in the module and where reliable and approved material models are used.

This work addresses the determination of thermomechanical stress and strain in the solar module that result from thermal cycling between -40°C and 85°C. Therefore, we rely on the theory of solid mechanics. We model the PV module structure and subject it to a homogeneous temperature profile that corresponds to the thermal cycling norm test. The underlying equations of solid mechanics form a set of partial differential equations that can in general not be solved analytically. We numerically solve our model with the Finite-Element-Method (FEM) which is the state-of-the-art technique in engineering applications for computational mechanical analyses. The simulation model requires the input of material parameters for the front glass, the silicon solar cells, the interconnectors, the back sheet and the polymeric encapsulation material. Furthermore, we perform experiments on specially designed laminates and compare them to simulation data in order to evaluate the quality of the simulation model.

Several questions have to be answered along the path of our solution strategy. What mechanical

tests are convenient to determine the material properties of the polymeric sheets in the module? Do the elastic material properties of crystalline silicon solar cells match the literature data for monocrystalline bulk silicon? Is it sufficient to model all module materials by linear elasticity or do they exhibit dependencies on temperature or on time? Is there an accurate and contactless experimental method to measure the thermal displacements or strains of a solar cell in a laminate? And finally, how stressed are the module materials in a thermal cyling test and is there a dependence on the position in the module?

The principles of photovoltaic energy conversion are considered outside the scope of this work as well as the electrical interconnection concepts for PV modules. This work was carried out at the Institute for Solar Energy Research Hamelin (ISFH) in Emmerthal, Germany.

Structure of the work

Chapter 1 describes a standard crystalline silicon photovoltaic module. The different materials and their function in the module is explained. In addition, we draw special attention to the lamination process. It plays a key role in the mechanical investigation as we use it to define the initial unloaded state of the material assembly. The third section of Chapter 1 gives an insight into commonly reported reliability issues of PV modules. The significance of thermomechanical investigation within the field of reliability issues is given. The accelerated aging tests in the IEC 61215 norm, i.e. thermal cycling, mechanical load test and the hail test, are briefly outlined. We take the thermal cycling test to motivate the detailed analysis of the thermomechanical investigation down to -40°C that follows in the subsequent chapters.

Chapter 2 gives an introduction to the theory of solid mechanics that is necessary to understand the terminology of stress, strain, displacement and temperature. In this chapter the theory is limited to linear elastic material behavior. The basic equations of solid mechanics, i.e. the balance of moment of momentum, the constitutive equations and the compatibility equations, are presented. As the FEM-simulations play a key role in our thermomechanical analysis we illustrate the basic ideas of this powerful numerical tool. For glass, copper and silicon we review linear elastic material data from the literature. A limited number of RISE-EWT solar cells is subjected to 3-point bending experiments to compare the results with silicon literature data. In case of the polymeric materials, i.e. the encapsulant EVA and a PVF-based back sheet, tensile tests at room temperature, 80°C and -40°C (-35°C) are performed. For EVA, the testing results require a further investigation so that a dynamic mechanical analysis (DMA) is carried out over the temperature range from -60°C to 100°C.

Chapter 3 deals with the concept of time-dependent material behavior, so-called viscoelastic materials. It is demonstrated that EVA shows these viscoelastic properties so that relaxation and creep tests at different isothermal temperatures are performed as an experimental basis for a viscoelastic modeling procedure. The viscoelastic concept is introduced step by step leading to a linear viscoelastic constitutive equation which takes an integral form over time. The mechanical parameter relaxation modulus is now a function of time which we approximate by a generalized Maxwell model. However, as the model requires the relaxation modulus in shear, we discuss the concept of interconversion from tensile relaxation and creep data to shear data. This calculation involves an ill-posed formulation, where we propose a regularization method to reduce perturbation. The obtained shear relaxation data are then shifted according to the time-temperature superposition with a Williams-Landel-Ferry (WLF) equation. We determine the parameters G_i and τ_i of the generalized Maxwell model by fitting the model to the shifted mastercurve. To check the accuracy of this time- and temperature-dependent material model for EVA the original relaxation tests are simulated with FEM-software and are compared to the experimental data.

Chapter 4 addresses the thermomechanics of laminated structures and modules. First, the experimental technique of digital image correlation in conjunction with a stereo camera system is introduced to measure the distance of two adjacent laminated solar cells. The experiments include several laminates, all containing 3 solar cells with different interconnection techniques.
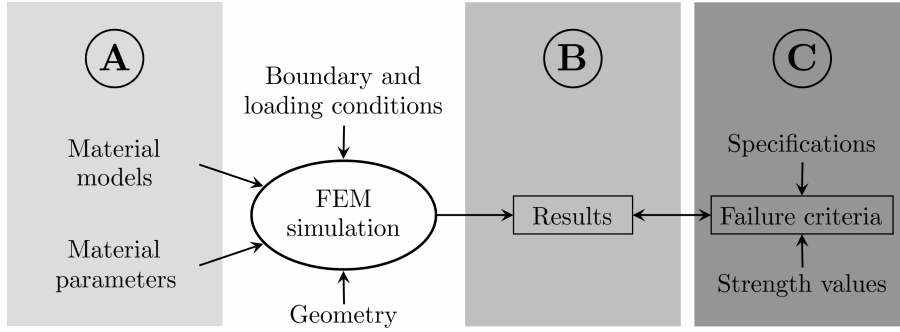
Figure 2: Different types of experiment categories in the context of the simulation.

Furthermore, we measure the gap displacement in a laminate where the float glass is replaced by borosilicate glass. We use the mechanical material parameters determined in Chapters 2 and 3 to simulate the gap displacement experiments with a two-dimensional plane-stress model. The complexity of the material models for silicon and EVA is varied and compared to the experimental results. Furthermore, we determine the impact of a variation of the input parameters by $\pm 10\%$ on the simulation results. The material model that agrees best with the experimental data of the gap displacement measurements is used to simulate the thermomechanics of a frameless PV module without interconnectors. Finally, we discuss the determined stress and strain distributions in the different modules layers.
In **Summary and outlook** we list the key results of this work and propose topics for further investigation.

Context of simulation and experiment

The equations of solid mechanics form a set of partial differential equations on a given subdomain with unique boundary conditions. This class of problems can only be solved analytically for special topologies of the subdomain. Whenever non-trivial subdomain shapes or boundary conditions are given, this set of equations has to be solved numerically. For this reason the FEM analysis is utilized which is implemented in commercial software packages and which is intensively used by engineers throughout all application fields of mechanics. When different material models for EVA are discussed in this work, they affect only one part of the subdomain. Furthermore, the material model is not simulated itself but is part of the set of equations from solid mechanics which is numerically solved as a whole.
The experiments in this work can be divided into two categories of the three categories shown in Fig. 2. The first category (A) contains experiments that determine mechanical properties of individual materials (Chapters 2 and 3). These properties are part of the equations of solid mechanics and have to be be seen as input parameters to the FEM-simulation. The experiments in the second class (B) are used to check the simulated results (Chapter 4). These experiments help to evaluate the accuracy and correctness of the simulation and the underlying material models and parameters. The third category (C) is outside the scope of this work where experiments determine design limits and failure modes.
As mechanical failure is related to stress in the material, and stress cannot be measured directly by the experimental technique presented in Chapter 4, a purely experimental investigation of laminates is not sufficient. The combination of both simulation and experiment is qualified to determine accurate stress values.
The simulations are carried out with the commercially available software packages Comsol Multiphysics and Abaqus. Unless indicated elsewise the mechanical experiments are performed at the facilities of the Institute for Solar Energy Research Hamelin (ISFH).

Chapter 1

Photovoltaic modules

Following the definition given in [119], a photovoltaic (PV) module is the bulding unit for solar generators, which makes a module the PV product that can be purchased in the market. From a technical point of view a solar module is defined as a collection of individual solar cells integrated into a package for environmental protection [59, 97].

PV modules for terrestrial applications are commonly classified in two major groups: crystalline silicon modules and thin film modules. In 2009, the fraction of crystalline silicon modules of the annual production was 78% while thin film modules made 22% of a total module production of 24 GW [3]. Crystalline silicon solar modules are thus the dominating module type and in this work the mechanical investigations are limited to this kind of modules.

The operating principles of solar cells and the photovoltaic conversion of sunlight into electricity are considered outside the scope of this work. The reader is referred to standard text books such as [48, 49, 50, 76]. A detailed description of the electrical principles on the module level is given in [59].

1.1   Structure

Crystalline silicon solar cells are the core of a PV module. These energy conversion units are electrically connected in series with copper ribbons to form so-called strings. The strings are embedded in the encapsulating polymer sheets which bond the strings to a glass superstrate. The rear side of the crystalline silicon modules consists of a polymeric backsheet or, alternatively, of a second glass plate. This general lay-up is illustrated in Fig. 1.1. The focus of this work is on modules with a polymeric back sheet.

Crystalline silicon solar cells

Crystalline silicon solar cells are processed from crystalline silicon wafers with thicknesses between nowadays 140 μm and 240 μm. The processing steps include etching, doping, texturing, screen-printing and firing. A standard solar cell contains a 150 to 350 nm-deep diffusion layer of phosphorus-doped silicon, a passivation layer of silicon nitride of approximately 80 nm thickness, a front surface of 2 to 15 μm-high pyramids, a metalization grid of 15 to 25 μm-thick silver paste at the front and a 25 to 50 μm-thick metallization of aluminum at the back. The thicknesses of these layers are all small compared to the cell thickness, so that from a mechanical point of view monocrystalline cells are here treated as continua whose mechanical properties are expected to match those of monocrystalline silicon. Detailed overviews of solar cell technologies are given in [66, 65].
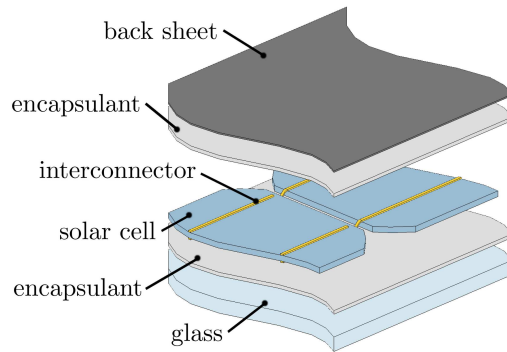
Figure 1.1: Layer structure of a standard PV module

Interconnectors

The interconnectors are copper ribbons that are completely covered with solder material. The ribbons are approximately 130 µm thick and 2 mm wide. The solder coating has a thickness of around 20 µm. Mostly tin-lead solders are used, however legislative restrictions are expected to ban lead in PV modules in the near future so that alternatives such as tin-silver coated copper ribbons have been successfully tested. Depending on the cell design two or three interconnectors are soldered to the front side busbars of the solar cell. These interconnectors lead the electrical current to the back side of the neighboring solar cell. An alternative to soldering is the use of conductive adhesives which has been evaluated by research groups to lower the interconnection temperatures and thereby the thermal stress [12, 36, 33].

Encapsulant

The encapsulation material bonds the different layers of a PV module together. It must provide high optical transmittance, good adhesion to different module materials, adequate mechanical compliance to accomodate stresses induced by differences in thermal expansion coefficients between glass and cells, and electrical insulation [71]. The most commonly used encapsulation sheets are based on ethylene vinyl acetate (EVA) [29, 68]. After lamination EVA is considered an elastomeric material and exhibits the typical material properties of low mechanical stiffness at room temperature and of high yield strain. It features the states of the glassy region at low temperatures and the rubber elastic region at medium to high temperatures. Other materials used for encapsulation are polyvinyl butyral (PVB) or silicone rubbers.

Glass

The glass used for PV modules is typically tempered and has a low iron content with a standard thicknesses of 3.2 mm or 4 mm. The glass provides mechanical rigidity, impact resistance (hail), optical transparency, electrical insulation of the solar cell circuit and outdoor weatherability [71]. The low iron content results in a higher transmittance of sunlight. On the other hand, the passing of ultraviolet sunlight is undesirable as it damages the underlying polymeric encapsulant and thereby leads to increased degradation of the module. The absorption of the short wavelengths is facilitated by doping the glass with cerium [71]. A number of module manufacturers uses glass with a special surface treatment to enhance the optical properties. Similar to the concepts on the cell level, the module glass is either textured [13] or coated with an anti-reflection layer [86, 88]. In this work these treatments are regarded as minor changes in the elastic properties of glass, so that the elasticity of glass as it is discussed in the following chapters remains valid for these structures as well.
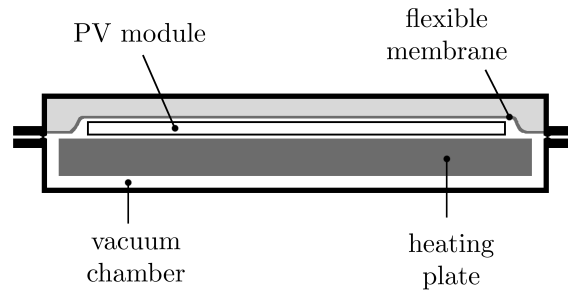
Figure 1.2: Configuration of a laminator for PV module production.

Back sheet

The back sheet is a multilayered polymeric material that has the function to protect the cells and the encapsulant from detrimental environmental influences and to provide electrical insulation and structural support [67]. Moisture permeability is an issue that is highly dependent on the cells' sensitivity to corrosion and the encapsulant's stability under humid conditions at varying temperatures. Therefore, different types of back sheets are available containing polyvinyl fluoride (PVF) layers or a diffusion blocking layer of aluminum. The adhesion to the encapsulating material is important as well as the stability over the PV module's lifetime of the back sheet itself. Compared to a glass cover on the rear side, PVF back sheets are permeable but have the advantage of a much lower weight and can provide a more durable mechanical package as glass-glass modules are susceptible to glass breakage due to edge pinching [63].

1.2 Lamination

The manufacturing of crystalline silicon solar modules consists of two major and critical process steps: stringing and lamination. The other minor steps are cell control and sorting, glass cleaning, framing, junction box mounting, module power inspection and packing [59].
In conventional automated PV module production lines the soldering process is performed by the stringer machine that delivers interconnected solar cell strings [93]. The cells are rigidly coupled to the copper ribbons at elevated temperatures that depend on the soldering temperature (183°C for lead solder Sn63Pb37, 221°C for lead free solders Sn95.5Ag3.8Cu0.7). The different coefficients of thermal expansion of copper and silicon create significant amounts of stress when cooling back to room temperature.
In a subsequent vacuum lamination step the lay-up of glass, encapsulant, solar cell strings, encapsulant and back sheet is bonded together by the curing of EVA at 150°C [94, 95]. Figure 1.2 illustrates the design of a standard laminator for PV modules. During the heating stage the assembly is evacuated in order to press the material layers together and to prevent the formation of voids. At lamination temperature the EVA begins to react from a thermoplastic to an elastomer, i.e. it crosslinks its formerly unconnected polymeric chains to form a wide-meshed network structure [29, 136]. It adheres to the surfaces of the glass, the solar cells and the back sheet. Depending on the particular EVA product it usually takes 7 to 15 min at 150°C to reach a sufficient degree of cure. When the module leaves the laminator it cools down to room temperature building up thermal stresses caused by the discrepancy of the thermal expansion coefficients of the different material layers.
Whenever a module is exposed to mechanical or thermal loads either during qualification testing or under operating conditions in the field the initial state at room temperature is not stress free but charged with intrinsic stress which results from the lamination process. For investigations of mechanical stress and strain it is therefore adequate to set the initial stress-free condition to the lamination temperature. Throughout this work the stress-free initial state is always set to 150°C.

1.3   Reliability and aging effects

Today's crystalline PV modules are sold with warranties that guarantee a power loss of less than 10% after 10 or 12 years and at most 20% loss in power after 20 or 25 years of operation in the field[1]. Module manufacturers and researchers work towards the goal of even higher lifetimes to make PV power more cost efficient. The longer a module produces electricity in the field the lower becomes the cost per generated kWh as the cost of a PV system is mainly given by the inital prize of the PV system. As modules cannot be tested under real conditions for 25 years until they enter the market, a number of accelerated aging tests were designed since the late 1970's [97] that have lead to today's qualification test standard IEC 61215 [1]. A module can either 'pass' or 'fail' the qualification tests but the result only accesses the manufacturing quality and the intial performance of a product [131]. The passing of the qualification does not predict a module's lifetime nor does it identify the weak points in the modules design, for example the failure mode at the end of its lifetime. However, the tests have been invented to reproduce module failure previously observed in the field so that negative results reveal a high probability of failure due to a known mechanism [133]. On the other hand it is probable that modules with standard design and a positive qualification test result will perform well in the field. With changing module design due to cost reduction the qualification sequence needs to be continuously adapted. However, for a first evaluation of new ideas in the process of module research the standard tests can already give a first insight into possible weak points of the tested concepts.

Accelerated aging tests

The accelerated aging tests in the IEC 61215 qualification test sequence [1] comprise a hot-spot enduring test, a UV-preconditioning test, thermal cycling, humidity freeze, damp heat, a mechanical load test and a hail test to imitate long-term outdoor exposure [7] in various climates. The tests that address mechanical issues are the mechanical load test, the thermal cycling test and the hail test.
The idea of the mechanical load test is to determine the module's ability to withstand wind, snow, static or ice loads. The module is first loaded with 2400 Pa for 1 h on the front glass and afterwards for 1 h from the rear side. The loading is repeated 3 times. Alternatively, the module is loaded with 5400 Pa at the last pressure load cycle to be then qualified for harsh snow and ice conditions. In the temperature cycling test a module is exposed to temperatures between 85°C and -40°C as shown in Fig. 1.3. During temperatures above 25°C the maximum current flows through the module. The temperature cycle is repeated for 200 cycles.
The hail test is performed with ice balls of specified diameters between 12.5 mm to 75 mm that are shot onto several positions of the module glass surface with velocities between 16 m/s to 39.5 m/s. The positions are close to the module edges, module corners and cell edges near an electrical joint. The tests are 'passed' if the module remains operational during the tests, the degradation after the tests is less than 5% power loss, the module does not exhibit visible damage and the electrical insulation remains unaffected.

Mechanical failure

The harmful influences that are responsible for failure of PV modules are corrosion of materials (especially metals), water-vapor intrusion, delamination of encapsulant materials, physical damage

---

[1]Warranties retrieved from websites of selected manufacturers (November 22, 2010):
10%/10yrs, 20%/20yrs: Sanyo, Kyocera
 10%/10yrs, 20%/25yrs: Bosch Solar, aleo, Solon, Trina Solar, Qcells, Yingli
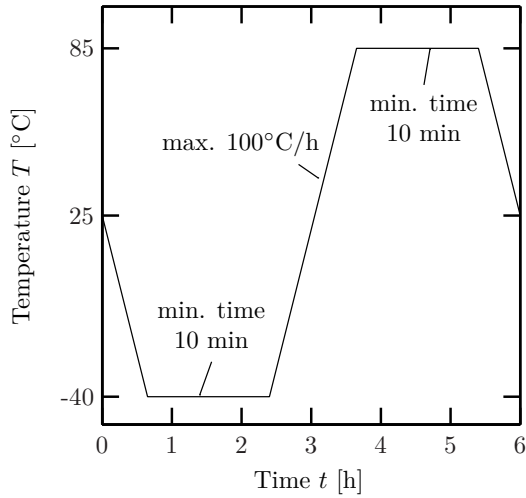10%/12yrs, 20%/25yrs: Solarwatt, Sunpower, Suntech, Solarworld

Figure 1.3: One cycle of the temperature cycling test according to IEC 61215

from wind, hail and installation, thermal excursions due to thermal expansion mismatches, ultraviolet radiation and deterioration of or damage to external components such as junction boxes, wiring and frames [97]. While the problems of corrosion, water intrusion, delamination and UV damage can be eliminated or reduced with a proper choice of metallization layers, polymer materials and glass additives, the thermal mismatch problems and the physical damage factors remain a problem of the combination of materials with different mechanical properties. The mechanical stability of the whole package can only be maintained if the stress due to thermal changes and mechanical loads remains under the limits of the materials' strengths. The magnitude of those stresses derives from the geometrical design of the module, the rigidity of the layers in the module and the interconnection technique. The module designer must therefore carefully address the mechanical issues and needs to know how the stress levels change when layer thicknesses or sizes are modified.

Recent developments lead to thinner cells that must be embedded in modules without increasing the risk of cracks in the cells [133]. Another type of back contact cells, the metal-wrap-though (MWT) cells [23, 69], are about to enter mass production and conformable module concepts are under investigation [33, 46]. The pressure of cost reduction questions the use the well-established encapsulation [68] and back sheet materials [67]. The desire to reduce weight may lead to thinner glass [125]. The expensive aluminum frame may be omitted or replaced by a plastic support construction [2].

All these examples demonstrate that a detailed analysis of the thermomechanical stability and the understanding of stress build up is highly relevant for the module design and the module manufacturing process.

Chapter 2

Linear elastic thermomechanics

2.1 Theoretical basics

The theory of solid mechanics relates displacements, mechanical stresses and strains of a deformable body. Almost every basic textbook in the field of mechanics contains a detailed description of these relations, for example the books from Altenbach [4, 5], Balke [9], Bower [14], Castro [32], Greve [53], Gross [54, 55, 56], Noda [91], Słuzalec [111, 112] or Wriggers [134]. This section consists of a condensed version of the discussion given in [6]. Vectors and tensors are written in bold type.

2.1.1 Displacement and deformation gradient

The deformation of a body is illustrated in Fig. 2.1. In the unloaded reference configuration the position vector $\boldsymbol{r}$ to a material point p in the body is given by

$$\boldsymbol{r}(x_1, x_2, x_3) = x_1\,\boldsymbol{e}_1 + x_2\,\boldsymbol{e}_2 + x_3\,\boldsymbol{e}_3$$

in the cartesian coordinate system $\boldsymbol{e}_1, \boldsymbol{e}_2, \boldsymbol{e}_3$. In a deformed state the point p is translated to p'. The new position is expressed by the vector $\boldsymbol{R}$ so that the displacement vector $\boldsymbol{u}$ becomes

$$\boldsymbol{u}(x_1, x_2, x_3) = \boldsymbol{R}(x_1, x_2, x_3) - \boldsymbol{r}(x_1, x_2, x_3).$$

A small line element $d\boldsymbol{r}$ in the initial configuration is written as

$$d\boldsymbol{r} = dx_1\,\boldsymbol{e}_1 + dx_2\,\boldsymbol{e}_2 + dx_3\,\boldsymbol{e}_3$$

and is transformed to $d\boldsymbol{R}$ in the deformed configuration. Since

$$d\boldsymbol{R} = \frac{\partial \boldsymbol{R}}{\partial x_1}\,dx_1 + \frac{\partial \boldsymbol{R}}{\partial x_2}\,dx_2 + \frac{\partial \boldsymbol{R}}{\partial x_3}\,dx_3$$

and

$$dx_1 = d\boldsymbol{r} \cdot \boldsymbol{e}_1, \qquad dx_2 = d\boldsymbol{r} \cdot \boldsymbol{e}_2, \qquad dx_3 = d\boldsymbol{r} \cdot \boldsymbol{e}_3,$$

we obtain

$$
\begin{aligned}
d\boldsymbol{R} &= d\boldsymbol{r} \cdot \boldsymbol{e}_1 \frac{\partial \boldsymbol{R}}{\partial x_1} + d\boldsymbol{r} \cdot \boldsymbol{e}_2 \frac{\partial \boldsymbol{R}}{\partial x_2} + d\boldsymbol{r} \cdot \boldsymbol{e}_3 \frac{\partial \boldsymbol{R}}{\partial x_3} & (2.1)\\
&= d\boldsymbol{r} \cdot \left[\boldsymbol{e}_1 \otimes \frac{\partial \boldsymbol{R}}{\partial x_1} + \boldsymbol{e}_2 \otimes \frac{\partial \boldsymbol{R}}{\partial x_2} + \boldsymbol{e}_3 \otimes \frac{\partial \boldsymbol{R}}{\partial x_3} \right]. & (2.2)
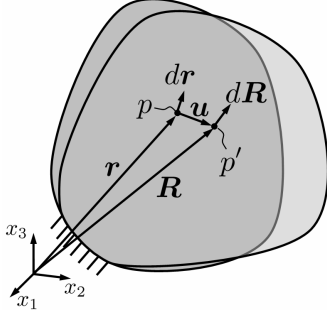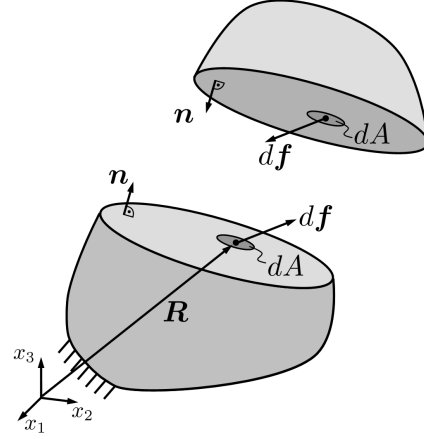\end{aligned}
$$

Figure 2.1: Deformation of a body.

Figure 2.2: Derivation of the stress tensor in the material point p' of a deformed body.

The tensor

$$\boldsymbol{F} := \left[\boldsymbol{e}_1 \otimes \frac{\partial \boldsymbol{R}}{\partial x_1} + \boldsymbol{e}_2 \otimes \frac{\partial \boldsymbol{R}}{\partial x_2} + \boldsymbol{e}_3 \otimes \frac{\partial \boldsymbol{R}}{\partial x_3} \right]^T = (\nabla \boldsymbol{R})^T$$

is called deformation gradient and relates $d\boldsymbol{R}$ to $d\boldsymbol{r}$, i.e.

$$d\boldsymbol{R} = \boldsymbol{F} \cdot d\boldsymbol{r}.$$

From the definition of displacement (Eq. (2.1.1), Fig. 2.1) follows

$$\boldsymbol{F} = \boldsymbol{I} + (\nabla \boldsymbol{u})^T,$$

where $\boldsymbol{I}$ denotes the unit tensor. The deformation gradient is used to define the strain in a body.

2.1.2 Stress and strain

The strain tensor

Different definitions for the strain tensors exist, here we introduce the Green-Lagrangian strain tensor $\boldsymbol{G}$, which is defined as

$$\boldsymbol{G} = \frac{1}{2} \left(\boldsymbol{F}^T \cdot \boldsymbol{F} - \boldsymbol{I} \right) = \frac{1}{2} \left(\nabla \boldsymbol{u} + (\nabla \boldsymbol{u})^T + (\nabla \boldsymbol{u})^T \cdot (\nabla \boldsymbol{u}) \right).$$

For infinitesimal deformations, i.e. $\|\boldsymbol{u}\| \ll 1$ and $\|\nabla \boldsymbol{u}\| \ll 1$, we can neglect the quadratic term in $\boldsymbol{G}$ and obtain the infinitesimal strain tensor $\boldsymbol{\varepsilon}$,

$$\boldsymbol{\varepsilon} = \frac{1}{2} \left(\nabla \boldsymbol{u} + (\nabla \boldsymbol{u})^T \right). \tag{2.3}$$

The strain tensor consists of 3×3 components and is symmetric, $\boldsymbol{\varepsilon} = \boldsymbol{\varepsilon}^T$. The components on the diagonal of $\boldsymbol{\varepsilon}$ are called normal strains, the non-diagonal elements are called shear strains. Positive normal strain values indicate a stretching of the body in that direction, negative strains describe compression. Strains are dimensionless quantities.

The stress tensor

Fig. 2.2 shows a free cut through a deformed body. The force $d\boldsymbol{f}$ imitates the mechanical effect of the counterpart acting on the infinitesimal area dA of the cutting plane. The orientation of dA is characterized by the normal vector $\boldsymbol{n}$. The mechanical stress $\boldsymbol{\sigma_n}$ on dA is defined as

$$\boldsymbol{\sigma_n} = \frac{d\boldsymbol{f}}{dA}$$

and is assumed to be constant over dA. The stress tensor $\boldsymbol{\sigma}$ is introduced by

$$\boldsymbol{\sigma_n} = \boldsymbol{n} \cdot \boldsymbol{\sigma}$$

and it holds

$$\boldsymbol{\sigma} = \boldsymbol{e}_1 \otimes \boldsymbol{\sigma_{e_1}} + \boldsymbol{e}_2 \otimes \boldsymbol{\sigma_{e_2}} + \boldsymbol{e}_3 \otimes \boldsymbol{\sigma_{e_3}}.$$

The stress in p' on an infinitesimal surface with arbitrary orientation can now be computed from the stress tensor for p'. Identical to the strain tensor, the stress tensor consists of 3×3 components and is symmetric. The components on the diagonal of $\boldsymbol{\sigma}$ are called normal stresses, the non-diagonal elements are called shear stresses. Positive normal stress values indicate a loading of the body in tension in that direction, negative stresses describe compression. Stress has the unit Pascal, $Pa = N/m^2$.

Principal stresses and strains

For every stress tensor there exists a set of normal vectors $\boldsymbol{n}$ so that the corresponding stresses $\boldsymbol{\sigma_n}$ point in the $\boldsymbol{n}$-direction. For such a vector $\boldsymbol{n}$, it holds

$$\lambda\boldsymbol{n} = \boldsymbol{n} \cdot \boldsymbol{\sigma}. \tag{2.4}$$

λ is the value of the corresponding normal stress. There exist three perpendicular solutions $\boldsymbol{n}_I, \boldsymbol{n}_{II}, \boldsymbol{n}_{III}$. The corresponding normal stress values $\sigma_I, \sigma_{II}, \sigma_{III}$ are named principal stresses with the convention $\sigma_I \geq \sigma_{II} \geq \sigma_{III}$.
Equation (2.4) belongs to the class of eigenvalue problems and can be solved by satisfying

$$\det\left(\boldsymbol{\sigma} - \lambda\boldsymbol{I}\right) = 0 \tag{2.5}$$

or the equivalent formulation

$$\lambda^3 - I_1\lambda^2 + I_2\lambda - I_3 = 0.$$

The tensor invariants I_1, I_2 and I_3 are given by

$$
\begin{aligned}
I_1 &= \text{tr}(\boldsymbol{\sigma}) = \sigma_{11} + \sigma_{22} + \sigma_{33} \\
&= \sigma_I + \sigma_{II} + \sigma_{III},
\end{aligned}
$$

$$
\begin{aligned}
I_2 &= \det\begin{bmatrix} \sigma_{11} & \sigma_{12} \\ \sigma_{12} & \sigma_{22} \end{bmatrix} + \det\begin{bmatrix} \sigma_{22} & \sigma_{23} \\ \sigma_{23} & \sigma_{33} \end{bmatrix} + \det\begin{bmatrix} \sigma_{11} & \sigma_{13} \\ \sigma_{13} & \sigma_{33} \end{bmatrix} \\
&= \sigma_I\,\sigma_{II} + \sigma_{II}\,\sigma_{III} + \sigma_I\,\sigma_{III},
\end{aligned}
$$

$$
\begin{aligned}
I_3 &= \det(\boldsymbol{\sigma}) \\
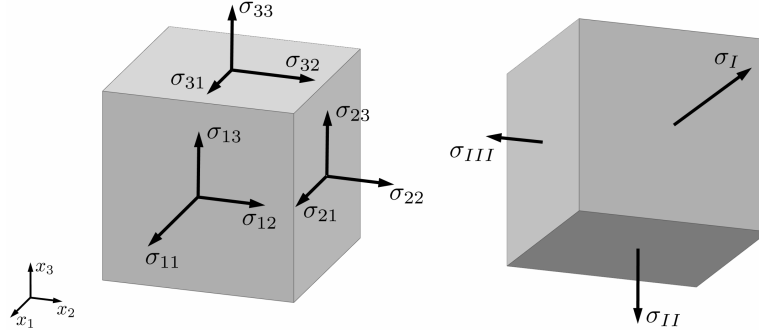&= \sigma_I\,\sigma_{II}\,\sigma_{III}.
\end{aligned}
$$

13

Figure 2.3: Illustration of the Cauchy stress tensor (left) and the principal stresses (right).

Once the principal stresses σ_I, σ_{II} and σ_{III} are determined, the principal directions are calculated by solving the linear systems

$$
\begin{aligned}
(\boldsymbol{\sigma} - \sigma_I \boldsymbol{I}) \cdot \boldsymbol{n}_I &= \boldsymbol{0}, \\
\boldsymbol{n}_I \cdot \boldsymbol{n}_I &= 1,
\end{aligned}
$$

$$
\begin{aligned}
(\boldsymbol{\sigma} - \sigma_{II} \boldsymbol{I}) \cdot \boldsymbol{n}_{II} &= \boldsymbol{0}, \\
\boldsymbol{n}_{II} \cdot \boldsymbol{n}_{II} &= 1,
\end{aligned}
$$

$$
\begin{aligned}
(\boldsymbol{\sigma} - \sigma_{III} \boldsymbol{I}) \cdot \boldsymbol{n}_{III} &= \boldsymbol{0}, \\
\boldsymbol{n}_{III} \cdot \boldsymbol{n}_{III} &= 1.
\end{aligned}
$$

The additional normalizing equations are necessary to obtain unique solutions for $\boldsymbol{n}_I$, $\boldsymbol{n}_{II}$ and $\boldsymbol{n}_{III}$ as eq. (2.5) implies non-uniqueness of $(\boldsymbol{\sigma} - \lambda \boldsymbol{I}) \cdot \boldsymbol{n} = \boldsymbol{0}$ [6, 70]. The procedure applies equivalently for the principal strains ε_I, ε_{II} and ε_{III}.

2.1.3 Temperature

Materials expand when they are heated and contract when being cooled. The material parameter that describes this behavior is the coefficient of thermal expansion α (CTE, unit 1/K). The unconstrained purely thermal deformation of a body over a temperature range $\Delta T = T - T_{\text{ref}}$ affects only the normal strains and is given by

$$
\boldsymbol{\varepsilon}_{\text{th}} = \alpha \, \Delta T \, \boldsymbol{I}.
$$

If a body is mechanically deformed and heated, the resulting strain tensor consists of the purely mechanical and the purely thermal fraction and it holds

$$
\boldsymbol{\varepsilon} = \boldsymbol{\varepsilon}_{\text{mech}} + \boldsymbol{\varepsilon}_{\text{th}} = \boldsymbol{\varepsilon}_{\text{mech}} + \alpha \, \Delta T \, \boldsymbol{I}.
$$

2.1.4 Governing equations of solid mechanics

The equations of solid mechanics consist of the kinematic compatibility equation, the balance of moment of momentum and the constitutive equation.

The kinematic compatibility equation

The kinematic compatibility equation relates displacement to strain. It has already been introduced by the definition of the infinitesimal strain tensor in Eq. (2.3),

$$\boldsymbol{\varepsilon} = \frac{1}{2}\left(\nabla\boldsymbol{u} + (\nabla\boldsymbol{u})^T\right).$$

Balance of moment of momentum

The balance of moment of momentum implies that the time derivative of the moment of momentum equals the sum of volumetric and external forces on an arbitrary subdomain of a deformed body. Let Ω denote the subdomain, $\partial\Omega$ the surface of the subdomain, ρ the density, $\boldsymbol{v}$ the velocity field ($\boldsymbol{v} = d\boldsymbol{u}/dt$), $\rho\boldsymbol{b}$ the internal forces acting on Ω and $\boldsymbol{\sigma_n}$ the external forces acting on $\partial\Omega$. Then, the balance of moment of momentum becomes

$$\frac{d}{dt}\int_{\Omega}\rho\boldsymbol{v}\,d\Omega = \int_{\Omega}\rho\boldsymbol{b}\,d\Omega + \int_{\partial\Omega}\boldsymbol{\sigma_n}\,dA. \tag{2.6}$$

With the Gaussian integral theorem and the definition of the stress tensor, $\boldsymbol{\sigma_n} = \boldsymbol{n}\cdot\boldsymbol{\sigma}$, Eq. (2.6) becomes

$$\frac{d}{dt}\int_{\Omega}\rho\boldsymbol{v}\,d\Omega = \int_{\Omega}\left(\rho\boldsymbol{b} + \nabla\cdot\boldsymbol{\sigma}\right)d\Omega. \tag{2.7}$$

The balance of moment of momentum is valid for any volumetric subset Ω of the deformed body which is only possible if the integrand vanishes, i.e.

$$\rho\dot{\boldsymbol{v}} = \nabla\cdot\boldsymbol{\sigma} + \rho\boldsymbol{b}.$$

Constitutive equations

The constitutive equations describe the relations between stresses and strains. They characterize the mechanical stiffness of a material. For linear elastic materials they are

$$\boldsymbol{\sigma} = \boldsymbol{C}\,\boldsymbol{\varepsilon}. \tag{2.8}$$

$\boldsymbol{C}$ is the fourth order stiffness tensor. It consists of 81 elastic coefficients, associating 9 stress components with 9 strain components. Due to the symmetry of the strain and the stress tensor only 21 components are independent. If the material is isotropic, $\boldsymbol{C}$ depends on only two parameters and Eq. (2.8) can be reduced to the Hooke's law,

$$\boldsymbol{\sigma} = \lambda\,\mathrm{tr}(\boldsymbol{\varepsilon})\,\boldsymbol{I} + 2\mu\,\boldsymbol{\varepsilon}. \tag{2.9}$$

The operator $\mathrm{tr}(\cdot)$ is the trace of a tensor, i.e. the sum of the diagonal elements. The two coefficients λ and μ are called Lamé constants. Alternative sets of two parameters are equivalently used to describe isotropic linear elasticity, for example Young's modulus (elastic modulus) and Poisson's ratio (E, ν) or shear and bulk modulus (G, K). Table 2.1 shows how to convert these quantities.

The Hooke's law only converts mechanical strain $\boldsymbol{\varepsilon}_{\mathrm{mech}}$ into stress, which implies that pure thermal strain does not cause any stresses. Including the strains $\boldsymbol{\varepsilon}_{\mathrm{th}}$ that result from a temperature change $\alpha\Delta T$, Eq. (2.9) becomes

$$\boldsymbol{\sigma} = \lambda\left(\mathrm{tr}(\boldsymbol{\varepsilon}) - 3\alpha\Delta T\right)\boldsymbol{I} + 2\mu\left(\boldsymbol{\varepsilon} - \alpha\Delta T\,\boldsymbol{I}\right).$$

Table 2.1: Conversion between elastic constants [123].

Elastic constant	λ, μ	E, ν	G, K
		Expressed as function of:	
λ		$\dfrac{E\nu}{(1+\nu)(1-2\nu)}$	$K - \dfrac{2}{3}G$
μ		$\dfrac{E}{2(1+\nu)}$	G
E	$\mu\dfrac{3\lambda + 2\mu}{\lambda + \mu}$		$\dfrac{9KG}{3K+G}$
ν	$\dfrac{\lambda}{2(\lambda+\mu)}$		$\dfrac{3K-2G}{6K+2G}$
G	μ	$\dfrac{E}{2(1+\nu)}$	
K	$\lambda + \dfrac{2}{3}\mu$	$\dfrac{E}{3(1-2\nu)}$	

If a material does not belong to the class of linear elastic materials, different constitutive equations have to be used that adequately model the observed material behavior. Constitutive equations for viscoelastic materials are discussed in Chapter 3.

Final set of governing equations, boundary and initial conditions

With the three sets of equations derived above the governing equations of a solid mechanical problem are now complete,

$$\boldsymbol{\varepsilon} = \frac{1}{2}\left(\nabla\boldsymbol{u} + (\nabla\boldsymbol{u})^T\right), \tag{2.10}$$

$$\rho\dot{\boldsymbol{v}} = \nabla\cdot\boldsymbol{\sigma} + \rho\boldsymbol{b}, \tag{2.11}$$

$$\boldsymbol{\sigma} = \lambda\left(\mathrm{tr}(\boldsymbol{\varepsilon}) - 3\alpha\Delta T\right)\boldsymbol{I} + 2\mu\left(\boldsymbol{\varepsilon} - \alpha\Delta T\,\boldsymbol{I}\right). \tag{2.12}$$

The equation system consists of 15 scalar equations, i.e. 6 compatibility equations, 3 balances of moment of momentum and 6 constitutive equations. The 15 unknowns are $\boldsymbol{u}$ (3 components), $\boldsymbol{\sigma}$ (6) and $\boldsymbol{\varepsilon}$ (6). For static problems, the left hand side in the balance of moment of momentum vanishes, $\rho\dot{\boldsymbol{v}} = 0$. Additional conditions are needed to obtain a uniquely defined mathematical problem. In case of static problems, boundary conditions are needed and in case of time-dependent problems, boundary and initial conditions must be given,

$$\boldsymbol{u}|_{\Gamma_1} = \boldsymbol{g}(\boldsymbol{x}, t), \quad \boldsymbol{x} \in \Gamma_1, \tag{2.13}$$

$$\boldsymbol{\sigma}\cdot\boldsymbol{n}|_{\Gamma_2} = \boldsymbol{f}(\boldsymbol{x}, t), \quad \boldsymbol{x} \in \Gamma_2, \tag{2.14}$$

$$\boldsymbol{u}(\boldsymbol{x}, t_0) = \boldsymbol{h}_1(\boldsymbol{x}), \tag{2.15}$$

$$\dot{\boldsymbol{u}}(\boldsymbol{x}, t_0) = \boldsymbol{h}_2(\boldsymbol{x}). \tag{2.16}$$

The boundary Γ_1 denotes the part of the body's surface where displacements are given and Γ_2 the surface part where stresses are applied. In general, solid mechanical problems as presented above form a set of partial differential equations, which cannot be solved analytically. Only for special cases, such as simple geometries, the solutions can be derived analytically. In most cases, the Finite-Element-Method (FEM) is used to solve the system of partial differential equations numerically.

2.2 Finite-Element-Method

The Finite-Element-Method is the commonly used numerical technique to solve continuum mechanical problems or partial differential equations in general. In mechanical applications, commercial software packages like Ansys [105], Abaqus [30], MSCMarc [87], Comsol Multiphysics [24] and a variety of other programs are available. The software requires the input of geometry, material constants and loading conditions while the mathematical procedures of the Finite-Element-Analysis are often not visible for the user. However, it is essential for the user to understand the fundamental ideas and concepts of the method to assure an appropriate operation of these powerful computational instruments.

Different discretization methods of continuum problems were developed independently by mathematicians and mechanical engineers in the early twentieth century. Later, in the 1960's, the term Finite-Element-Method was used to decribe a general discretization procedure of continuum problems [139]. There is a variety of textbooks that discuss the method from different perspectives, for example Braess [17], Klein [72], Merkel and Öchsner [83], Słuzalec [111], Wriggers [134] or Zienkiewicz [139, 140]. Here, only the basic ideas of FEM shall be explained that are given in more detail in [72] and [83].

2.2.1 Matrix-vector-formulation of the governing equations

As the stress and the strain tensors are symmetric, it is in this context convenient to write them as vectors of 6 independent components. In this so-called Voigt notation the stress and strain are written as

$$\boldsymbol{\sigma} = \begin{bmatrix} \sigma_{11} \\ \sigma_{22} \\ \sigma_{33} \\ \sigma_{23} \\ \sigma_{13} \\ \sigma_{12} \end{bmatrix} \quad \text{and} \quad \boldsymbol{\varepsilon} = \begin{bmatrix} \varepsilon_{11} \\ \varepsilon_{22} \\ \varepsilon_{33} \\ 2\varepsilon_{23} \\ 2\varepsilon_{13} \\ 2\varepsilon_{12} \end{bmatrix}.$$

Now, the governing equations of solid mechanics can be reformulated. The compatibility equation (2.10) becomes

$$\begin{bmatrix} \varepsilon_{11} \\ \varepsilon_{22} \\ \varepsilon_{33} \\ 2\varepsilon_{23} \\ 2\varepsilon_{13} \\ 2\varepsilon_{12} \end{bmatrix} = \begin{bmatrix} \partial/\partial x_1 & 0 & 0 \\ 0 & \partial/\partial x_2 & 0 \\ 0 & 0 & \partial/\partial x_3 \\ 0 & \partial/\partial x_3 & \partial/\partial x_2 \\ \partial/\partial x_3 & 0 & \partial/\partial x_1 \\ \partial/\partial x_2 & \partial/\partial x_1 & 0 \end{bmatrix} \cdot \begin{bmatrix} u_1 \\ u_2 \\ u_3 \end{bmatrix},$$

or

$$\boldsymbol{\varepsilon} = \boldsymbol{D} \cdot \boldsymbol{u}$$

respectively. In this section the Finite-Element-Method is explained for a static problem. Then, the left hand side of the balance of moment of momentum, given by Eq. (2.11), is equal to zero. The balance of moment of momentum in matrix-vector notation becomes

$$\begin{bmatrix} 0 \\ 0 \\ 0 \end{bmatrix} = \begin{bmatrix} \partial/\partial x_1 & 0 & 0 & 0 & \partial/\partial x_3 & \partial/\partial x_2 \\ 0 & \partial/\partial x_2 & 0 & \partial/\partial x_3 & 0 & \partial/\partial x_1 \\ 0 & 0 & \partial/\partial x_3 & \partial/\partial x_2 & \partial/\partial x_1 & 0 \end{bmatrix} \cdot \begin{bmatrix} \sigma_{11} \\ \sigma_{22} \\ \sigma_{33} \\ \sigma_{23} \\ \sigma_{13} \\ \sigma_{12} \end{bmatrix} + \begin{bmatrix} \rho b_1 \\ \rho b_2 \\ \rho b_3 \end{bmatrix}.$$

The matrix above is identical to the transpose of the matrix $\boldsymbol{D}$ so that we can write the balance of moment of momentum in short form

$$\boldsymbol{0} = \boldsymbol{D}^T \cdot \boldsymbol{\sigma} + \boldsymbol{p}.$$

The linear elastic constitutive equation (2.9) is written in terms of the Lamé constants. Replacing these constants by E and ν according to Table 2.1 we obtain the constitutive equation in the form

$$
\begin{bmatrix}
\sigma_{xx} \\
\sigma_{yy} \\
\sigma_{zz} \\
\tau_{yz} \\
\tau_{xz} \\
\tau_{xy}
\end{bmatrix}
= \frac{E}{(1+\nu)(1-2\nu)}
\begin{bmatrix}
1-\nu & \nu & \nu & 0 & 0 & 0 \\
\nu & 1-\nu & \nu & 0 & 0 & 0 \\
\nu & \nu & 1-\nu & 0 & 0 & 0 \\
0 & 0 & 0 & \frac{1-2\nu}{2} & 0 & 0 \\
0 & 0 & 0 & 0 & \frac{1-2\nu}{2} & 0 \\
0 & 0 & 0 & 0 & 0 & \frac{1-2\nu}{2}
\end{bmatrix}
\cdot
\begin{bmatrix}
\varepsilon_{xx} \\
\varepsilon_{yy} \\
\varepsilon_{zz} \\
2\varepsilon_{yz} \\
2\varepsilon_{xz} \\
2\varepsilon_{xy}
\end{bmatrix}
$$

which can also be written as

$$\boldsymbol{\sigma} = \boldsymbol{C} \cdot \boldsymbol{\varepsilon}.$$

The tensor $\boldsymbol{C}$ from Eq. (2.8) has now become a 6×6 matrix. In summary, the governing equations of solid mechanics for a static problem in matrix-vector notation are

$$
\begin{align}
\boldsymbol{\varepsilon} &= \boldsymbol{D} \cdot \boldsymbol{u} \tag{2.17}\\
\boldsymbol{0} &= \boldsymbol{D}^T \cdot \boldsymbol{\sigma} + \boldsymbol{p} \tag{2.18}\\
\boldsymbol{\sigma} &= \boldsymbol{C} \cdot \boldsymbol{\varepsilon}. \tag{2.19}
\end{align}
$$

2.2.2 Principle of virtual work

There are different but equivalent approaches to derive the formalism of the Finite-Element-Method for static problems, such as the principle of virtual work or the method of Galerkin. Both approaches lead to a linear system $\boldsymbol{k} \cdot \boldsymbol{u}_p = \boldsymbol{F}$ with a stiffness matrix $\boldsymbol{k}$, a known vector $\boldsymbol{F}$ on the right hand side and the unknown vector $\boldsymbol{u}_p$ that contains displacement parameters. Solving for $\boldsymbol{u}_p$ does then provide the displacements in the deformed body so that the strains and the stresses can be directly calculated from the displacement solution, using Eqs. (2.17) and (2.19).
Within the principle of virtual work the balance equation (2.18) is replaced by the postulation that the internal virtual work equals the external virtual work,

$$\delta\Pi_{\text{int}} = \delta\Pi_{\text{ext}}.$$

The virtual work is generated by small compatible displacements $\delta\boldsymbol{u}$ in the body B, so that we write

$$\delta\Pi_{\text{int}} = \int_B \delta\boldsymbol{\varepsilon}^T \cdot \boldsymbol{\sigma}\, dV$$

and

$$\delta\Pi_{\text{ext}} = \delta\boldsymbol{u}^T \cdot \boldsymbol{f} + \int_B \delta\boldsymbol{u}^T \cdot \boldsymbol{p}\, dV + \int_{\partial B} \delta\boldsymbol{u}^T \cdot \boldsymbol{q}\, dA,$$

where $\boldsymbol{f}$ are concentrated loads on the boundary ∂B, $\boldsymbol{q}$ are distributed loads on ∂B and $\boldsymbol{p}$ are volume forces in B. It follows from Eqs. (2.17) and (2.19)

$$\delta\boldsymbol{\varepsilon}^T = \delta\boldsymbol{u}^T \cdot \boldsymbol{D}^T$$

and

$$\boldsymbol{\sigma} = \boldsymbol{C} \cdot \boldsymbol{D} \cdot \boldsymbol{u}$$

so that the equality of the internal and external virtual work becomes

$$\int_B \delta\boldsymbol{u}^T \cdot \boldsymbol{D}^T \cdot \boldsymbol{C} \cdot \boldsymbol{D} \cdot \boldsymbol{u}\, dV = \delta\boldsymbol{u}^T \cdot \boldsymbol{f} + \int_B \delta\boldsymbol{u}^T \cdot \boldsymbol{p}\, dV + \int_{\partial B} \delta\boldsymbol{u}^T \cdot \boldsymbol{q}\, dA.$$

So far, the formalism is exact and corresponds to Eqs. (2.17) - (2.19). Now, we approximate the vector field $\boldsymbol{u} = \boldsymbol{u}(\boldsymbol{x})$ by the product of a matrix $\boldsymbol{G}$ that is a known function of $\boldsymbol{x}$ and a finite vector with coefficients $\boldsymbol{u}_p$,

$$\boldsymbol{u} \approx \boldsymbol{G} \cdot \boldsymbol{u}_p.$$

The choice of $\boldsymbol{G}$ and $\boldsymbol{u}_p$ is explained in the following Section 2.2.3. Now, we obtain

$$\int_B \delta \boldsymbol{u}_p^T \cdot \boldsymbol{G}^T \cdot \boldsymbol{D}^T \cdot \boldsymbol{C} \cdot \boldsymbol{D} \cdot \boldsymbol{G} \cdot \boldsymbol{u}_p \, dV = \delta \boldsymbol{u}_p^T \cdot \boldsymbol{G}^T \cdot \boldsymbol{f} + \int_B \delta \boldsymbol{u}_p^T \cdot \boldsymbol{G}^T \cdot \boldsymbol{p} \, dV + \int_{\partial B} \delta \boldsymbol{u}_p^T \cdot \boldsymbol{G}^T \cdot \boldsymbol{q} \, dA$$

with the only unknown variable $\boldsymbol{u}_p$. Since the equation above has to be fulfilled for all virtual displacements and since $\boldsymbol{u}_p$ is by definition not dependent on $\boldsymbol{x}$, it follows

$$\int_B (\boldsymbol{D} \cdot \boldsymbol{G})^T \cdot \boldsymbol{C} \cdot (\boldsymbol{D} \cdot \boldsymbol{G}) \cdot dV \, \boldsymbol{u}_p = \boldsymbol{G}^T \cdot \boldsymbol{f} + \int_B \boldsymbol{G}^T \cdot \boldsymbol{p} \, dV + \int_{\partial B} \boldsymbol{G}^T \cdot \boldsymbol{q} \, dA.$$

By assigning to $\boldsymbol{F}$ the right hand side that consists of the external forces,

$$\boldsymbol{F} = \boldsymbol{G}^T \cdot \boldsymbol{f} + \int_B \boldsymbol{G}^T \cdot \boldsymbol{p} \, dV + \int_{\partial B} \boldsymbol{G}^T \cdot \boldsymbol{q} \, dA,$$

and setting

$$\boldsymbol{k} = \int_B (\boldsymbol{D} \cdot \boldsymbol{G})^T \cdot \boldsymbol{C} \cdot (\boldsymbol{D} \cdot \boldsymbol{G}) \cdot dV = \int_B \boldsymbol{B}^T \cdot \boldsymbol{E} \cdot \boldsymbol{B} \, dV$$

we obtain the linear system

$$\boldsymbol{k} \cdot \boldsymbol{u}_p = \boldsymbol{F}.$$

Commercial FEM-programs offer a number of choices for the functions in $\boldsymbol{G}$. For these functions the derivatives needed for $\boldsymbol{D} \cdot \boldsymbol{G}$ are implemented in the software as well so that the matrix $\boldsymbol{k}$ is automatically assembled without adding computational errors. For the right hand side $\boldsymbol{F}$ numerical quadrature formulas are used to compute the solution of the integrals so that $\boldsymbol{F}$ contains potential numerical errors.

The time-consuming part in a FEM-simulation is solving the linear system $\boldsymbol{k} \cdot \boldsymbol{u}_p = \boldsymbol{F}$. There are two strategies to solve the linear system, either by direct solvers or by iterative solvers. The direct solvers are modified versions of the Gaussian elimination method. They are robust but demand a high computational effort so that they take generally more time to find a solution and need more storage capacity than the iterative solvers. The iterative solvers are modified versions of Newton's method. There, the real solution is successively approximated starting from a first guess for $\boldsymbol{u}_p$. They are faster than direct solvers and needs less storage capacities during the solving process. However, they are less stable than direct solvers as the solution process must converge towards the real solution which is not always the case. The standard recommendation is to use direct solvers for small and nonlinear problems while the iterative solvers are generally better suited for large problems.

2.2.3 Element shape functions

The main idea to approximate the real solution $\boldsymbol{u}$ by $\boldsymbol{G} \cdot \boldsymbol{u}_p$ is to subdivide the body B in small elements and to postulate a polynomial shape of $\boldsymbol{u}$ within every element. As an example, such a subdivision, also called mesh, into triangular elements of a two-dimensional problem is shown in Fig. 4.15. If we choose a linear shape for the approximative solution $\hat{\boldsymbol{u}}$ in such a triangle, the displacements can be expressed by

$$\hat{\boldsymbol{u}} = \left[\begin{array}{c} \hat{u}_1(x_1, x_2) \\ \hat{u}_2(x_1, x_2) \end{array} \right] = \left[\begin{array}{c} \alpha_{00} + \alpha_{10} x_1 + \alpha_{01} x_2 \\ \beta_{00} + \beta_{10} x_1 + \beta_{01} x_2 \end{array} \right].$$

The six unknown coefficients α_{00}, α_{10}, α_{01}, β_{00}, β_{10} and β_{01} are uniquely determined if we know the values of $\hat{u}_1$ and $\hat{u}_2$ in three points in the triangle, for example in the corners as shown in
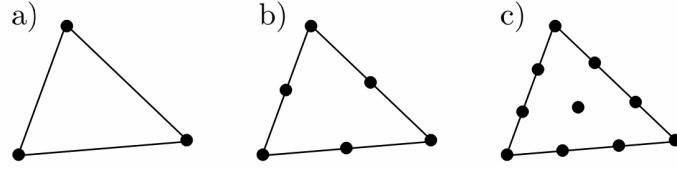
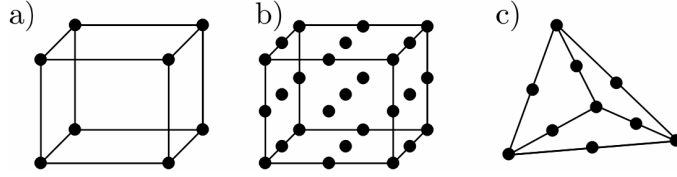Figure 2.4: Nodes for linear (a), quadratic (b) and cubic (c) shape functions for a triangular 2d-element.

Figure 2.5: Hexahedral 3d-element with linear shape function (a), hexahedral 3d-element with quadratic shape function (b) and tetrahedral 3d-element with quadratic shape function (c).

Fig. 2.4 a). Now the polynomial functions can be grouped in $\boldsymbol{G}$ and the coefficients α and β of all elements in $\boldsymbol{u}_p$. The interpolation points are called nodes. Mathematically speaking, the number of nodes corresponds to the dimension of the polynomial space. Positioning the nodes in the corners has the advantage to automatically create a continuous solution $\hat{\boldsymbol{u}}$ in B because each node is used for interpolation in the adjacent element as well. The approximation of the real solution $\boldsymbol{u}$ can be improved by choosing higher polynomial degrees for the shape functions. Then, the number of nodes increases accordingly as shown for quadratic and cubic shape functions in Fig. 2.4 b and 2.4 c.

In general, a scalar polynomial function $p(\boldsymbol{x})$ can be constructed according to Table 2.2 for an element of a one-, two- or three-dimensional deformable body. Furthermore, there are alternatives for the geometric form of an element, for example quadrangles in 2d or prisms and hexahedrons in 3d.

If the user is not satisfied with the level of detail of a numerical solution obtained from a FEM-simulation, there are two strategies to improve the accuracy of the numerical solution. It is either possible to generate a better approximation of the solution in every element by increasing the polynomial degree of the shape functions or to refine the mesh by decreasing the size of each element. Both options lead to higher computational effort because the size of $\boldsymbol{u}_p$, $\boldsymbol{k}$ and $\boldsymbol{F}$ increases. The key is to assure a high accuracy in regions where the solution changes considerably and to keep the level of detail low where the solution is smooth.

Table 2.2: Overview of shape functions with polynomial degree k for different geometrical dimensions and element types.

Dimension	Element form	Shape function		Number of nodes
1	line	$p(x)$	$= \sum_{0 \le i \le k} \alpha_i x^i$	$k+1$
2	triangle	$p(x_1, x_2)$	$= \sum_{0 \le i+j \le k} \alpha_{ij} x_1^i x_2^j$	$\frac{1}{2}(k+1)(k+2)$
2	quadrangle	$p(x_1, x_2)$	$= \sum_{0 \le i,j \le k} \alpha_{ij} x_1^i x_2^j$	$(k+1)^2$
3	tetrahedron	$p(x_1, x_2, x_3)$	$= \sum_{0 \le i+j+l \le k} \alpha_{ijl} x_1^i x_2^j x_3^l$	$\frac{1}{6}(k+1)(k+2)(k+3)$
3	hexahedron	$p(x_1, x_2, x_3)$	$= \sum_{0 \le i,j,l \le k} \alpha_{ijl} x_1^i x_2^j x_3^l$	$(k+1)^3$

Table 2.3: Mechanical properties of standard float glass (soda-lime) and borosilicate glass (*: converted from psi-units).

Glass type and reference	E [GPa]	ν [-]	α [10^{-6} 1/K]	ρ [g/cm^3]
float glass [18]	73		8.96	2.495
soda-lime [101]	68.95*	0.24	9.2	
soda-lime [104]	69.1		9	
soda-lime [108]	74		9.5	2.53
soda-lime [127]	73.4			
soda-lime [135]	70		9	2.5
borosilicate [18]	59		3.25	2.226
borosilicate [104]	63.7			
borosilicate [101]	65.5*	0.20	3.25	
borosilicate [127]	63.7			

2.3 Materials

The materials used in a photovoltaic module must be mechanically characterized in order to accurately simulate the deformation of a module. In this section, the materials are described by linear elastic models, that require two material parameters (see Table 2.1). In the following paragraphs the Young's modulus E and Poisson's ratio ν are used as a pair of elastic constants. The values are either taken from literature data or are determined by mechanical testing. The testing procedures are described in detail below.

2.3.1 Glass

Glass is formed by amorphous soldification from a molten mass that contains silica and, depending on the sort of glass, other constituents like sodium carbonate, all kinds of oxides, boron or lead. The glass used for photovoltaic modules or windows is float glass. This name refers to the float process where the molten glass is continuously led from the cast over a tin bath where it soldifies [19, 62]. The float process provides low stress glass panes with very planar surfaces and no air inclusions. Almost all float glasses are soda-lime glasses which implies that their chemical structure is made of silica, sodium carbonate, calcium oxide, aluminum oxide and magnesium oxide. Float glass used in solar applications often exhibits a lower content of iron impurities in order to ensure a better transmission of sunlight compared to standard float glass. Additional treatment of float glass also allows to freeze stress in the glass which changes the fracture properties. These types of glass are found under the names of prestressed or toughened safety glass. While conventional float glass has a bending strength of 45 MPa, the value for prestressed glass is 70 MPa and for toughened safety glass it is 120 MPa [85]. Typical photovoltaic glasses are toughened or prestressed.
Here the focus lies on standard float glass as it is used in the thermomechanical experiments, that are discussed in Chapter 4.

Mechanical properties

After soldification the formerly liquid glass has a very high viscosity ($\eta \approx 10^{14}$ Pa·s at $T \approx 600°$C [104], $\eta \approx 10^{12}$ Pa·s at $T \approx 530°$C [10]). It can thus be considered as purely elastic below the soldification point which is referred to as the glass transition temperature T_G. For float glass T_G is around 550°C [18]. Stress-strain curves of glass show linear elastic material behaviour until fracture. The mechanical material properties of conventional float glass used in this study are taken from the literature and are shown in Table 2.3. The general testing procedures of how to
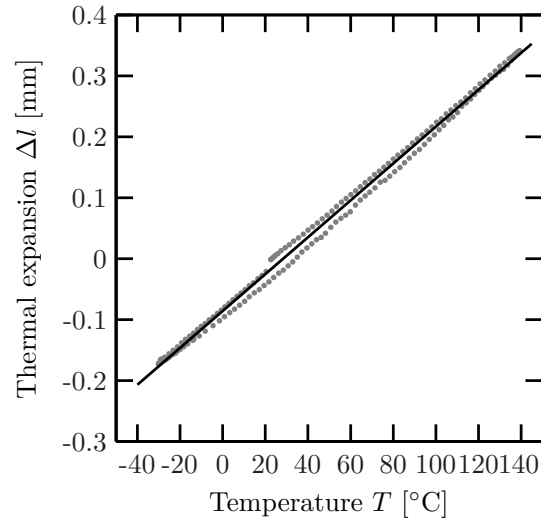
Figure 2.6:   Measured thermal expansion of soda-lime glass with linear regression

obtain the mechanical parameters of glass can be found in [21]. The mechanical parameters of borosilicate glass are also shown in Table 2.3 because we use this low-CTE-glass for a laminate experiment in Chapter 4.

Measurement of coefficient of thermal expansion

The coefficient of thermal expansion of glass is considered a critical quantity for the thermomechanical investigation of solar modules. An experiment is conducted to check the value of 9×10^{-6} 1/K. The experiment uses a stereo camera system of a digital image correlation system to perform two 2d-displacement measurements with simultaneous data capturing. The details of the system are explained in Subsection 4.1.1.

A glass plate of 45 cm × 15 cm × 4 mm is positioned in a climate chamber behind a window and is equipped with a temperature sensor. Two cameras of a digital image correlation system, that are in parallel orientation to each other, view the regions near the glass edges. Each camera faces the glass surface in a rectangular manner. The inspected regions near the edges of the glass have been coloured with a random speckle pattern of black and white spray paint. A mark is set in both speckled regions creating a precise distance of 38.75 cm from mark to mark. From the experimental setup follows that the cameras should have the same distance. The calibration of each camera that enables the computation of displacement in millimeters from displacement in pixels is made with the help of graph paper. At room temperature the paper is held on the glass surface before the experiment. First, the temperature is ramped up to 140°C followed by cooling down to −30°C and is finally heated up to room temperature again. The change in length of the glass is plotted in Fig. 2.6. As $\varepsilon = \Delta l / l$, these total elongation data have to be related to the initial distance of $l = 387.5$ mm of the measurement points to obtain the CTE. The straight line represents the linear regression and is used to calculate the CTE value of the experiment which is given in Table 2.4.

The measured value is around 1×10^{-6} 1/K lower than the literature data. Two reasons may

Table 2.4: Measured CTE of soda-lime glass with upper and lower confidence bound of regression.

| CTE α | Confidence bounds | |
$[10^{-6}$ 1/K]	lower 95%	upper 95%
7.806	7.747	7.866
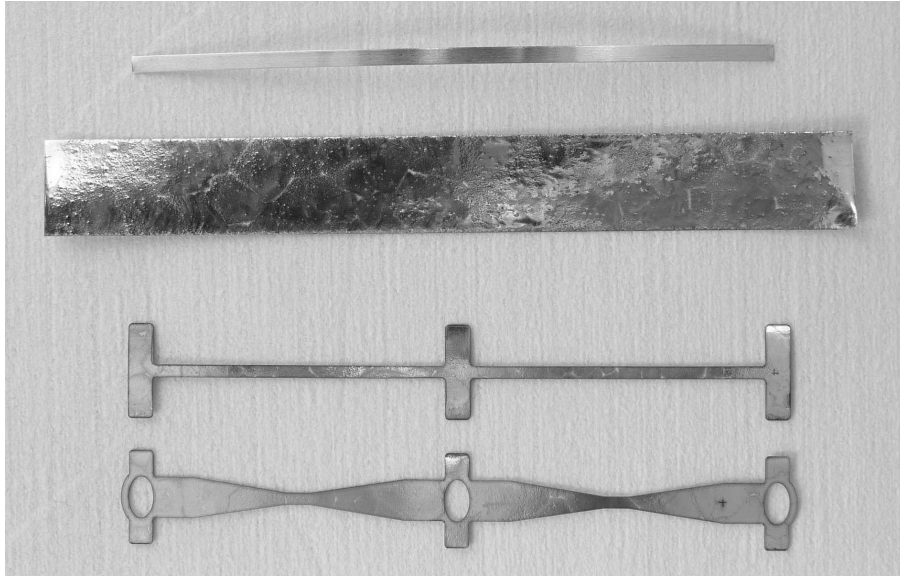
Figure 2.7: Tin-plated copper ribbons. Standard 2 mm wide copper ribbon, 12 mm wide copper ribbon and two shapes of interconnectors made from wide copper ribbon (top to bottom).

explain the deviation. First, systematic errors in the experiment and second the assumption that the composition of the measured glass does not exactly correspond to soda-lime glass. For the simulations in Chapter 4 we use the value of 8×10^{-6} 1/K. There, we also vary the CTE value by $\pm 10\%$ (7.2×10^{-6} 1/K, 8.8×10^{-6} 1/K) in order to check the sensitivity of this parameter for the simulation results.

2.3.2 Copper ribbons

Copper is a metallic material, whose properties are well known. It is chosen for the electrical interconnection between the solar cells because of its excellent electrical conductivity of around 58 m/Ω mm^2 which is, after silver, the highest value of all metals [103]. The copper ribbons that are used in solar modules are typically 130 µm thick and 2 mm wide. The copper ribbon is plated with a 20 µm thick layer of solder material which increases the total thickness up to about 170 µm. The plating allows a direct soldering of the ribbon to the solar cell by softly pressing the plated ribbon to the metallized surface of the solar cell and simultaneous heating of the contact area.

Mechanical properties

In this study the plating is assumed to be negligible for the mechanical material properties of the ribbon so only the values of copper are assigned to the interconnector. Table 2.5 lists the values for copper in general. A recent study by Wiese [128] on the mechanical properties of copper ribbons used in solar modules finds the Young's modulus E of plated copper ribbons to be significantly lower than those of pure copper, see Table 2.5. He also determines the temperature dependence of the Young's modulus ($dE/dT = -0.056$ GPa/K for $T = \{40, \ldots, 120°C\}$) and constructs a bilinear model to include plastic deformation. He finds linear elastic deformation for strain values below 1%. For higher strains the Hooke's law (Eq. (2.9)) is not applicable.

In this work we focus on the thermomechanics of non-interconnected cells in modules and the mechanical parameters of copper ribbons are not used as input parameters for FEM-simulations in subsequent sections. However, we measure the displacement of the gap between two solar cells in interconnected and non-interconnected laminates in Section 4.2. From the simulations of the

Table 2.5: Mechanical properties of copper.

Copper and reference	E [GPa]	ν [-]	α [10^{-6} 1/K]	ρ [g/cm^3]
copper [16]	117		17	8.907
copper, hard drawn [16]	124.1			
copper, soft wrought [16]	103.4			
copper [60]	120	0.34		
copper [85]	100 - 130		16.8	8.93
copper [99]	125	0.34	17.7	8.93
pure copper [109]			16.5	8.96
copper ribbon (type 1) [128]	86.1			

gap displacements in Sections 4.3 and 4.4 we conclude how much thermal deformation the copper ribbons have to compensate between two cells during thermal cycling.

2.3.3 Crystalline silicon solar cells

Crystalline silicon solar cells are made from mono- or multicrystalline silicon wafers. The thicknesses of the wafers are nowadays typically between 140 μm and 200 μm, the standard sizes are 125 mm × 125 mm or 156 × 156 mm. Multicrystalline cells are usually full squared (Fig. 2.8) as multicrystalline blocks of silicon are cut into columns with a squared base area. Each column is then cut into wafers by wire-sawing. Monocrystalline wafers are cut in thin slices out of a round shaped monocrystalline ingot. As the diameter of the ingot is smaller than the diagonal of a full squared cell, the monocristalline wafers have round shaped corners (Fig. 2.8). The shape is referred to as pseudo-square. The monocrystalline cells and wafers that are investigated in this study are (100) oriented which means that the normal of the wafer surface points in the crystallographic direction of <100>. The edges of the wafers are usually parallel to the [100]-direction (Fig. 2.10). As the processing of a wafer to a solar cell mainly results in modifications of the wafer surfaces or structures thin compared to the wafer thickness, the elastic properties of a monocrystalline solar cells are assumed to correspond well to those of the original wafer.

Mechanical properties

Silicon is a brittle material that shows basically no ductile effects. The stress strain curve is linear until fracture. Linear elasticity is thus the correct model to describe the mechanics of monocrystalline silicon. However, it has anisotropic material properties that are due to the crystallographic structure. We thus obtain different values of the elastic constants for different loading directions. For a wafer that is cut out of a monocrystalline ingot with surface normal in <100>-direction and edges along the <010>- and <001>-direction, the wafer coordinate system matches the materials coordinate system. Then the matrix $\boldsymbol{C}$ of the constitutive equation written in the form of Eq. (2.19) becomes, according to [51],

$$\boldsymbol{C} = \begin{bmatrix} C_{11} & C_{12} & C_{12} & 0 & 0 & 0 \\ C_{12} & C_{11} & C_{12} & 0 & 0 & 0 \\ C_{12} & C_{12} & C_{11} & 0 & 0 & 0 \\ 0 & 0 & 0 & C_{44} & 0 & 0 \\ 0 & 0 & 0 & 0 & C_{44} & 0 \\ 0 & 0 & 0 & 0 & 0 & C_{44} \end{bmatrix} \quad (2.20)$$

with the values for C_{11}, C_{12} and C_{44} from Table 2.6. The structure of the matrix $\boldsymbol{C}$ in Eq. (2.20) is generally valid for any material with a cubic symmetry [14]. To calculate the Young's modulus
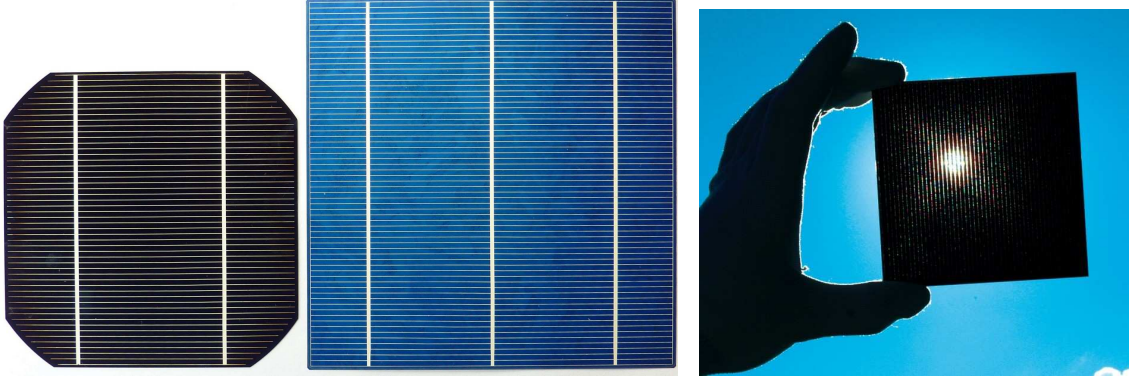
Figure 2.8: 125×125 mm^2 pseudo-squared monocrystalline solar cell (left), 156×156 mm^2 full-squared multicrystalline solar cell (center) and 100×100 mm^2 full-squared RISE-EWT solar cell(right), where the alignment of the laser drilled EWT holes is visible.

in x-direction, $\boldsymbol{C}$ is inverted and it then holds for a uniaxial stress state

$$\varepsilon_{11} = \frac{C_{11} + C_{12}}{C_{11}^2 + C_{11}C_{12} - 2C_{12}^2}\, \sigma_{11}, \tag{2.21}$$

so that

$$E_x = C_{11} - 2\frac{C_{12}^2}{C_{11} + C_{12}}.$$

Due to the cubic symmetry it holds

$$E_x = E_y = E_z$$

and as the material's coordinate system equals the wafer's coordinate system we find

$$E_{<100>} = E_{<010>} = E_{<001>} = E_x = E_y = E_z.$$

For materials with a cubic symmetry the coefficient of thermal expansion must be isotropic [14]. Table 2.6 also gives temperature dependencies of the elastic parameters.

Bending tests of solar cells

Bending tests are conducted in order to check how well the silicon values from the literature agree with experiments on solar cells. The cells tested are RISE-EWT solar cells [43, 42, 41]. The reason for the choice of this special cell type are research activities at the ISFH that focused on the industrial implementation of the RISE cell concept. Within these activities the mechanical strength of the RISE cell was adressed by 4-point bending tests [11, 106]. Two types of these cell structures are tested, first Czochralski-grown(CZ) silicon solar cells with a thickness of $200\,\mu$m and second cells processed on $250\,\mu$m thick float-zone(FZ) silicon. The CZ-cells are 125 mm $\times$ 125 mm pseudo-square while the FZ-samples are quadratic with an edge length of 100 mm. Typical characteristics of this cell type, that are mechanically relevant, are the laser ablated grooves at the rear side of the cell with a depth of about 20 to $25\,\mu$m and around 20 000 laser drilled holes that are oriented in lines in parallel to the grooves (Figs. 2.8 and 2.11).

In a 3-point bending test a solar cell is placed on two rolls with a distance of 80 mm. A third roll presses from the top in the center between the two bottom rolls. The force F and the deflection w under the centered roll are monitored (Fig. 2.9). Classical beam theory is used to calculate elastic constants from the experimental force and deflection values. The concept of beam theory is explained in many textbooks, for example [9, 55]. When the sample is loaded, the top surface
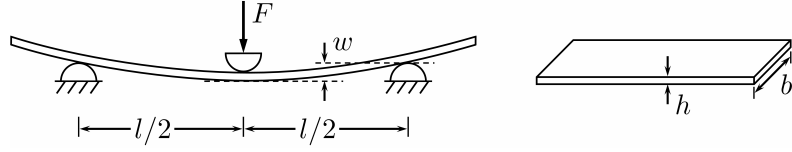
Figure 2.9: 3-point bending: relevant parameters and measured quantities

undergoes compression and the bottom surface tension. The stress along the bending direction (in-plane, rectangular to the rolls) is linear over the thickness and the height of the beam remains unchanged under bending. With these assumptions the stress and strain take their maxima on the sample surfaces. The formula for 3-point bending is given in [55],

$$EIw = \frac{l^3}{48}F,$$

with the Young's modulus E, the moment of inertia of area I and the distance l between the lower two rolls. For a rectangular cross-section of the beam, the moment of inertia of area is [55]

$$I = \frac{bh^3}{12}, \tag{2.22}$$

where h is the thickness and b the width.

For the CZ samples the parameters are $b = 125$ mm, $l = 80$ mm and $h = 190\,\mu$m. The second series of tests is conducted on a number of FZ cells with $b = 100$ mm, $l = 80$ mm and $h = 240\,\mu$m. The measured force-deflection curves of both series are shown in Figs. 2.12 and 2.13. We set

$$E_p = F/w$$

and determine one constant value for E_p for every measurement curve by a linear regression between $w = 0.3$ mm and $w = 2.3$ mm, except for sample 1 of the CZ cells (between 1.25 mm and 2.49 mm). The Young's modulus is then calculated by

$$E = \frac{l^3}{48I}E_p$$

Table 2.6: Mechanical properties of silicon.

Quantity	Unit	Value	Reference
C_{11}		164.8	
C_{12}	[GPa]	63.5	[51]
C_{44}		79.0	
$(\mathrm{d}C_{11}/\mathrm{d}T)/C_{11}$		-122	
$(\mathrm{d}C_{12}/\mathrm{d}T)/C_{12}$	[10^{-6} 1/K]	-162	[51]
$(\mathrm{d}C_{44}/\mathrm{d}T)/C_{44}$		-97	
$E_{<100>}$		129.5	
$E_{<110>}$	[GPa]	168.0	[51]
$E_{<111>}$		186.5	
$(\mathrm{d}E_{<100>}/\mathrm{d}T)/E_{<100>}$		-63	
$(\mathrm{d}E_{<110>}/\mathrm{d}T)/E_{<110>}$	[10^{-6} 1/K]	-80.3	[51]
$(\mathrm{d}E_{<111>}/\mathrm{d}T)/E_{<111>}$		-45.6	
$\alpha(T = 220\text{K})$		1.717	[77]
$\alpha(T = 260\text{K})$		2.225	[77]
$\alpha(T = 300\text{K})$	[10^{-6} 1/K]	2.614	[102]
$\alpha(T = 340\text{K})$		2.915	[102]
$\alpha(T = 420\text{K})$		3.342	[102]
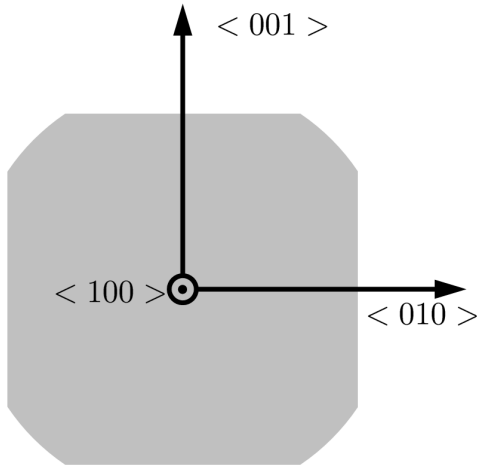
Figure 2.10: Crystallographic orientation of a solar cell
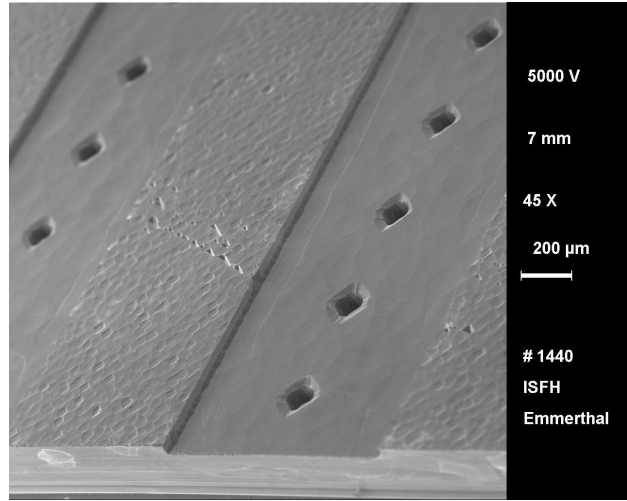
Figure 2.11: SEM image of a RISE-EWT solar cell with structure of grooves and holes (taken from [41]).

and is shown in Figs. 2.14 and 2.15. The filled circles stand for bending with rolls parallel to the grooves and the open squares for a perpendicular configuration of rolls and grooves.

As the structure of the RISE-EWT solar cells features grooves with a height of 20-25 µm, the experimental values can either be regarded as effective material constants of this special solar cell type or, for a comparison with silicon material properties, the values for I must be adjusted. Thus, a higher and a lower moment of inertia of area $I_{1,2}$ are calculated with $h_{1,2} = h \pm 10$ µm. The resulting values for E are represented by the errorbars in Figs. 2.14 and 2.15.

The elastic moduli E are found to depend on the orientation of the samples in the test. The specimens that are tested in parallel orientation of grooves and rolls always show lower stiffnesses than in perpendicular orientation. As assumed before, this fact is related to the geometrical structure of the cells. The lines act as perforations and thus lower the resistance of the material against the applied load. The grooves lead to a lower bending resistance when they are parallel to the loading axis. The measured values of E are compared to the Young's modulus of monocrystalline silicon in the <100>-direction (Table 2.6) which is shown by the straight lines in Figs. 2.14 and 2.15. The deviation of thickness has a strong impact on the measurement results which becomes obvious by the exponent of 3 in Eq. (2.22) and thus the large errorbars in the plot. The adjustment of I with $h_{1,2} = h \pm 10$ µm, that accounts for the lowered stiffness of the samples along grooves, gives values of E that enclose the silicon value.

We conclude from this experiment with a limited number of samples that the measured data agree reasonably with the material properties of bulk silicon. The deviation from sample to sample and the uncertainty in the thickness of the specimens is too large to construct an effective Young's modulus for RISE-EWT cells that differs significantly from the silicon data. We therefore assume silicon solar cells to exhibit the same mechanical properties as monocrystalline silicon wafers and simulate them in Sections 4.3 and 4.4 according to the values in Table 2.6.

2.3.4 Back sheet

The back sheet protects the solar cells and the lamination sheets from external influences such as humidity, atmospheric exposure, aggressive substances or scratches. It also provides electric
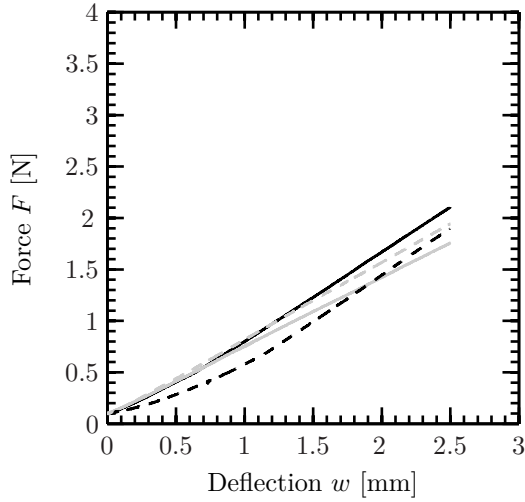
Figure 2.12: Force-deflection curves for 2 CZ-samples. Straight lines indicate grooves and hole lines parallel to rolls, dashed lines indicate grooves and hole lines perpendicular to rolls.
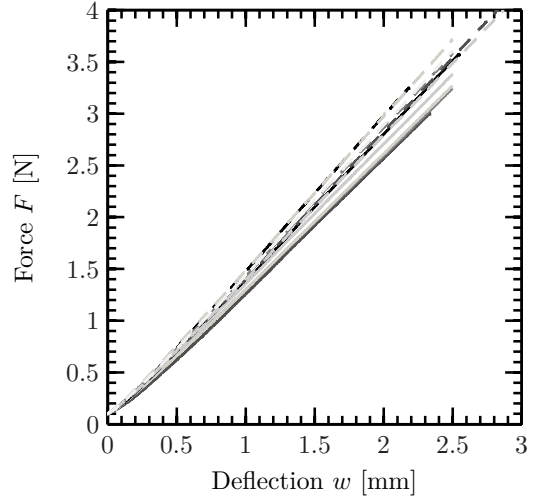
Figure 2.13: Force-deflection curves for 6 FZ-samples. Straight lines indicate grooves and hole lines parallel to rolls, dashed lines indicate grooves and hole lines perpendicular to rolls.
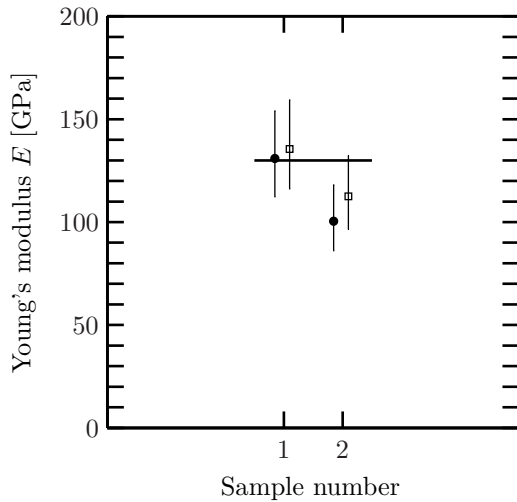
Figure 2.14: Extracted Young's moduli for CZ-samples with sample structure in parallel orientation ($\bullet$) and perpendicular orientation ($\square$) to rolls. The error bars indicate varied thicknesses by $\pm 10\,\mu$m. The straight line corresponds to $E_{<100>}$ from Table 2.6.
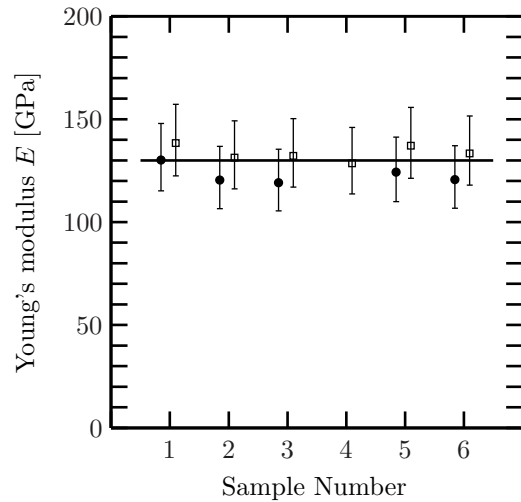
Figure 2.15: Extracted Young's moduli for FZ-samples with sample structure in parallel orientation ($\bullet$) and perpendicular orientation ($\square$) to rolls. The error bars indicate varied thicknesses by $\pm 10\,\mu$m. The straight line corresponds to $E_{<100>}$ from Table 2.6.
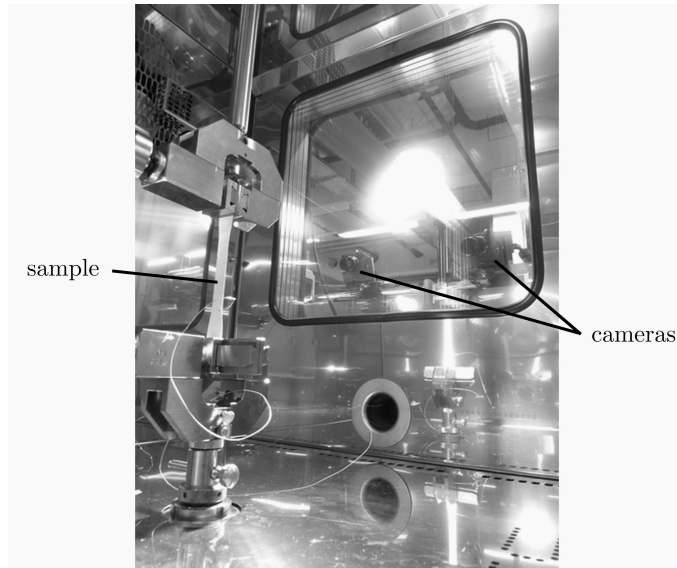
Figure 2.16: View of sample with grippers from within the temperature chamber. The stereo camera system is placed behind the window.

insulation. For crystalline wafer based modules back sheets made of plastic materials are commonly used. Back sheets are available in different colors but only white (higher reflexion and thus better optical performance) and black (attractive visual appearance) are often used. Different compositions of back sheets are available and the PV manufacturer's material choice is largely influenced by the lamination material and the sensitivity of the solar cells to corrosion. In this work the widely-used back sheets with PVF(polyvinyl fluoride), also known as Tedlar from DuPont, and PET-layers is investigated. Here the product Isovolta Icosolar 2442 is tensile tested to extract its mechanical properties.

Mechanical properties

Tensile test sample are measured at three different temperatures (20°C, 80°C and -35°C). The specimens are cut out of a 0.35 mm thick sheet. For testing temperatures of -35°C the shape of the samples is chosen in accordance to the ASTM D638 TYPE IV standard with a width of the narrow section of 6 mm. For the other temperatures the larger ASTM D638 TYPE I specimen form with a width of 13 mm is used. In order to check a possible anisotropy of the material, 5 samples are cut under an angle of 90° to the rolling direction of the sheet and are tested at room temperature (20°C transverse). The testing setup consists of a tensile testing machine that is mounted on top of a climate chamber. The specimen holders reach into the chamber and a digital image correlation system records the strain from outside the chamber (Fig. 2.16). This test setup enables the monitoring of force F, temperature T, elongational strain ε_l and transverse strain ε_t. The elongational velocity is 1 mm/min for the smaller samples (TYPE IV, -35°C) and 2 mm/min for the other samples (20°C, 80°C, TYPE I).

The Young's modulus is calculated by linear regression of the stress-strain curves in Fig. 2.17 within the strain intervall of 0.001 to 0.020 (-35°C), 0.001 to 0.025 (20°C) and 0.001 to 0.015 (80°C). Poisson's ratio ν is determined in these intervals as the slope of the ε_l-ε_t-curves in Fig. 2.18. The values of the elastic parameters E and ν are summarized in Table 2.7 and plotted versus temperature in Figs. 2.19 and 2.20.

The values in each of the three temperature regions are very reproducible. The small differences in the Young's modulus and Poisson's ratio of the samples in rectangular material orientation indicate a slight anisotropy at room temperature which we do not account for in the FEM-simulations in Section 4.4. We use the values of 3.5 GPa for E and 0.29 for ν.
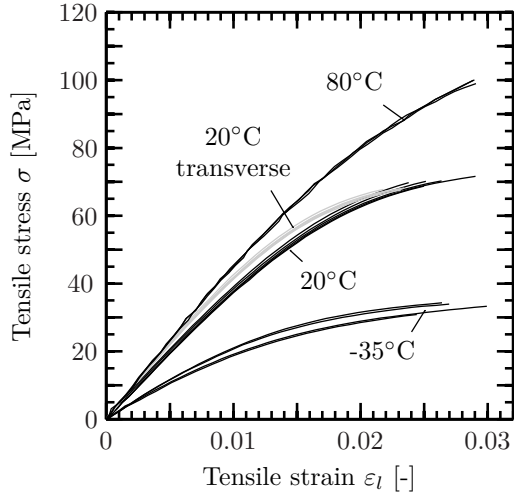
Figure 2.17: Stress-strain-curves of Isovolta Icosolar 2442 at different temperatures: 20°C (5 samples), 80°C (4), -35°C (3) and 20°C transverse (gray, 5) with a different material orientation.
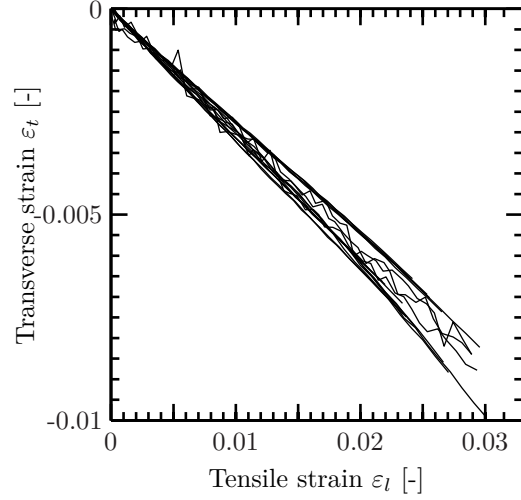
Figure 2.18: Strain in tensile direction versus transverse direction of all 17 samples. The 3 curves at -35°C exhibit noise due to a poor calibration of the DIC-system.
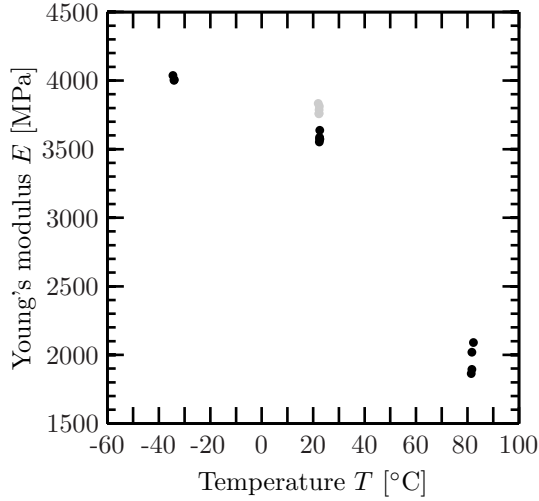
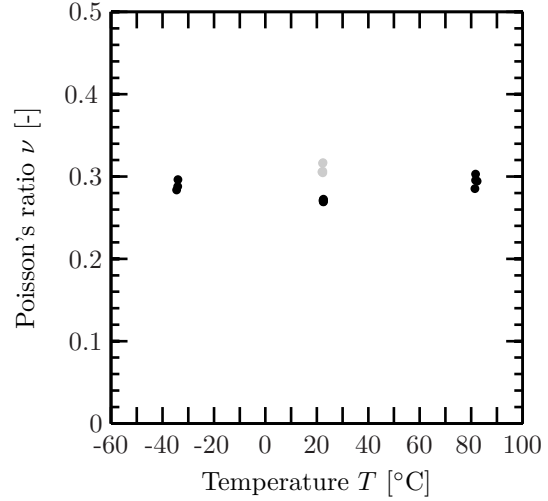Figure 2.19: Young's moduli determined from Fig. 2.17: 20°C (5 samples), 20°C transverse (5, gray symbols), 80°C (4), -35°C (3).

Figure 2.20: Poisson's ratio determined from Fig. 2.18: 20°C (5 samples), 20°C transverse (5, gray symbols), 80°C (4), -35°C (3).

Table 2.7: Elastic properties of Isovolta Icosolar 2442 from tensile testing with mean value and largest distance to minimum or maximum value.

	$-35°C$ 3 samples	$20°C$ 5 samples	$80°C$ 4 samples	$20°C$ transverse 5 samples
E [MPa]	4015.0 ± 21.81	3584.5 ± 53.2	1966.9 ± 123.4	3790.4 ± 43.2
ν [-]	0.289 ± 0.007	0.271 ± 0.002	0.295 ± 0.009	0.301 ± 0.007
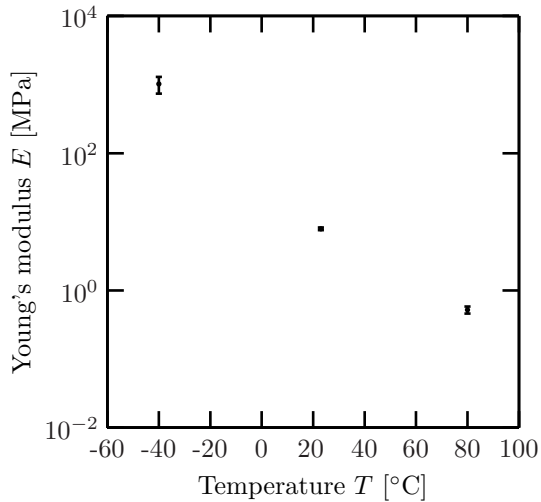
Figure 2.21: Young's modulus of Etimex Vistasolar 496.10 at different temperatures. The logarithmic y-axis reveals the strong time-dependence.
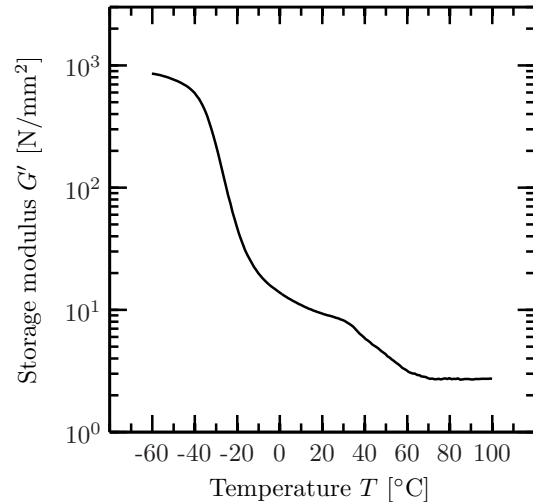
Figure 2.22: Dynamic mechanical analysis of Etimex Vistasolar 496.10 at 1 Hz. The elastic part G' of the shear modulus is shown.

2.3.5 Lamination sheets

EVA (ethylene vinyl acetate) is today's most used lamination material for photovoltaic modules. Here the commercially available product Etimex Vistasolar 496.10 is investigated. Like all other EVA-based products for photovoltaic encapsulation it contains additional substances, such as peroxides, UV-stabilizers and antioxidants. In this context the name EVA is used for the product, not for the bare polymer. The material is delivered in form of a rolled 0.5 mm thick sheet. Before lamination EVA is a thermoset in solid form. It consists of long polymer chain molecules of polyethylene and vinyl acetate. During lamination the material first softens and begins then to crosslink. During this process the carbon atoms of different chains are chemically bonded together so that a network structure forms. The laminated material can then be regarded as one large molecule. When the network structure forms the mechanical stiffness increases. After lamination the EVA is classified as an elastomer. Crosslinking is an irreversible process which means that a laminated EVA sheet cannot soften again without a destruction of the covalent atomic bonds. Unlike thermosets it can thus not be reshaped.

Mechanical properties

We determine the elastic properties of the laminated EVA. Two layers of 0.5 mm thick EVA are laminated together under standard lamination conditions (holding 150°C laminator temperature for 11 min) and are then tensile tested. The testing procedure is the same as for the back sheet described in Section 2.3.4. An examination for anisotropy is not carried out in detail as preliminary tension tests at room temperatures give no relevant anisotropic effects. The experiments at different temperatures are conducted at the Fraunhofer Institute for Mechanics of Materials (FhG IWMH) in Halle(Saale), Germany.
The resulting values of the Young's modulus, that are depicted in Fig. 2.21 and given in Table 2.8, reveal a strong temperature dependence of the mechanical material behavior. Unphysically high values above 0.5 are measured for the Poisson's ratio. The only reasonable explanation is a measurement inaccuracy. Otherwise the volume of the material has to expand under tensile deformation. In contrast to the E-values for the back sheet material, the Young's modulus of the

31

Figure 2.23: Interconverted curve for the Young's modulus E from G'. The black curve uses $\nu = 0.4$ for interconversion, the gray symbols show the interconverion with $\nu = 0.35$ (lower) and $\nu = 0.45$ (upper). The values from tensile testing (Fig. 2.21) are shown for comparison.
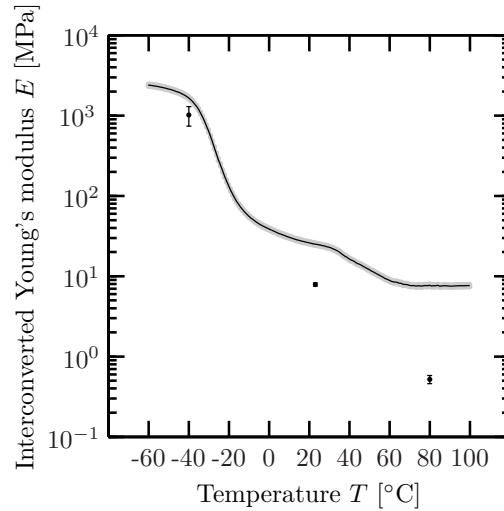
measured EVA changes by several orders of magnitude, so the question arises in what form of curve these three points have to be linked to adequately describe the material's behavior over temperature. A measurement that provides additional experimental values in between is necessary.

Therefore, a second experiment is conducted to obtain a curve for the material's stiffness. A commonly used technique for polymeric materials is the dynamic mechanical analysis (DMA). This DMA-experiment has been conducted at the German Institute of Rubber Technology (DIK) in Hanover. An exact description of the experimental method is given in the book from Grellmann [52]. A strip of laminated EVA is clamped in a tensile configuration. The sample is held under constant tension of 1 N while the upper sample holder dynamically rotates around the tensile axis. The material is thus strained periodically up to 1.5 %. The loading frequency is 1 Hz and the moment that is needed to deform the sample in torsion is monitored. In addition, the experiment is started at -60°C and the temperature is slowly raised (1°C/min) until 100°C.

The experimental result is shown in Fig. 2.22. The depicted quantity, the storage modulus in shear G', is the proportionality constant between implied shear strain and the material's instantaneous response in shear stress due to periodic loading. It is obvious from the curve of G' that the EVA crosses its glass transition region around -30°C as the modulus rises by orders of magnitude. The exact determination of the glass transition temperature, that is according to Ehrenstein [35] the inflection point of the linearly plotted G'-curve, gives $T_{\mathrm{G}} = -35.16$°C. Under the assumption of linear elasticity the transformation of the G'-curve to an E-curve is realized by using the interconversion formula $E(T) = 2G'(T)(1 + \nu)$ from Table 2.1. Poisson's ratio is set constant over temperature, i.e. $\nu = 0.4$. When using higher and lower values for Poisson's ratio in the interconversion, no significant change in E is found, as $\nu = 0.35$ and $\nu = 0.45$ lead to the gray points in Fig. 2.23. The depicted values for E from shear and tension do not match exactly on the logarithmic scale. Reasons could be the usual discrepancy for results in different loading conditions (tension and torsion) or the fact that the EVA samples for the DMA are laminated in a different run than the samples for tensile testing.

Table 2.8: Elastic properties of Etimex Vistasolar 496.10 from tensile testing with standard deviation.

	-40°C	23°C	80°C
E [MPa]	1019.04 ± 279.57	7.90 ± 0.35	0.52 ± 0.06
ν [-]	0.716 ± 0.116	0.411 ± 0.016	0.509 ± 0.036

For the linear elastic simulations in Section 4.3 we use the minimal and maximal value for E from Fig. 2.23 which is 6.5 MPa at 100°C and 2.1 GPa at -60°C. Poisson's ratio is set to 0.4. For the temperature-dependent linear elastic material model in Section 4.3 we use the information of the complete curve in Fig. 2.23 for the Young's modulus E while ν remains at 0.4.

In the DMA experiment it is found that the material exhibits a delay in response to the implied strain, which is expressed by the loss modulus G''. This time-dependent material behaviour cannot be modeled within the frame of linear elasticity, as the time is not incorporated in the constitutive equation. Therefore, a viscoelastic material description of EVA is needed that is thoroughly discussed in Chapter 3.

Chapter 3

Viscoelastic modeling of lamination sheets

The encapsulation material EVA(Ethylene-Vinyl-Acetate) is a polymeric material whose mechanical behaviour cannot be entirely described by a single stress-strain-curve. This fact is illustrated in Fig. 3.1 where a linear elastic analysis of two curves with different loading velocities would lead to two different elastic moduli for the same material.

The stress-strain-relation of such materials is thus dependent on time. Another aspect of polymeric materials such as EVA is a strong dependance of the mechanical material properties on temperature as shown in Fig. 3.2. The corresponding material theory that accounts for the time- and temperature-dependent behavior is called viscoelasticity. Many textbooks contain introductions to the principles of viscoelasticity, such as [22, 35, 56, 73, 82, 100, 138]. Textbooks that exclusively adress the topic of viscoelasticity have been published by Ferry [44], Macosko [78], Nielsen [89], Shaw [110], Tschoegl [123] or Wineman [130] among others.

Typical tests to determine the viscoelastic properties are retardation and relaxation tests or dynamic mechanical analyses (DMA) [74]. In retardation tests, also called creep tests, the material is exposed to a step in stress and the relaxing strain response is monitored over time. In a relaxation test, a step in strain is applied and the transient decay in stress is monitored. During a dynamic mechanical analysis the material is periodically loaded and the response signal is separated in the instantaneous in-phase part and the delayed out-of-phase part. The in-phase signal corresponds to the elastic behavior and the out-of-phase signal to the viscous behavior of the material. During a viscoelastic experiment with a DMA usually the frequency or temperature is varied to cover a wide range of the viscoelastic material behavior in one test. Figure 3.2 is the result of a DMA with a temperature sweep from -60°C to 150°C. The storage modulus G' represents the material parameter for the instantaneous elastic response.

3.1 Linear viscoelasticity

Applying a uniaxial tensile step strain ε_0 to a viscoelastic material (relaxation test) leads to a step in stress followed by a stress decay $\sigma(t)$ over time. The tensile relaxation modulus E is then defined as

$$E(t) = \frac{\sigma(t)}{\varepsilon_0}.$$

If $E(t)$ is known, the stress response to a given constant strain ε_0 that is instantaneous applied at time t_0 can be determined by

$$\sigma(t) = E(t - t_0)\,\varepsilon_0.$$
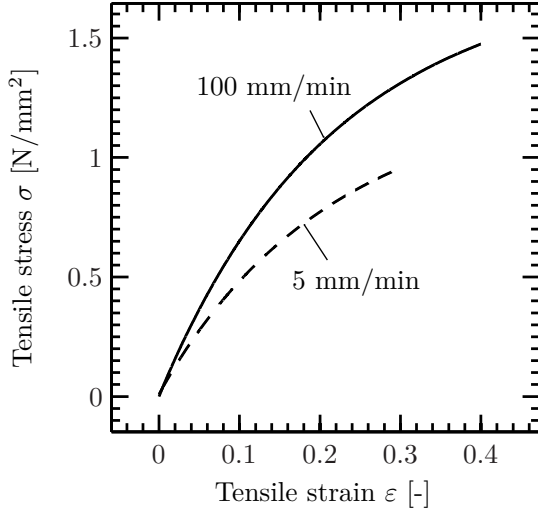
Figure 3.1: Stress-strain-curve of cured EVA for different elongation velocities.
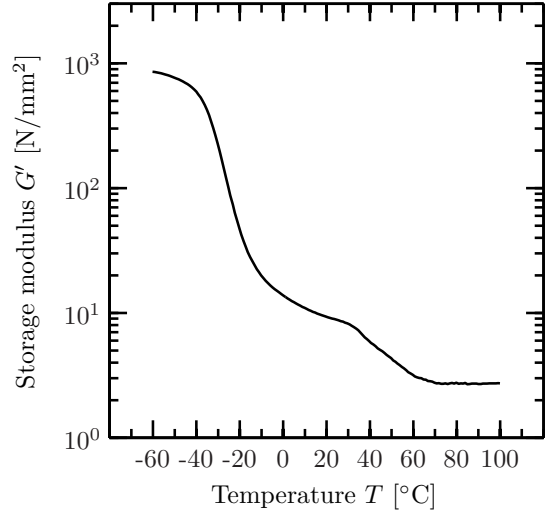
Figure 3.2: Elastic response of cured EVA in a dynamical mechanical analysis with a temperature sweep

In a retardation test, where a constant stress σ_0 is applied, the corresponding material parameter is the tensile creep compliance D, defined as

$$D(t) = \frac{\varepsilon(t)}{\sigma_0},$$

and it holds analogously

$$\varepsilon(t) = D(t - t_0)\,\sigma_0.$$

The linear elastic relationship $E = 1/D$ does not hold true in viscoelasticity, i.e. $E(t) \neq 1/D(t)$. A material is called linear viscoelastic as long as the stress and strain functions are linear,

$$\sigma(\alpha\varepsilon_1(t) + \beta\varepsilon_2(t)) = \alpha\sigma(\varepsilon_1(t)) + \beta\sigma(\varepsilon_2(t))$$

and

$$\varepsilon(\alpha\sigma_1(t) + \beta\sigma_2(t)) = \alpha\varepsilon(\sigma_1(t)) + \beta\varepsilon(\sigma_2(t)).$$

The linearity is used to derive viscoelastic constitutive equations which account for arbitrary stress and strain signals. Let us approximate a continuous strain function $\varepsilon(t)$ up to time t by a series of small strain steps $\varepsilon(t) = \sum_{i=0}^{n} \Delta\varepsilon_i$ with a corresponding discretization of time $t_0 = 0, \ldots, t_n = t$. The stress at time t which is induced by the single strain step $\Delta\varepsilon_i$ at time t_i is

$$\sigma_i(t) = E(t - t_i)\Delta\varepsilon_i.$$

According to linearity, the total stress at time t resulting from all strain steps can be expressed as

$$\sigma(t) = \sum_{i=0}^{n} \sigma_i(t) = \sum_{i=0}^{n} E(t - t_i)\,\Delta\varepsilon_i.$$

For $n \to \infty$ the discretization converges to the original strain function and the expression for the stress approaches the integral

$$\sigma(t) = \int_0^t E(t - u)\,\dot{\varepsilon}(u)\,du \tag{3.1}$$

which represents the viscoelastic constitutive equation. The same holds true for the calculation of strain from a stress input,

$$\varepsilon(t) = \int_0^t D(t - u)\,\dot{\sigma}(u)\,du.$$

In three dimensions, the stress tensor $\boldsymbol{\sigma}(t)$ can be expressed by the viscoelastic tensor $\boldsymbol{C}(t)$ and the strain tensor $\boldsymbol{\varepsilon}(t)$ by

$$\boldsymbol{\sigma}(t) = \int_0^t \boldsymbol{C}(t-u)\,\dot{\boldsymbol{\varepsilon}}(u)\,du.$$

For isotropic viscoelastic materials the constitutive equation can be formulated in terms of the shear relaxation modulus $G(t)$ and bulk relaxation modulus $K(t)$,

$$\boldsymbol{\sigma}(t) = 2\int_0^t G(t-u)\,\dot{\boldsymbol{\varepsilon}}(u)\,du + \int_0^t \left(K(t-u) - \frac{2}{3}G(t-u) \right) \mathrm{tr}(\dot{\boldsymbol{\varepsilon}}(u))\,du. \tag{3.2}$$

Both $G(t)$ and $K(t)$ are then scalar functions of time. In general, the assumption of linearity is valid for polymers up to small strains in the range of a few percent. Above that level non-linear viscoelastic behavior starts. The viscoelastic modeling techniques used in this work are all restricted to linear viscoelasticity.

3.2 Constitutive models

A linear viscoelastic material is fully described, if the material functions in $\boldsymbol{C}(t)$ are known. Regarding the relaxation modulus in 1D, a set of parameters is needed that characterizes $E(t)$. Usually a combination of elastic and viscous elements are used to create $E(t)$. In elasticity, a Hookean solid obeys

$$\sigma_e(t) = E\,\varepsilon_e(t) \tag{3.3}$$

where a constant E symbolizes a spring, while a viscous fluid is described by

$$\sigma_v(t) = \eta\,\dot{\varepsilon}_v(t) \tag{3.4}$$

with the parameter η for the corresponding dashpot.

3.2.1 Maxwell model

Setting a spring and a dashpot in series [100],

$$\sigma(t) = \sigma_e(t) = \sigma_v(t),$$
$$\varepsilon(t) = \varepsilon_e(t) + \varepsilon_v(t),$$

and using Eqs. (3.3) and (3.4) leads to

$$\dot{\varepsilon}(t) = \dot{\varepsilon}_e(t) + \dot{\varepsilon}_v(t) = \frac{\dot{\sigma}(t)}{E} + \frac{\sigma(t)}{\eta},$$
$$\eta\dot{\varepsilon}(t) = \sigma(t) + \tau\dot{\sigma}(t), \quad \tau := \eta/E.$$

If this model is subjected to a step in strain ε_0 at $t = 0$ the differential equation above becomes

$$\sigma(t) + \tau\dot{\sigma}(t) = 0, \quad \sigma(t=0) = E\varepsilon_0.$$

The resulting relaxation modulus is

$$E(t) = \frac{\sigma(t)}{\varepsilon_0} = E\exp\left(-\frac{t}{\tau}\right).$$
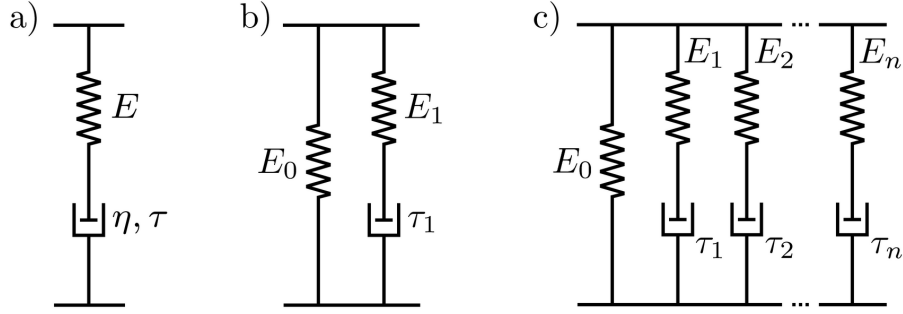
Figure 3.3: Spring-dashpot models: Maxwell model (a), 3-parameter solid (b) and generalized Maxwell model (c)

This so-called Maxwell model consists of the two parameters E and τ to characterize the material function $E(t)$. The creep compliance of the Maxwell model is

$$D(t) = \frac{t}{\tau E} + \frac{1}{E}.$$

It holds $\lim_{t \to \infty} E(t) = 0$ and it can thus not describe materials that converge to a stress value above 0 in a relaxation experiment. As $D(t)$ is a straight line it is not well suited to describe materials with a curve-shaped strain response in a creep test.

3.2.2   3-parameter solid

Adding a spring in parallel to the Maxwell model as shown in Fig. 3.3 leads to the model equations

$$E(t) = E_0 + E_1 \exp\left(-\frac{t}{\tau_1}\right),$$

$$D(t) = \frac{1}{E_0} + \left(\frac{1}{E_0 + E_1} - \frac{1}{E_1}\right) \exp\left(-\frac{t}{\tau_1} \frac{E_0}{E_0 + E_1}\right),$$

which is known as the 3-parameter solid [123]. It is able to reproduce the stress relaxation to a positive value as $\lim_{t \to \infty} E(t) = E_0$ and $D(t)$ shows a curve-shaped behavior. However, the double logarithmic plot of $E(t)$ reveals the steep slope in the transition region (Fig. 3.4) and thus the poor ability to reproduce experimental curves of polymers for $E(t)$.

3.2.3   Generalized Maxwell model

The generalized Maxwell model is an extension of the 3-parameter solid by addition of supplementary Maxwell elements [123]. Each Maxwell element is called a Maxwell arm in the model. The number of Maxwell arms defines the structure of this parametrization of $E(t)$. For n arms, one obtains the expression

$$E(t) = E_0 + \sum_{i=1}^{n} E_i \exp\left(-\frac{t}{\tau_i}\right),$$

which is referred to as a Prony series [123]. An explicit analogical expression for $D(t)$ in terms of E_i and τ_i does not exist. It is possible to obtain $D(t)$ from $E(t)$ by so-called interconversion which
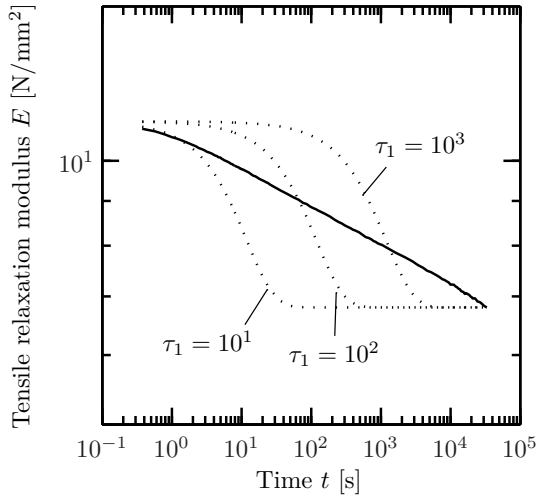
Figure 3.4: $E(t)$ of EVA measured at 20°C and fitting with 3-parameter solid for different values of τ_1
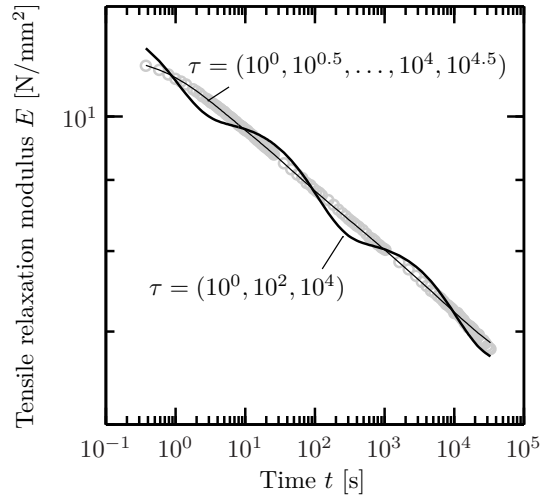
Figure 3.5: Measured E(t) at 20°C and fits with a 3-arm and a 10-arm generalized Maxwell model

involves numerical methods. In practice, the values for τ_i are chosen, for example one per decade, and the $n+1$ unknown values E_i are obtained from fitting the Prony series to the experimental curve of $E(t)$. Every Maxwell arm has a local impact on the shape of $E(t)$. τ_i defines the range of that impact within t and E_i sets the height of the model curve. If the distance between the τ_i is too large the curve takes a wave-like shape as shown in Fig. 3.5. A large number of Maxwell arms, such as 1 or 2 per decade, does thus not overfit the experimental data provided that enough data are present per decade. The Prony series for $E(t)$ can be regarded as an approximative discretization of the experimental curve. A possible interpretation of the model for polymeric materials is that each Maxwell arm corresponds to the mechanical behavior of all molecular chains with a certain length.

It has to be pointed out that fitting an experimental curve with a Prony series is not a straight forward task. First, as the curves are usually drawn on a double logarithmic scale, a simple least squares fit approximates the experimental data on a non-logarithmic scale and small values do not contribute to the fit. Second, all Prony coefficients have to be positive. The fitting algorithm becomes thus a constrained least squares problem. Several methods to find the Prony coefficients are presented in the literature, such as the Procedure X [123], the Collocation Method [123], the Multidata Method [123], the algorithm of Emri and Tschoegl [120], [121], [40], the method by Bradshaw and Brinson [15] and the method by Sorvari and Malinen [114].

The reason for the common use of the generalized Maxwell model over model functions for $E(t)$ with less fit parameters is the fact that the form of the Prony series is very convenient for Finite-Element-Simulations. For modeling isotropic viscoelastic materials in 3D, FEM programs like Comsol Multiphysics require the input of the shear relaxation modulus $G(t)$ in terms of (τ_i, G_i) and a constant bulk modulus $K \neq K(t)$. The respective assumption is that K does not depend on time and that $K(t) \gg G(t)$, so that the viscoelastic constitutive equation (3.2) becomes

$$\boldsymbol{\sigma}(t) = 2 \int_0^t G(t-u)\,\dot{\boldsymbol{\varepsilon}}(u)\,du + K\,\mathrm{tr}(\boldsymbol{\varepsilon}(t)).$$

This assumption has been found to be quite reasonable for most viscoelastic materials. In fact, the differences between polymers and solids are not so striking in compression as in shear [44].

3.3 Relaxation and retardation experiments of EVA

Relaxation and retardation measurements of EVA are conducted at different constant temperatures to determine its viscoelastic properties. The preparation of the EVA specimens includes the lamination of several layers of uncured EVA to a sheet with a thickness of approximately 1.6 mm, followed by cutting out the single specimens with the help of a cutting template which has the form of the tensile testing standard ASTM D638 Type I. The thickness of each piece is measured at three points of the narrow section. Afterwards the speckle pattern is sprayed onto the specimens, first a thin white layer and the speckles in black on top.

The experimental setup is shown in Fig. 2.16. A specimen is clamped in the top holder of the tensile testing machine so that the force can then be set to zero thus eliminating the weight of the specimen in the force signal. When both clamps are closed the upper clamp is moved down to reduce the clamp distance. That avoids a loading of the specimen due to contraction when the chamber is cooled down to low testing temperatures. The climate chamber is piloted to the desired temperature and the experiment starts as soon as a the temperature reaches a stable plateau which is measured at the specimen directly. The tensile test machine stretches the specimen up to a small specified pre-load. The calibrated stereo-camera system is then toggled to start recording the strain, first at time intervals of 200 ms which are in the course of the experiment stepwise increased up to 10 min. The user's input starts the experiment and the tensile tester ramps up to the specified force or elongation within 2 s. The force resp. the elongation is then held constant. During the experiment the temperature T, the time t, the force F and the traverse path s are recorded. The stereo images from the digital image correlation system are postprocessed after the experiment to create the longitudinal and transverse strain values ε_l and ε_t. The strain signals are shifted in time until the longitudinal strain matches the course of the traverse path s during the short loading period. As the density in the force data is much higher than the strain data, the force and the temperature are interpolated in the times of the strain data. This set of data $(t, T(t), F(t), \varepsilon_l(t), \varepsilon_t(t))$ represents the experimental data.

It has to be pointed out that neither the above described procedure of a relaxation test nor of a retardation test are in exact accordance with the theoretical test conditions. First, the ramp differs from a step loading. Second, during the relaxation test not the strain but the traverse path is held constant and during the retardation test the testing machine tries to keep the force constant instead of the stress. However, the experimental data $(t, T(t), F(t), \varepsilon_l(t), \varepsilon_t(t))$ are all directly measured and contain thus only the measurement errors. Within these errors the stress can be calculated from the initial thickness and width (cross-section A_0), the force $F(t)$ and the transverse strain $\varepsilon_t(t)$,

$$\sigma(t) = \frac{F(t)}{A_0(\varepsilon_t + 1)^2}.$$

Due to the reasons outlined above the moduli from these experiments are defined as

$$\hat{E}(t) = \frac{\sigma(t)}{\varepsilon_l(t)} \quad \text{and} \quad \hat{D}(t) = \frac{\varepsilon_l(t)}{\sigma(t)}$$

and their shape is shown in Figs. 3.6 and 3.7 for the different temperatures. The ramp of 2 s is cut.

3.4 Interconversion between different deformation modes

The measured data from relaxation and creep experiments as described in Section 3.3 are determined from a tensile deformation mode. In the FEM-programs like Comsol Multiphysics or Abaqus the input of an isotropic viscoelastic material is required in terms of the shear modulus $G(t)$ and the bulk modulus K. Therefore, the tensile data have to be interconverted to data in a shear deformation mode before they can be fitted to the generalized Maxwell model. Furthermore,
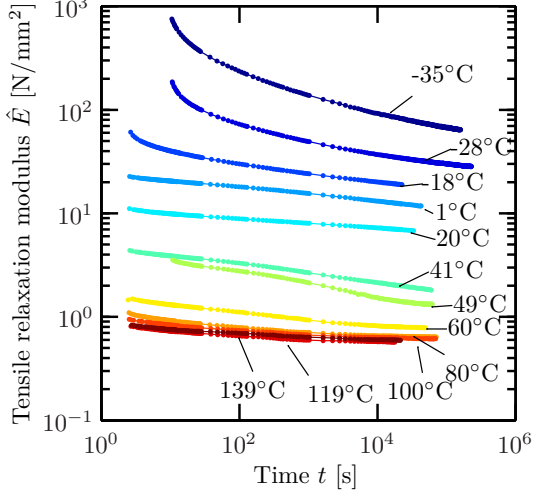
Figure 3.6: Tensile relaxation moduli for laminated EVA at different constant temperatures
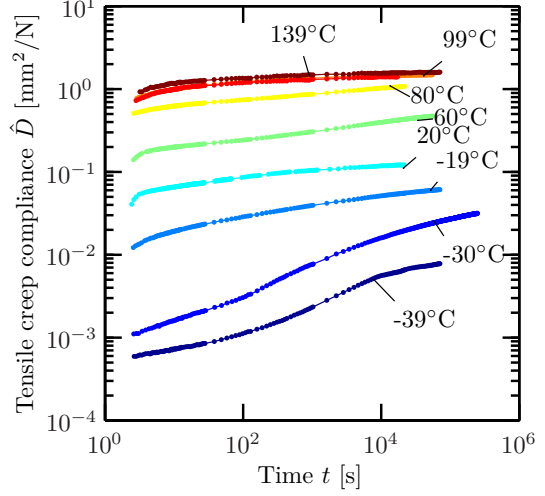

Figure 3.7: Tensile creep compliance for laminated EVA at different constant temperatures

to use the retardation test data for the construction of a model for the shear relaxation modulus, an interconversion from creep data to relaxation data is required.

3.4.1 Use of the elastic-viscoelastic correspondence principle

In linear elasticity, a pair of elastic parameters such as (E, ν), (G, K) or (μ, λ) uniquely defines the mechanical behavior of an isotropic material in three dimensions, see Table 2.1. In a uniaxial tensile test (Fig. 3.8), like the EVA relaxation and creep tests described above, it holds

$$\boldsymbol{\sigma} = \begin{bmatrix} \sigma_{11} & 0 & 0 \\ 0 & 0 & 0 \\ 0 & 0 & 0 \end{bmatrix} \quad \text{and} \quad \boldsymbol{\varepsilon} = \begin{bmatrix} \varepsilon_{11} & 0 & 0 \\ 0 & \varepsilon_{22} & 0 \\ 0 & 0 & \varepsilon_{22} \end{bmatrix}$$

and thus the universal linear elastic equation written for every component

$$\sigma_{ij} = 2\,G\varepsilon_{ij} + (K - 2/3\,G)(\varepsilon_{11} + \varepsilon_{22} + \varepsilon_{33})\delta_{ij}$$

takes the forms

$$0 \neq \sigma_{11} = (K + 4/3\,G)\varepsilon_{11} + (2K - 4/3\,G)\varepsilon_{22},$$
$$0 = \sigma_{22} = (K - 2/3\,G)\varepsilon_{11} + (2\,K + 2/3\,G)\varepsilon_{22}.$$

According to the elastic-viscoelastic correspondence principle the viscoelastic stress-strain relations can be brought to the same form as the elastic forms by the use of Laplace transforms [22, 123], so that it holds

$$\bar{\sigma}_{11}(s) = s\left(\bar{K}(s) + 4/3\,\bar{G}(s)\right)\bar{\varepsilon}_{11}(s) + s\left(2\bar{K}(s) - 4/3\,\bar{G}(s)\right)\bar{\varepsilon}_{22}(s),$$
$$0 = s\left(\bar{K}(s) - 2/3\,\bar{G}(s)\right)\bar{\varepsilon}_{11}(s) + s\left(2\,\bar{K}(s) + 2/3\,\bar{G}(s)\right)\bar{\varepsilon}_{22}(s),$$

where the bar denotes the Laplace transform

$$L(f) = \bar{f}(s) = \int_0^\infty f(t)\exp(-st)\,dt.$$
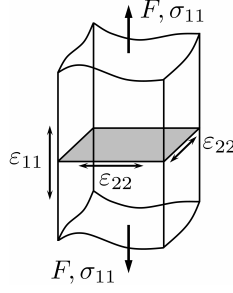
Figure 3.8: Tensile test of an isotropic material.

Rearranging the above equations leads to expressions of the bulk and shear moduli

$$\bar{\sigma}_{11}(s) = 2s\,\bar{G}(s)\,(\bar{\varepsilon}_{11}(s) - \bar{\varepsilon}_{22}(s)),\tag{3.5}$$

$$\bar{\sigma}_{11}(s) = s\,\bar{K}(s)\,(3\bar{\varepsilon}_{11}(s) + 6\bar{\varepsilon}_{22}(s)),\tag{3.6}$$

which can then be inverse Laplace transformed via

$$L^{-1}(s\bar{g}(s)\bar{f}(s)) = g(t)f(0) + \int_0^t g(u)\frac{df(t-u)}{d(t-u)}\,du$$

resulting in expressions for the unknowns $G(t)$ and $K(t)$,

$$\sigma_{11}(t) = 2\,G(t)\,(\varepsilon_{11}(0) - \varepsilon_{22}(0)) - 2\int_0^t G(u)\frac{d\,(\varepsilon_{11}(t-u) - \varepsilon_{22}(t-u))}{du}\,du,\tag{3.7}$$

$$\sigma_{11}(t) = K(t)\,(3\varepsilon_{11}(0) + 6\varepsilon_{22}(0)) - \int_0^t K(u)\frac{d\,(3\varepsilon_{11}(t-u) + 6\varepsilon_{22}(t-u))}{du}\,du.\tag{3.8}$$

From the relaxation and creep tests the values for $\varepsilon_{11}(t)$, $\varepsilon_{22}(t)$ and $\sigma_{11}(t)$ are known. However, Eqs. (3.7) and (3.8) cannot be rearranged for a direct determination of $G(t)$ and $K(t)$.

3.4.2 Recursive interconversion formula

Numerical interconversion formulas are needed to solve Eqs. (3.7) and (3.8) which calculate the values of G and K from discrete test data [123]. We examine a general form of Eqs. (3.7) and (3.8), i.e.

$$\sigma(t) = c\,A(t)f(0) - c\int_0^t A(u)\frac{df(t-u)}{du}\,du.\tag{3.9}$$

In case of Eq. (3.7), we assign

$$A(t) = G(t), \quad c = 2, \quad f(t) = \varepsilon_{11}(t) - \varepsilon_{22}(t),$$

and in case of Eq. (3.8)

$$A(t) = K(t), \quad c = 1, \quad f(t) = 3\varepsilon_{11}(t) + 6\varepsilon_{22}(t).$$

Now, let $\{t_1 = 0, t_2, \ldots, t_N = t\}$ be a discretization of time where the values of A and f are given. If we numerically approximate the integral term in Eq.(3.9) with the trapezoidal rule we obtain the recurrence formula

$$A(t_n) = \frac{\sigma(t_n) + 1/2\,c\,A(t_1)\,[f(t_n - t_2) - f(t_n)] + 1/2\,c\,\sum}{1/2\,c\,f(0) + 1/2\,c\,f(t_n - t_{n-1})},\tag{3.10}$$

$$\sum = \sum_{i=2}^{n-1} A(t_i)\,[f(t_n - t_{i+1}) - f(t_n - t_{i-1})], \quad A(t_1) = \frac{\sigma(t_1)}{c\,f(0)},$$
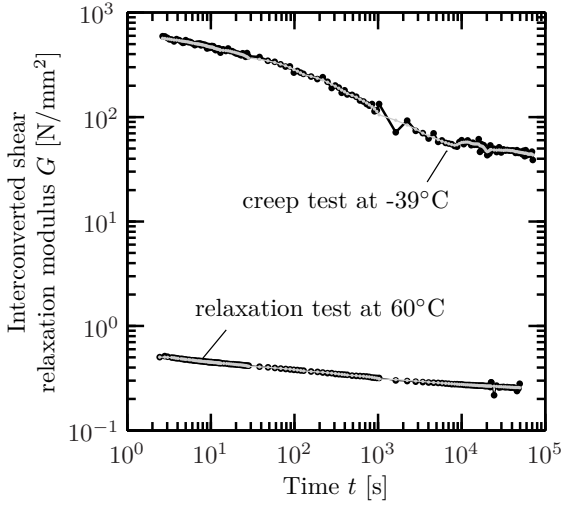
Figure 3.9: Interconversion of two different experiments via recurrence formula (3.10) (black) and regularized formulation (3.11) (gray).
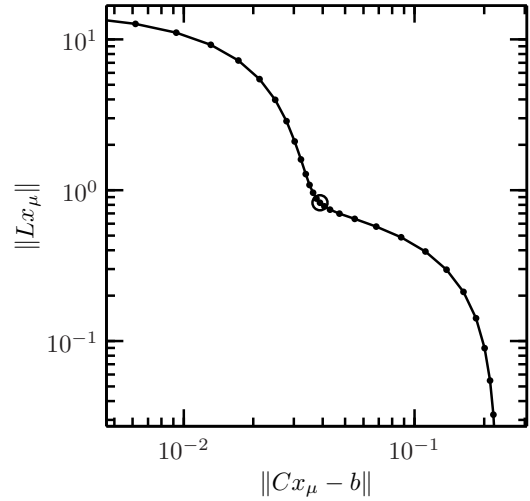
Figure 3.10: L-curve method to determine the regularization parameter μ.

which has to be evaluated for all t_n $(1 < n \leq N)$ to determine $A(t)$. In the experiments, the points in time t_n are not equally spaced because a viscoelastic analysis involves logarithmic time scales. As a consequence, values in between two points in time, for example $f(t_n - t_{i+1})$, have to be interpolated within the numerical interconversion procedure.

However, as reported in the literature [79, 90, 114, 113] and shown in Fig. 3.9, these interconversion techniques imply solving ill-posed problems. Sorvari [114, 113] proposes to use Tikhonov regularization to stabilize the conversion of experimental viscoelastic data. The suggested procedure cannot be used in this case because in contrast to Sorvari the experimental data are not given in equidistant times. Here, an interconversion formulation is developed that transforms the recurrence formula to a matrix-vector expression where the Tikhonov regularization is then applied. Writing Eqs. (3.10) in matrix form $Cx = b$ results in

$$C_{kl} = \frac{1}{2}\, c \begin{cases} 0, & l > k \\ 2f_{11}, & l = k = 1 \\ f_{k1} - f_{k2}, & l = 1, k \neq 1 \\ f_{k,k-1} + f_{kk}, & l = k \neq 1 \\ f_{k,l-1} - f_{k,l+1}, & 2 \leq l < k \end{cases} \quad \text{with} \quad f_{ij} = f(t_i - t_j),$$

and the vectors x and b become

$$b_k = \sigma(t_k)$$

and

$$x_k = A(t_k).$$

Instead of solving $Cx = b$ directly for the unknowns $x_k = A(t_k)$, which is the same as solving the recurrence formula (3.10), the linear system is regularized by the help of the $(N-1) \times N$-matrix

$$L = \begin{pmatrix} -1 & 1 & & 0 \\ & \ddots & \ddots & \\ 0 & & -1 & 1 \end{pmatrix}$$

so that the regularized problem formulation becomes

$$\min_{x_\mu} \left\{ \|Cx_\mu - b\|^2 + \mu \|Lx_\mu\|^2 \right\}.$$

43

This is equivalent to

$$x_\mu = \left(\mu L^T L + A^T A\right)^{-1} A^T b. \tag{3.11}$$

The regularization parameter μ is chosen with the help of the L-curve method. For different μ, Eqs. (3.11) is solved and the norm $\|Lx_\mu\|$ is plotted versus $\|Cx_\mu - b\|$ on a loglog-scale (Fig. 3.10). The value of μ that corresponds to the lower left hand corner of the curve is chosen as the regularization parameter. While this interconversion procedure works well for the determination of the shear relaxation modulus $G(t)$ from the data shown in Section 3.3, the interconversion from the same tensile experimental data to the bulk modulus $K(t)$ fails. It is clear from the deduction of the interconversion Eqs. (3.7) that the interconverted G is, within the range of numerical errors, the real shear relaxation modulus. The fact, that the experiments from Section 3.3 are not in exact accordance with theoretical testing procedure does not affect the determination of $G(t)$ as measured $\varepsilon_l(t), \varepsilon_t(t), \sigma(t)$ are used.

3.5 Time-temperature superposition

In the previous sections the discussed modeling techniques involved only the time-dependence of the viscoelastic material parameters. As depicted in Figs. 3.2, 3.6 and 3.7 EVA also exhibits a strong sensitivity to temperature. The moduli between 130°C and -30°C differ by about 2 to 3 decades. It is therefore necessary to include the temperature T in the viscoelastic equations, so that Eqs. (3.1) becomes

$$\sigma(t, T) = \int_0^t E(t - u, T)\, \dot{\varepsilon}(u) du.$$

3.5.1 Mastercurve

In 1951 Andrews and Tobolsky [8] published relaxation curves which they combined by using the concept of reduced times. The observation is that by shifting a polymeric relaxation curve along the logarthmic time axis to another curve from a slightly different temperature results in an overlap of both curves. The new curve then coveres a larger time domain at the constant temperature of the unshifted curve. This empirical method is called time-temperature-superposition [130] and has by now become the standard procedure to include temperature in the characterization of polymers [122]. Applying this procedure to several relaxation curves then allows the experimentalist to create a relaxation curve that stretches over a time domain that can practically not be included in one experiment. This new curve is known as a mastercurve. Material where the shifting results in a satisfactory mastercurve is called thermorheologically simple. For thermorheologically complex material this horizontal shifting does not result in a satisfactory overlap.
By assuming EVA to be thermorheologically simple, the shifting to -20°C results in mastercurves that are illustrated in Fig. 3.11 for the tensile relaxation modulus $\hat{E}$ and Fig. 3.12 for the tensile creep compliance $\hat{D}$. This assumption is found to be unsatisfactory fulfilled as the overlap is not in excellent agreement. The interruptions in the curves are due to a lack of certain testing temperatures and the shifting is there done by eye. As EVA is a copolymer and contains semicrystalline parts [57] the superposition is, according to Tschoegl [122], not applicable. However, in the modeling procedure of the viscoelastic behavior of EVA presented here we accept these approximative errors.

3.5.2 Shift factor

Shifting data along the logarithmically scaled time axis corresponds to selecting the modulus value at a different time when the temperature has changed. For two isothermal relaxation curves at
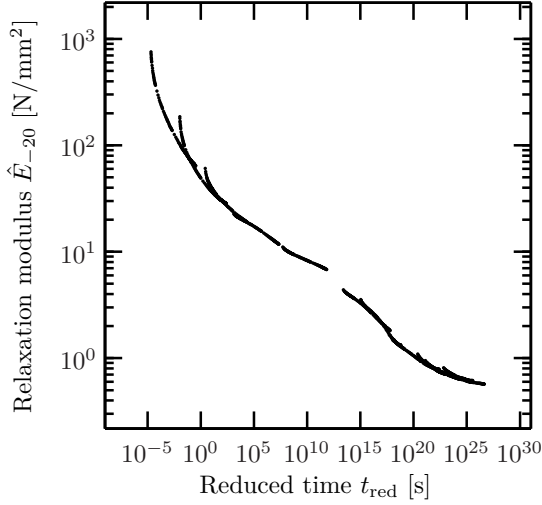
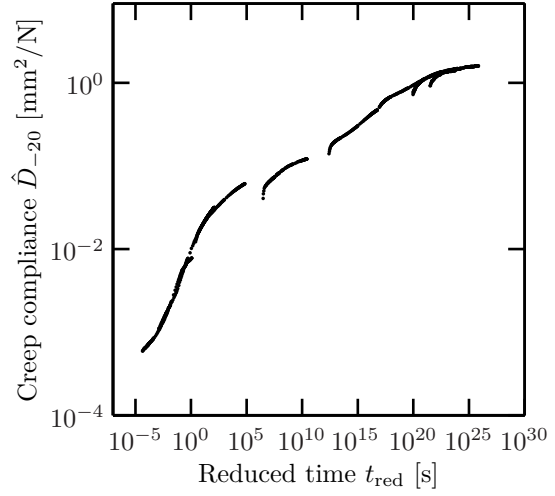Figure 3.11: Mastercurve of EVA for tensile relaxation modulus $\hat{E}$ by shifting to -20°C

Figure 3.12: Mastercurve of EVA for tensile creep compliance $\hat{D}$ by shifting to -20°C

T_{ref} and T_1 the shifting is expressed by

$$E(t, T_1) = E(t/\, \alpha_{T_{\mathrm{ref}}}(T_1), T_{\mathrm{ref}}) = E(t_{\mathrm{red}}, T_{\mathrm{ref}}).$$

How far the relaxation curve at T_1 has to be shifted to reach the curve at T_{ref} is expressed in the shift factor $\alpha_{T_{\mathrm{ref}}}(T)$. The shifted time scale is often called reduced time. For non-isothermal data $T(t)$ the reduced time t_{red} is

$$t_{\mathrm{red}} = \xi(t) = \int_0^t \frac{1}{\alpha_{T_{\mathrm{ref}}}(T(u))} \, du$$

and thus by knowing $\alpha_{T_{\mathrm{ref}}}(T)$ arbitrary temperature profiles can be included in a viscoelastic FEM-simulation.

However, the implementation of the reduced time concept into the viscoelastic constitutive equation is not straight forward. The following derivation of the temperature-dependent viscoelastic constitutive equation is taken from [130]. Let us consider a relaxation test with a step in strain ε_0 applied at $t_0 = 0$ and a subsequent step in temperature applied at time t_1 as shown in Fig. 3.13. The reduced time for $t > t_1$ becomes

$$\xi(t) = \int_0^{t_1} \frac{1}{\alpha_{T_{\mathrm{ref}}}(T_{\mathrm{ref}})} \, du + \int_{t_1}^t \frac{1}{\alpha_{T_{\mathrm{ref}}}(T_1)} \, du = t_1 + \frac{t - t_1}{\alpha_{T_{\mathrm{ref}}}(T_1)}.$$

It follows

$$E(t, T(t)) = E\left(t_1 + \frac{t - t_1}{\alpha_{T_{\mathrm{ref}}}(T_1)}, T_{\mathrm{ref}}\right),$$

which is shown in Fig. 3.14. In analogy to Section 3.1 where the viscoelastic constitutive equation is deduced from a series of relaxation steps, we write the contribution of such a small strain increment $\Delta\varepsilon_i$ applied at time $t_i < t$ to the stress at time t as

$$\sigma_i(t, T(t)) = E\left(\int_{t_i}^t \frac{1}{\alpha_{T_{\mathrm{ref}}}(T(u))} \, du, T_{\mathrm{ref}}\right) \Delta\varepsilon_i = E(\xi(t) - \xi(t_i), T_{\mathrm{ref}}) \, \Delta\varepsilon_i.$$

Splitting an arbitrary strain history $\varepsilon(t)$ with a temperature history $T(t)$ into n small strain steps $\Delta\varepsilon_i$ lets us write the stress $\sigma(t, T(t))$ as

$$\sigma\left(t, T(t)\right) = \sum_{i=0}^n \sigma_i(t) = \sum_{i=0}^n E(\xi(t) - \xi(t_i), T_{\mathrm{ref}}) \, \Delta\varepsilon_i.$$

45
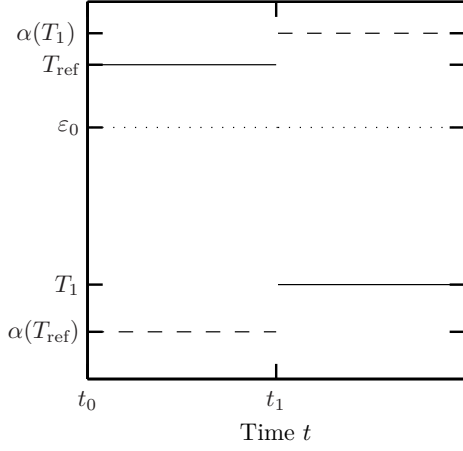
Figure 3.13: Relaxation test with temperature step at time t_1.
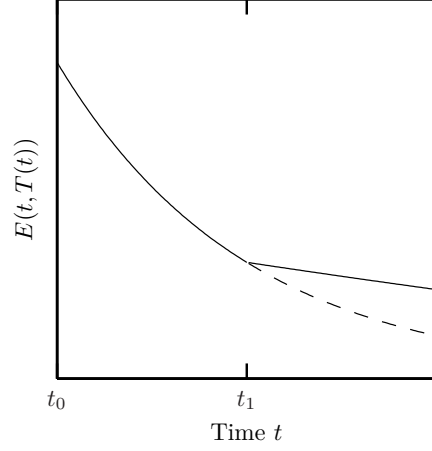
Figure 3.14: Resulting relaxation modulus $E(t)$ for relaxation with temperature step.

For the limit case $n \to \infty$ we obtain the temperature-dependent viscoelastic constitutive equation

$$\sigma(t, T(t)) = \int_0^t E(\xi(t) - \xi(u), T_{\text{ref}}) \, \dot{\varepsilon}(u) \, du.$$

The shift factor is a material property and should thus be the same for relaxation data, creep data and other deformation modes [44]. Different semi-empirical models are available to approximate the shift factor as a funtion of temperature. Below the glass transition temperature T_G of the polymer the Arrhenius model

$$\log_{10} \, \alpha_{T_{\text{ref}}}(T) = \frac{E_A}{2.303R} \left(\frac{1}{T} - \frac{1}{T_{\text{ref}}} \right)$$

is often chosen. E_A is an activation energy and R is the universal gas constant. For temperatures between $T_G - 10$ and $T_G + 100$ the Williams-Landel-Ferry equation [129] is widely used,

$$\log_{10} \, \alpha_{T_{\text{ref}}}(T) = \frac{-C_1(T - T_{\text{ref}})}{C_2 + T - T_{\text{ref}}}.$$

Williams, Landel and Ferry determined $C_1 = 17.44$ and $C_2 = 51.6°C$ as universal parameters if the glass transition temperature is chosen as the reference temperature. In practice C_1 and C_2 are usually treated as fit parameters. For EVA the WLF fit parameters from Fig. 3.15 are given in table 3.1.

Now the temperature dependency of EVA is included in the viscoelastic modeling procedure, so that the viscoelastic model of EVA can be completed by fitting a generalized Maxwell model to the mastercurve depicted in Fig. 3.16. A Prony series with 25 Maxwell arms is chosen in order to cover the reduced time domain up to 10^{22}.

Table 3.1: WLF parameters for EVA.

T_{ref} [°C]	C_1 [-]	C_2 [°C]
-20	48.44	172.55
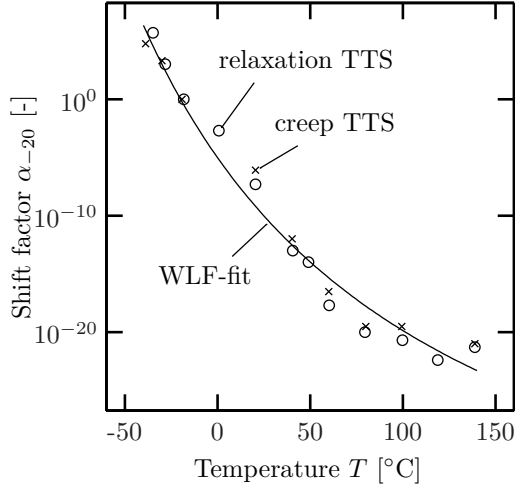
Figure 3.15: Values of α_{-20} from time-temperature-superposition of EVA. (○) represent the values obtained from shifting relaxation curves (Fig. 3.11), (×) from shifting creep curves (Fig. 3.12).
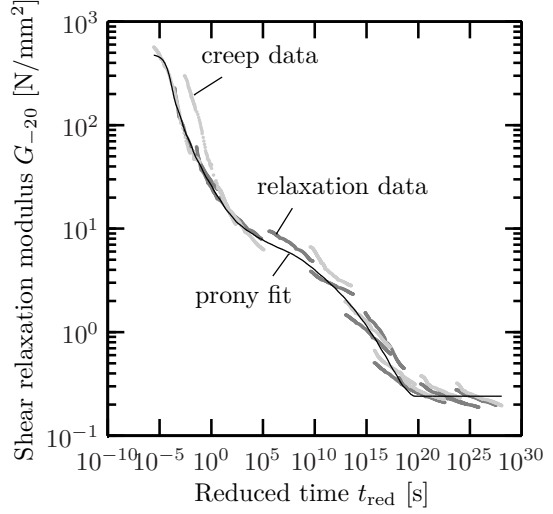
Figure 3.16: Mastercurve and Prony fit of shear modulus G of EVA. Data are interconverted from relaxation and creep experiments and then shifted using the WLF equation.

3.6 Verification of viscoelastic model for EVA

The derivation of a viscoelastic model for EVA as described in the previous sections contains several steps, each of them contributing possible errors to the final model:

1. Determination of relaxation modulus and creep compliance:
   $t, \sigma, \varepsilon_l \rightarrow \hat{E}, \hat{D}$

2. Time-temperature superposition of relaxation and creep functions:
   $t, T, \hat{E}, \hat{D} \rightarrow \alpha_{-20}, C_1, C_2$

3. Interconversion of tensile data to shear relaxation modulus:
   $t, \sigma, \varepsilon_l, \varepsilon_t \rightarrow G$

4. Fitting generalized Maxwell model to mastercurve:
   $t, G, C_1, C_2 \rightarrow G_i, \tau_i$

This section is intended to compare the derived model to the original creep measurement data. Two methods are used to validate the model. First, a FEM-simulation of the tensile experiments and second, an analytical formula similar to (3.7) which is solved numerically.

3.6.1 FEM-simulation

The specimen form ASTM D638 Type I is geometrically modeled in 2D. For each simulation the measured thickness of the specimen and the measured force $F(t)$ is fed to the FEM-program. The discretization of time is chosen to match the experimental points in time. The simulated material is modeled as viscoelastic by using the Prony parameters associated with the curve shown in Fig. 3.16 and the WLF parameters according to table 3.1. The whole experiment is simulated, which means that the complete ramp is included. The results of the simulation are the stress and strain values in the narrow section of the geometry.
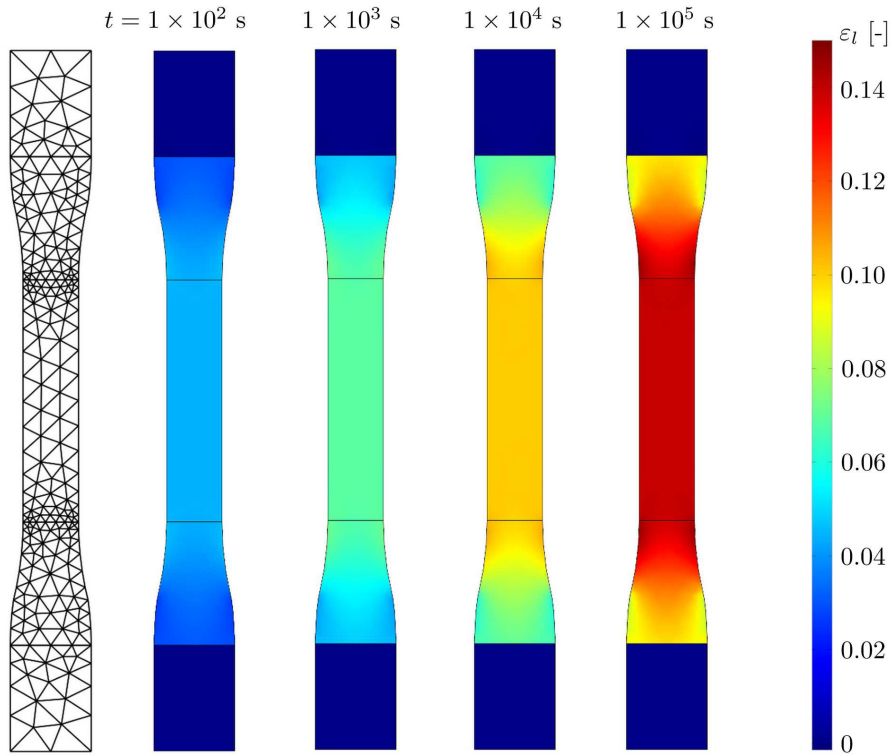
Figure 3.17: Simulation of EVA creep experiment at -30°C, tensile strain at different points in time.
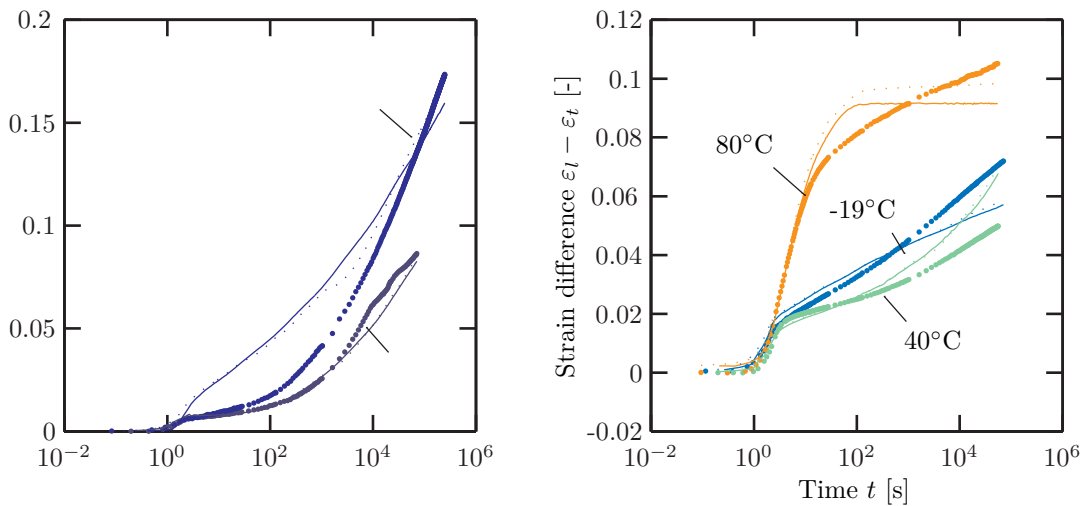
Figure 3.18: Verification of viscoelastic model for EVA: experimental creep data (•), FEM-simulation (−) and analytical formula (···) for different creep experiments

3.6.2   Analytical formula

If the relaxation shear modulus $G(t)$ and the tensile stress $\sigma(t)$ are given, the interconversion procedure from Section 3.4 can be used to determine $\varepsilon_l(t) - \varepsilon_t(t)$. Equation (3.5) which is inverse Laplace transformed to provide formula (3.7) can also be inverse laplace transformed to give

$$\sigma_{11}(t) = 2\,G(0)\,(\varepsilon_{11}(t) - \varepsilon_{22}(t)) - 2\int_0^t \frac{dG(t-u)}{d(t-u)}\,(\varepsilon_{11}(u) - \varepsilon_{22}(u))\ du. \tag{3.12}$$

This expression is then solved for $\varepsilon_l(t) - \varepsilon_t(t)$ by using the regularized formulation (3.11).

The results illustrated in Fig. 3.18 indicate that the analytical formula agrees reasonably with the simulation which thus correctly interprets the viscoelastic model. Two reasons can explain the fact that simulation and analytical formula are not in exact agreement. First, the simulation uses a constant bulk modulus and second the approximative solution of Eq. (3.12) is again prone to numerical error. The difference between the experimental data and simulated/analytically determined data reveals that the modeling cannot reproduce the material behavior of EVA completely. One possible reason is already explained in Subsection 3.5.1 which is the thermorheologically complex behavior of EVA. Another cause could be errors due to non-perfect testing or preparation conditions such as clamping, thickness measurements or non-homogeneous lamination conditions. These errors are contained in the experimental data and can only explain why certain experimental curves deviate significantly from the mastercurve. However, it is obvious that the viscoelastic model can reflect thermomechanical properties of EVA over a large temperature and time range that a simple linear elastic material model cannot.

Chapter 4

Thermomechanical deformation of PV laminates

4.1 Experimental technique for deformation measurements

Standard techniques to measure the mechanical behavior of laminates are strain gauges, which are still the most used experimental method [61], optical (interferometric) methods, photoelasticity (Fiber Bragg Gratings [64, 107]) or, on a microscopic scale, Raman spectroscopy and X-ray diffraction [31]. Both latter techniques are able to measure structure and stress, and for the XRD technique measurements through thin non-transparent laminate layers are possible. However, such methods are very complex, time-consuming and restricted to small measurement regions.

Laminating strain gauges into a PV module has several disadvantages, such as adhesion of the gauge to the lamination sheet over the whole gauge length, a thermal sensitivity of the sensor and only local strain information between two material points. Furthermore, the insertion of strain gauges into the laminate including the necessary wire connections is likely to influence the thermomechanical properties of the laminate itself. The preparation of such test laminates is time-consuming and elaborate.

The optical methods such as interferometry [138, 58] (laser profile interferometry, Moire interferometry, holographic interferometry, speckle interferometry) and digital image correlation [118] have the advantage to measure contactless, non-destructive and to provide full field data. We find the digital image correlation technique with a stereo camera system (3D-DIC or DISC) to be a well suited tool for deformation measurements of in-laminate components because the displacements and strains of the solar cells becomes accessible by viewing through the transparent back sheet and one layer of EVA. Additionally the method is not restricted to special sizes of measurement regions as it only records relative extents and is thus applicable to samples of different scales in size. A disadvantage of the DIC method in combination with a stereo camera system is the limit of strain resolution. That limit is set by the resolution of the cameras. The system that we use here consists of two 5 Mega Pixel CCD cameras which leads to a strain resolution of approximately 100 microstrains. With other methods such as strain gauges, fiber Bragg gratings or laser interferometry much higher resolutions are possible.

4.1.1 Digital image correlation

The method of digital image correlation technique was developed during the 1980's when the progress in computer technology enabled the computation of large data volumes, so that the efficient evaluation of image data became possible [96]. The use of this measurement technique
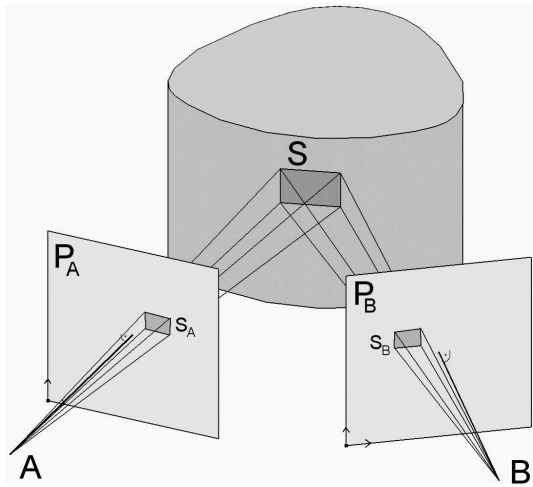
Figure 4.1: Pinhole model for the calculation of the object surface S in three dimensions from two-dimensional camera images P_A and P_B.
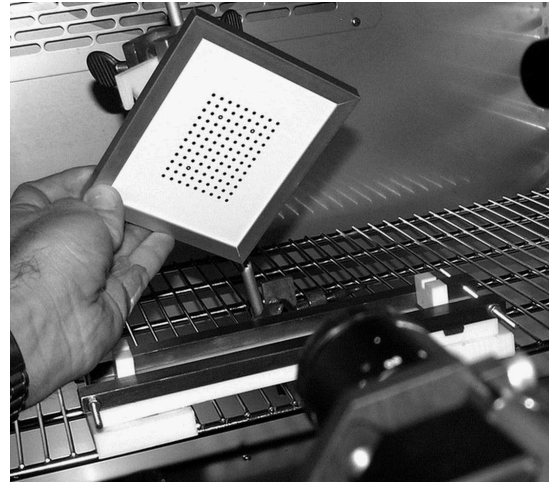

Figure 4.2: Calibration of the DIC-system. The computer detects the pattern in both images and then determines the camera parameters that are needed for the correlation.

has increased over the last years and is applied in various fields such as microelectronic packaging [75, 98, 116, 138], automotive, biomechanics [137] or geological engineering [25]. Various systems and software are commercially available. In this study we use a system by isi-sys with two 5 Mega pixel CCD cameras and the vic3D-software by Correlated Solutions. In 2009, we first demonstrated the benefits of this contactless measurement method for photovoltaic modules [39, 38]. In the mean time Meier [80] successfully managed to inspect the thermal displacement of complete solar cells in a PV module by viewing through the module glass.

Measurement principle

The principle is only presented in short form here, very detailed descriptions of the method are given in the books and articles of Sutton and Orteu [92, 117, 118]. Two CCD cameras mounted on a rigid rig take simultaneously pictures of the speckled surface of the inspected object. With the use of a pinhole model, that is illustrated in Fig. 4.1, both camera images P_A and P_B are correlated by a computer algorithm to obtain the shape of the surface S in three dimensions. Displacement and strain are measured by comparing the computed 3D-surface to the correlated surface of a reference state. In order to correlate the stereo images the correlation algorithm needs information about the orientation and position parameters of the cameras as well as the intrinsic parameters of each camera. These parameters are determined prior to each experiment by a calibration, which is performed by taking a number of images of a calibration target, that is held in different orientations in front of the cameras, as shown in Fig. 4.2. The exact point pattern on the target must, of course, be provided to the software.

4.1.2 Measurement errors

The examination of the measurement accuracy focuses on the use of the DIC-system as described in detail in Section 4.2. Figures 4.3 and 4.4 illustrate the experimental setup. Two regions on two adjacent solar cells near the gap between the cells are speckled and chosen as areas of interest (AOI) where the displacement is analyzed. The average displacement values of both AOIs are subtracted to determine the change of the gap width. Three possible sources of error contribute
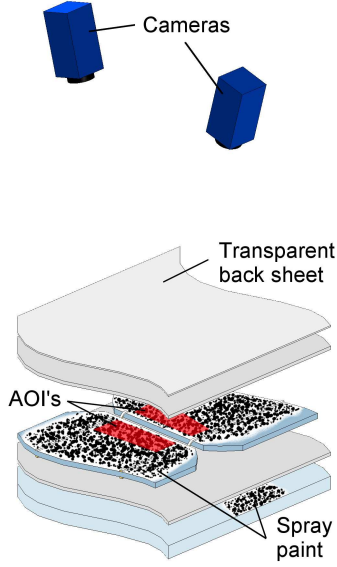
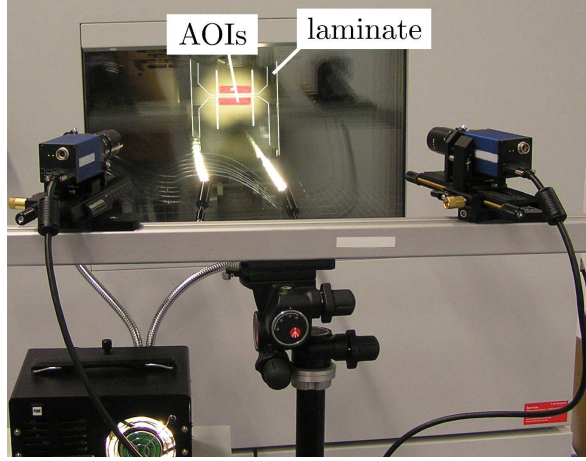Figure 4.3: Scheme of measurement and position of AOIs.

Figure 4.4: Experimental setup for measurement of gap displacement between two solar cells in the laminate.

to the global error of this measurement procedure. First, the strain and displacement resolution of the system, second the impact of the 10 cm thick window of the climate chamber that the cameras have to look through and third the influence of optical refraction of the transparent laminate layers on top of the inspected surface. These errors are estimated for one typical measurement setup with one corresponding calibration. The accuracy cannot by guaranteed for all measurements in this work as the system has been set up and removed several times, has thus been re-calibrated, has been used for various laminates and with different climate chambers. The discussion of the errors thus gives only an estimation of the accuracy that we believe not to deviate significantly for the different laminate experiments in Section 4.2.

Resolution of strain and displacement

The digital image correlation is a relative measurement method. In general, DIC-systems are calibrated with an accuracy of up to $e = 0.01$ pixels [117]. For the laminate measurements in Section 4.2 we calibrate the system through the window of the climate chamber thus reaching a calibration factor of $e = 0.05$ pixels. To determine the resolution in displacement Δu the mapping ratio in the focal plane array M, i.e. the number of micrometers per pixel, has to be taken into account,

$$\Delta u = e \cdot M.$$

We work with a mapping ratio of $M = 60 \,\mu\text{m/pixel}$, resulting in a displacement resolution of $3 \,\mu\text{m}$ as marked in Fig. 4.5.

Averaging over regions

For the determination of the gap change the resolution in displacement can be improved by averaging over measurement regions where the displacement values do not depend on their spatial coordinates. By taking into account approximately 1000 spatially resolved data points (number of pixels in one AOI shown in Fig. 4.3) to determine a single displacement value for one complete AOI the statistical error is lowered by the square root of 1000. For the gap measurement shown
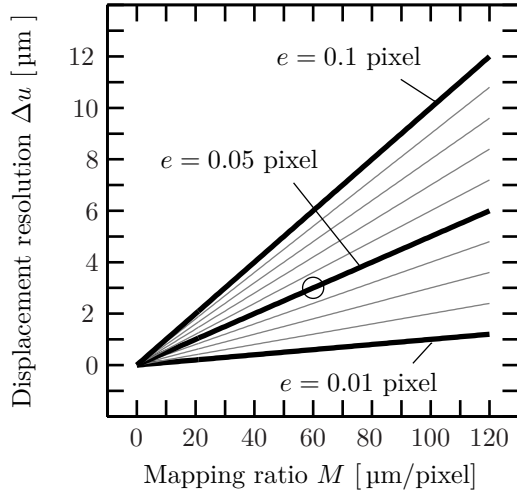
Figure 4.5: Resolution in displacement depending on the size of the inspected measurement area for the goodness of the calibration between $e = 0.01$ and $e = 0.1$.
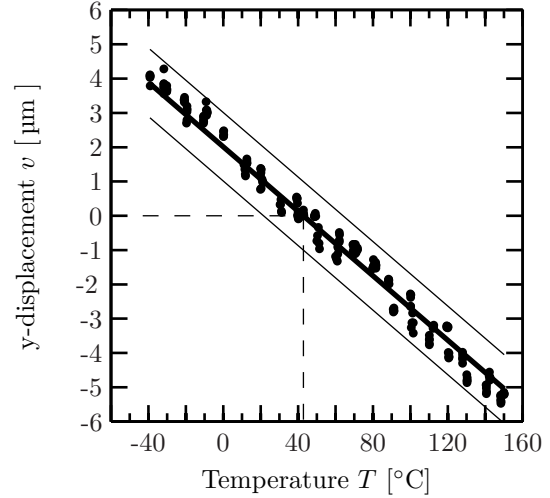
Figure 4.6: Measurement of AOI displacements on copper (points) and line calculated with CTE from literature [126]. Additional lines show reference state and 1 µm envelope.

in Fig. 4.7, this assumption of homogeneous displacement leads to an accuracy of $\Delta u = 0.1$ µm. However, the AOIs are stripes on the solar cells with a height h of approximately 8 mm and therefore the thermal deformation of the underlying silicon has to be taken into account. Then, the bottom of the stripe that is close to the gap moves away from the top of the stripe that is closer to the middle of the cell when the temperature rises. We calculate an upper limit of this difference Δh per °C by assuming a free thermal expansion of silicon, so that

$$\Delta h = h\,\alpha_{\mathrm{Si}}.$$

Then, the average values of one AOI in Fig. 4.7 contain a maximum error of 1.14 µm at -35.1°C and 1.33 µm at 89.7°C. Still, the technique of working with averaged data lowers the error in displacement to 1.3 µm for $\|T - T_{\mathrm{ref}}\| \leq 67$°C compared to the resolution accuracy of 3 µm for raw displacement data that we obtain from our calibration with $e = 0.05$ pixels.

Reference measurement with copper

We perform a reference experiment in order to verify the error that we calculated from the calibration and the averaging technique. We compare the measured free expansion of a copper sample with literature data for copper. A 3 cm x 10 cm copper strip with a thickness of 2 mm is placed in the climate chamber and is subjected to temperatures in the range of 150°C to -40°C. Pieces of polytetrafluoroethylene (PTFE), a material of low thermal conductance, hold the strip in an upward position similar to the laminate measurements. Still the strip remains unsupported and may thus freely expand. A temperature sensor is attached to the rear side of the sample. We record the displacement v in vertical direction every 10°C for every pixel. For each temperature 5 stereo-images are taken.

For an accurate comparison to the gap displacement measurements, we calculate the displacement values on the copper strip in the exact same manner, i.e. choosing the identical pixel coordinates for the lower AOI in Fig. 4.7. The y-displacement values in that AOI are averaged leading to one displacement value per stereo-image. These values are plotted in Fig. 4.6. The black line represents the displacement calculated from the CTE $\alpha = 16.4 \times 10^{-6}$ 1/K of copper which is taken from White [126]. The exact procedure of how to calculate the displacement from the CTE

is given in [39]. We find all measured data points in Fig. 4.6 to lie less than $1\,\mu m$ away from the literature data. We thus conclude from the reference measurement that the maximal error of the averaging technique for a thermal measurement through the window is less than $1\,\mu m$. However, the procedure of calculating the displacement from a given CTE in [39] does not assume the displacement to be constant over the AOI. Therefore, the maximum error for the experiments in Section 4.2 remains at the limits of $1.3\,\mu m$.

The discussion of the third source of error, which is due to the optical refraction at the two material layers on top of the solar cell that the cameras have to look through, is carried out in detail in [39]. There, the relative error in strain is found to be negligible as it is in the range of 1×10^{-6} for one camera.

To conclude the discussion of the accuracy, error contributions from the refraction of the transparent layers and the limits in displacement resolution are negligible for the presented laminate deformation experiment. The error determined with the copper reference measurement is less than $1\,\mu m$. The maximum error, however, originates from the violation of the assumption that the displacement is constant over one AOI at one temperature. We find this maximum error to be less than $1.4\,\mu m$ which we regard as the measurement accuracy for the laminate experiments.

4.2 Measurement of gap displacement

The displacement of the gap between two adjacent solar cells in a PV laminate is determined on test structures that contain 3 solar cells in a row.

4.2.1 Sample preparation

The application of the DIC method requires a random speckle pattern on the surface of the measured object (Fig. 4.3). As the deformation of the solar cells in the laminate is of interest, a speckle pattern is applied onto the rear side of the cells before lamination. Temperature resistant spray paint is used to cover the rear surface completely white. When dry a black pattern is sprayed on the white background. The thickness of the paint layer is measured between 20 and $40\,\mu m$. For the test laminate three speckled solar cells with a size of 125×125 mm^2 are placed between two transparent sheets of uncured ethylene vinyl acetate (EVA, etimex vistasolar 486.00) that are laid on top of a 4 mm thick glass plate. The distance between the cells is chosen to match 2 mm. The glass plate, and thus the laminate, is 45 cm by 15 cm in size. The rear side of the assembly is covered with a transparent back sheet (Isovolta Icosolar T 2754) which is a composite material with a thickness of $100\,\mu m$ consisting of polyethylene terephthalate (PET) and an ethylene tetrafluoroethylene (ETFE) core. The test sample is laminated after the paint has completely dried to avoid the formation of bubbles and the smearing of the paint. The lamination temperature is 150°C for 13 min. The EVA cures by crosslinking its molecular chains and adheres to the cells, the glass and the back sheet. After lamination the sample has a thickness between 5.0 and 5.2 mm. It is important to assure that the surface of the back sheet is completely flat and parallel to the speckled rear side of the cells after lamination. If the surface of the back sheet contains some sort of structure, for example in form of little lenses, the optical path from the speckled and buried surface to the camera would be disturbed. Then the assumptions made in the theoretical approach for the determination of the third source of error [39], i.e. the optical refraction at the laminate surface, are no longer valid.

4.2.2 Measurement

The laminate is placed in a climate chamber (CTS-40/350/S) in an upright position parallel to the window as it is shown in Fig. 4.4. The rear side of the sample faces the window so that the
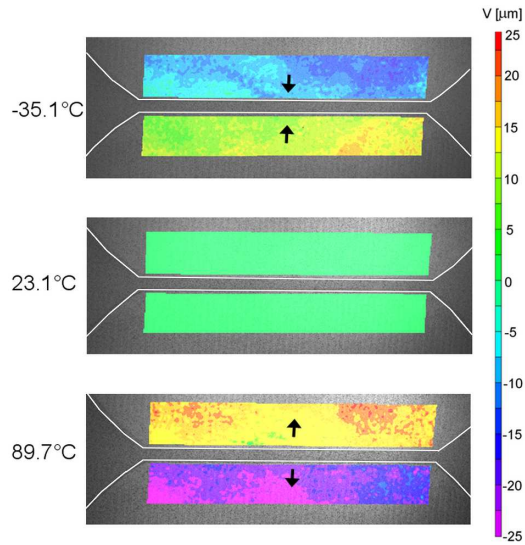
Figure 4.7: Inspected AOIs of the laminate with three non-interconnected solar cells. Colours indicate the displacement at three different temperatures. White lines highlight the edges of the solar cells.
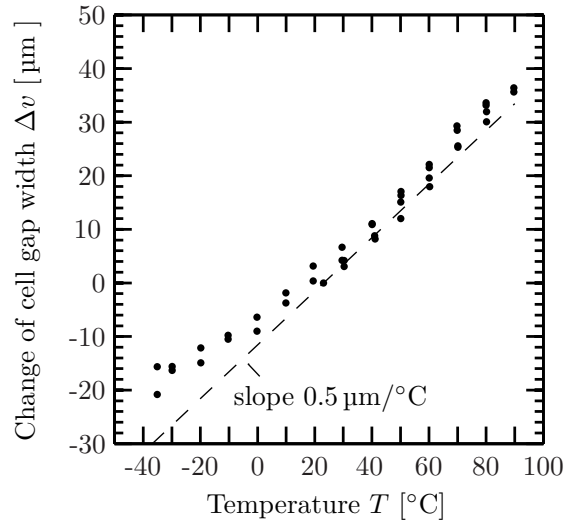
Figure 4.8: The change of the gap width between two laminated solar cells for different temperatures. The stress- and displacement-free reference state is at 23.1°C.

speckled surfaces are visible from outside the chamber. One thermocouple is attached to the front and another to the rear side of the PV laminate. The window consists of 4 glass panes and is approximately 10 cm thick. An LED source illuminates the measurement region on the speckled surface from outside the chamber. Both cameras are mounted on a rigid rig in front of the window with a stereo angle of approximately 30°. The system is calibrated by placing the calibration target inside the chamber, so that the cameras view the target through the window of the chamber eliminating the influence of the window.

One stereo image is recorded at room temperature before the experiment in order to define the reference state of the object. While monitoring the temperature sensors on the sample the laminate is heated up to 85°C. Afterwards the sample is cooled down to -40°C, imaging the surface approximately every 10°C.

4.2.3 Results

After the measurement an area of interest (AOI) is defined on the recorded images of the inspected surface, where the strain and the displacement are computed relatively to the reference state at 23.1°C. The AOIs are chosen directly adjacent to the gap between two solar cells. As the thermal deformation of the sample holder and of the interior of the climate chamber causes the AOI to move on the images of two different temperatures, the rigid body displacement and rotation has to be removed. This is done by an average transformation. Figure 4.7 shows these areas of interest and the color coded displacement values v in vertical direction for three different temperatures. Compared to room temperature, the regions near the cell gap move 20 µm up and down in vertical direction at 84.8°C. The opening and closing of the gap between two cells is computed from the displacement data of both AOIs by first averaging the vertical displacement over each AOI and second by then subtracting these average values. This difference is referred to as the change of solar cell gap width or simply gap displacement. The gap is found to widen when the temperature rises and to shrink when the temperature decreases. Figure 4.8 shows the change of the cell gap width as a function of the temperature. The graph has a linear behaviour for temperatures above
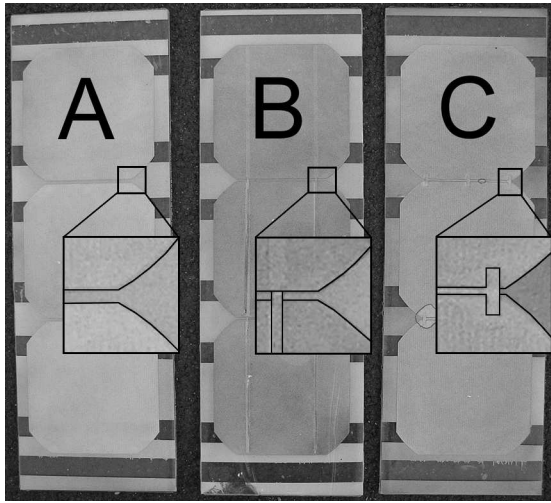
Figure 4.9: Test laminates: no interconnection(A), standard interconnection (B) and back-contact interconnection (C).
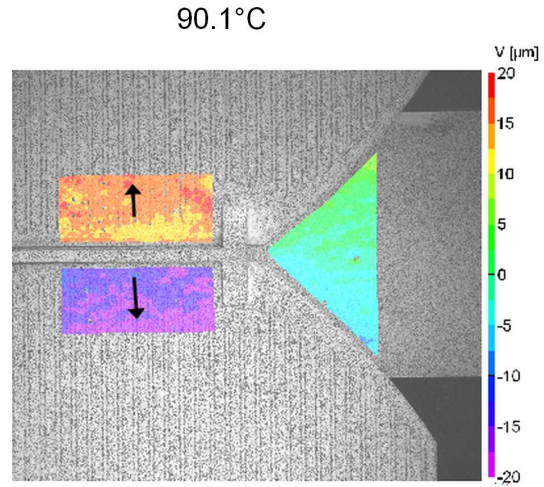

Figure 4.10: Laminate C: experimental determination of gap displacement of 30.14 µm at 90.1°C.

0°C and a less steep slope below 0°C. A change of cell gap is found to be around 0.5 µm/°C as plotted in Fig. 4.8.

4.2.4 Varying materials and interconnection techniques

The experiment described above is repeated with a number of modified laminates. Two characteristics are changed compared to the laminate from Subsections 4.2.1 - 4.2.3 which is now named 'laminate A'. First, different interconnection techniques are investigated and second borosilicate glass is used instead of the soda-lime glass substrate.

Different interconnection techniques

Figure 4.9 shows three similar laminates that differ only in their interconnection method. The cells in laminate A are not connected while laminate B contains standard interconnected cells. There, the copper ribbons reach from the cell's top surface to the bottom face of the neighboring cell. In between the cells the interconnect resembles a stretched S-shape seen from a side-view. In laminate C a plane back-contact interconnector is soldered to 6 points on the rear sides of back-contact cells. It creates a direct link between the solder joint pairs along the cell gap. For the latter two laminates the soldering is done prior to the application of the spray paint. Apart from that the preparation steps are identical to those of laminate A as described in Subsection 4.2.1. The plot in Fig. 4.11 displays the temperature for laminate A during the experiments. The temperature is read from the thermocouples which are attached to the front and back of the laminates. We chose the average of both values to define the actual sample temperature. Figure 4.12 shows the measured changes of the cell gap width over temperature. The data for laminate B and C are displayed along with the data for A from Fig. 4.8. A detail of the experiment with laminate C at 90.1°C is given in Fig. 4.10. The slope of the data points of laminate B (standard interconnection) is slightly higher than laminate A while laminate C exhibits a smaller slope. We believe the latter observation to be due to the presence of the back-contact interconnector shown in Figs. 4.9 (C) and 2.7 (second from bottom) which creates a stiff mechanical connection between the cells and thus constrains the gap displacement.
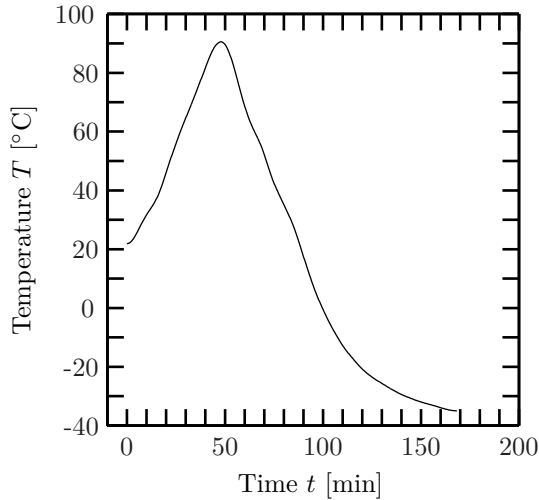
Figure 4.11: The temperature curve during laminate A experiment. The average of both temperature sensors is shown.
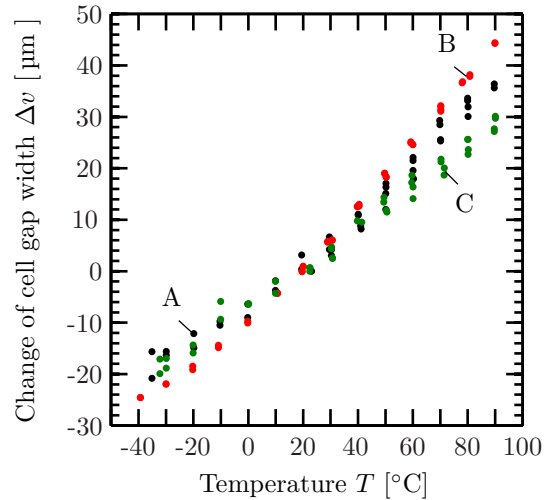
Figure 4.12: Measured changes in the cell gap width for laminates A(black), B(red) and C(green).

Borosilicate glass

An additional laminate is prepared where the soda-lime glass is replaced by borosilicate glass. The cells are not interconnected in order to compare the measurement to the laminate A data from the soda-lime glass experiments. The dimensions of the borosilicate glass are equal to those of the soda-lime glass. Thereby, the geometric properties of the laminates are identical but the CTE of the glass, that is believed to have a strong impact on the gap displacement, is now significantly lower. As described in Section 2.3.1 the CTE of borosilicate glass $(3.25 \times 10^{-6}$ 1/K$)$ is between one half and one third the value of soda-lime glass $(7.8 - 9.4 \times 10^{-6}$ 1/K$)$ and hence much closer to the CTE of silicon (approx. 2.5×10^{-6} 1/K). Consequently, less change of the cell gap is expected. The temperature curve during the experiment with the borosilicate laminate, that is plotted in Fig. 4.13, is different to the one of the soda-lime glass laminate (Fig. 4.11) because here the laminate is given approximately one hour to reach a homogeneous and stable temperature before an image is recorded. The image capturing is symbolized by the points in Fig. 4.13.
Similar to the soda-lime glass experiments described above, the change of cell gap width is determined and added to the measured values of the non-interconnected soda-lime glass laminate in Fig. 4.14. No significant change of the cell gap is detected as the data are in the range of the measurement accuracy of 1.4 μm which is discussed in Section 4.1.2. It implies that the adaption of the CTE of glass close to silicon eliminates the temperature related gap displacement.

4.3 Simulation of gap displacement in 2D

Thermomechanical simulations are able to provide the full range of mechanical quantities for every material point such as displacements, stresses and strains if the real material properties and the correct loading conditions are properly reproduced by the computational model. Experiments can only deliver information from a few material points, for example strain from strain gages or displacements from digital image correlation. It is thus the combination of experiments and simulations that permits a thorough study of a device's deformation. In this section the experimental results from the gap measurements are taken as references to check how well the computational models forecast the mechanical behaviour of PV laminates. Therefore, a two dimensional geometry with dimensions equal to the test laminates in Section 4.2 is composed and shown in Fig. 4.15.
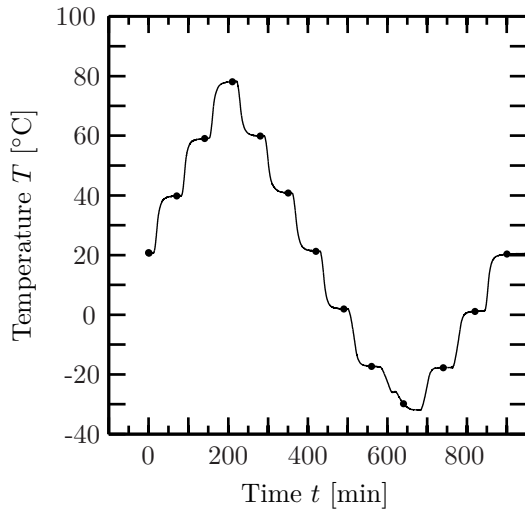
Figure 4.13: Temperature over time for the experiments with borosilicate laminates. Marks indicate the times when the deformation is recorded.
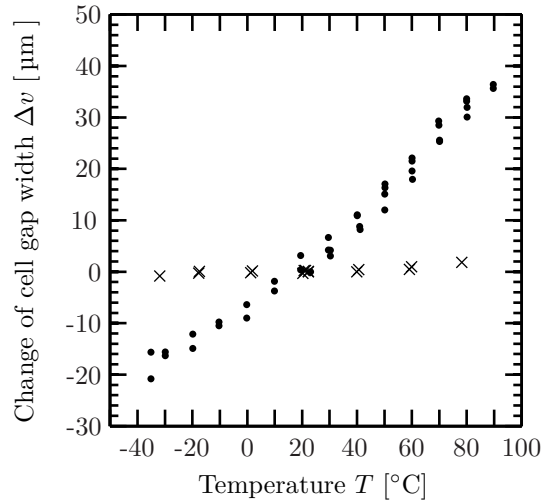
Figure 4.14: Measured changes in the cell gap width for non interconnected cells. Comparison between float glass experiment($\cdot$) from Fig. 4.8 and borosilicate experiment($\times$).

Although the geometry demands a plane strain simulation, plane stress is favored over plane strain. The reason is that in the plane strain mode the thermal strain in the out-of-plane direction can only remain zero, if very high out-of-plane stresses occur which implies a non-physical state in this context. The out-of-plane thickness is set to 125 mm to match the cell width. We choose quadratic shape functions on a triangular mesh. The element type is shown in Fig. 2.4 b). The symmetry of the test samples allows to model only one half of the laminate by applying symmetric boundary conditions to the left boundary displayed in Fig. 4.15. The lower left hand point is fixed in order to avoid rigid body displacements. The simulation is conducted with both isotropic and anisotropic silicon values as well as purely linear elastic, temperature-dependent elastic and viscoelastic material models for EVA. The other constant material parameters are varied by $\pm 10\%$ in order to evaluate the sensitivity of the values, that were introduced in Section 2.3, to the computational results.

The purely linear elastic and temperature-dependent linear elastic models are simulated with Comsol Multiphysics. For the viscoelastic material model the software Abaqus is used.

4.3.1 Use of linear elastic models

Linear elasticity (for isotropic materials) requires a pair of constant values, for example the Young's modulus E and Poisson's ratio ν. It is not dependent on time, so that only the temperature range from the experiments needs to be fed to the simulation instead of the complete temperature history from Fig. 4.11. Consequently, a parametric model with temperature T as a parameter is sufficient to simulate the gap-experiments. The reference temperature, where no initial stress or strain is present, is set to the lamination temperature of $150°$C. The values for parameter T range from $150°$C in steps of $10°$C down to $-40°$C. As it is demonstrated in Subsection 2.3.5 and in Chapter 3 it is impossible to pick the 'correct' value for the Young's modulus of EVA as is not a constant value but dependent on time and temperature. In this simulation context with a linear elastic model, where only constant material values can be taken into account, the value of E for EVA is set to the highest and lowest value from Fig. 2.23. We thus expect to obtain from this simulation a higher and lower bound for the gap displacement. The parameters used in the linear elastic simulations are given in Tables 4.1 and 4.2. The values for the EVA and the back sheet
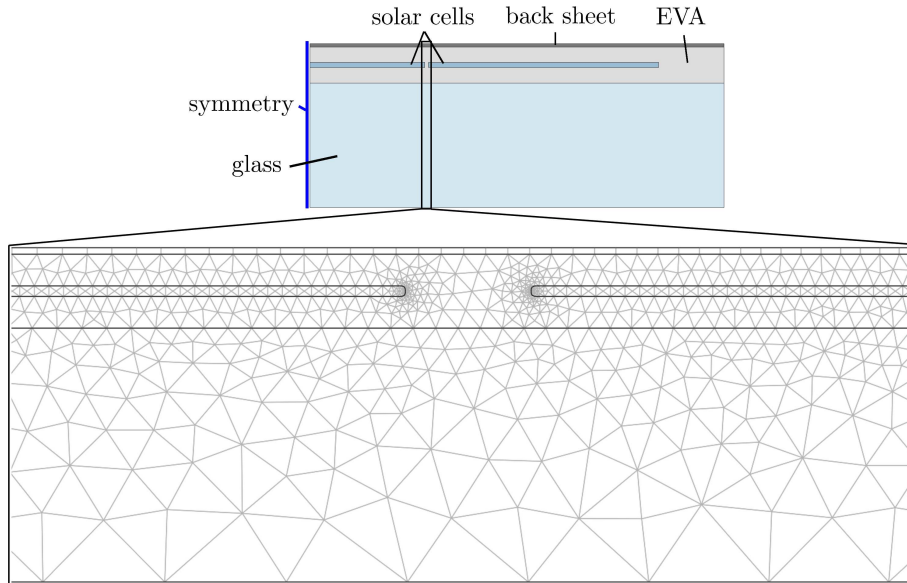
Figure 4.15: Geometry of the 2-dimensional FEM-model in the simulations with Comsol Multiphysics.

are varied by $\pm 10\%$ while for silicon and glass the data from literature are believed to be correct. For silicon, E is set to the in-plane value of anisotropic silicon $E_{<100>}$. For glass only the value of α is varied because the testing that is documented in Section 2.3.1 reveals a slight discrepancy to the literature data.

Laminates with float glass

The simulated gap displacement, where all materials are modeled with constant linear elastic parameters, is shown in Fig. 4.16. The values are obtained from inspecting the difference in the x-displacements at the two points on the cell edges. In the unstressed initial state at $150°$C the width of the cell gap is 2 mm. When the temperature decreases the simulation shows a shrinkage of the cell gap which is found in the experiments as well. Furthermore, three main observations can be made from the simulation results:

First, the two different values for E of EVA have a large impact on the gap displacement as they give two different black lines shown in Fig. 4.16. The simulations with a stiff EVA (high value for E) exhibit a lower gap displacement than those with a compliant EVA (low value for E). A stiffer EVA implies a stronger adhesion of the solar cells to the glass so that the thermal displacement of the glass forces the silicon to deform accordingly. A compliant EVA describes a weaker bond between the glass and the solar cells so that the silicon is able to deform more independently following its pure thermal contraction. In this case, the silicon contracts less than the glass below the cell and thus the gap displacement is larger.

Second, varying the coefficient of thermal expansion of the glass α by $\pm 10\%$ results in significant deviations from the gap displacement curves indicated by gray lines in Fig. 4.16. A higher α implies a larger difference of the CTEs of glass and silicon and thus a larger gap displacement. When the CTE approaches the CTE of silicon the gap displacement is expected to be lower. It has to be pointed out that the two values for EVA are motivated by the experimental observations from Subsection 2.3.5 and differ by 2 to 3 orders of magnitude instead of only $\pm 10\%$.

Third, the variation in all other parameters has no influence on the gap displacement results as the black curves from simulations 1 - 7 coincide in the plot as well as the curves from simulations
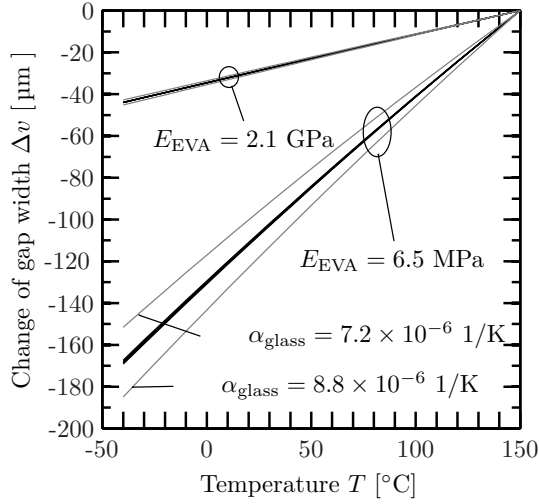
Figure 4.16: Simulated changes in the cell gap width for non-interconnected float glass laminates. The linear elastic parameters are given in Tables 4.1 and 4.2.
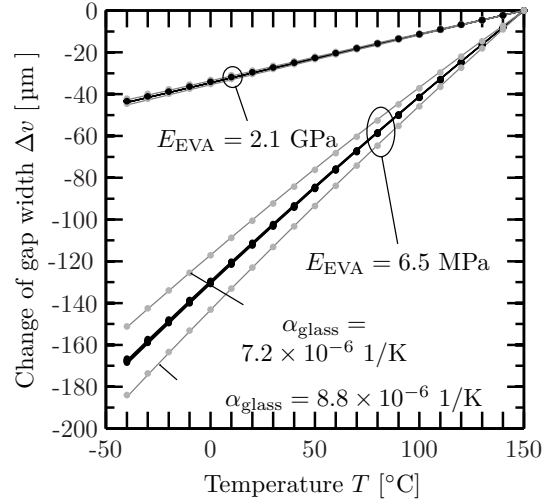
Figure 4.17: Simulated changes in the cell gap width for anisotropic silicon (points) compared to isotropic silicon (lines) from Fig. 4.16 for simulations 1-18.

10 - 16 (Tables 4.1 and 4.2).

Including the full anisotropy of silicon in the simulation model does not change the simulated gap displacement result. This can be seen from Fig. 4.17 where the anisotropic data (points) coincide with the isotropic data (lines). The anisotropic model for silicon is thus not further considered in the subsequent two-dimensional simulations of the gap displacement.

In order to compare the simulation data directly with the experimental data, the simulation curves have to be shifted. In the experiments the reference temperature is set to room temperature while the simulation assumes its stress free initial state at lamination temperature. However, as the experimental samples are laminated at 150°C and cool down to the experimental reference temperature the laminate is at the beginning of the experiment already in a deformed state. The simulation curves must therefore be shifted along the *y*-axis until the gap displacement at room temperature is equal to zero. As plotted in Fig. 4.18 the simulation curves then create a corridor with an upper and lower bound which results from the minimum and maximum values for the Young's modulus of EVA. The experimental data are found to fit well in that corridor. However, it is noticable that the simulated gap displacement does not agree with the experimental data nor is it able to reproduce the laminates' curve-shaped deformation behaviour as it always forms virtually straight lines over temperature.

Laminates with borosilicate glass

Simulations of the borosilicate laminate are carried out in the same manner as for the float glass laminates. The CTE of glass is changed to 3.25×10^{-6} 1/K, which is taken from literature for borosilicate glass according to Subsection 2.3.1, and is also varied by $\pm 10\%$. The corresponding modifications in the list of parameters is given in Table 4.3. The simulation results are plotted in Fig. 4.19. The change of the cell gap is less which supports the thesis that the gap displacement diminishes as the CTEs of glass and silicon converge.
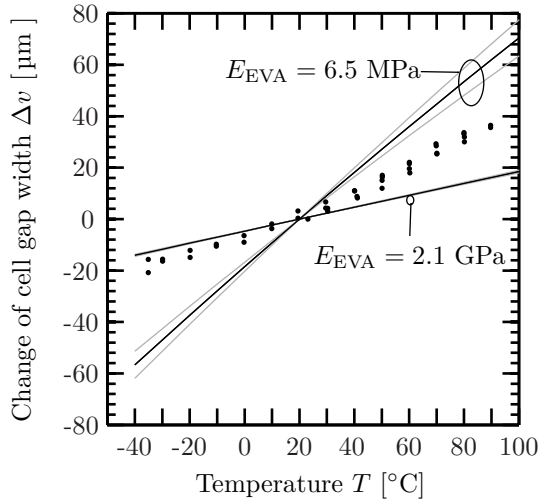
Figure 4.18: Comparison of linear elastic simulations and experiment for non-interconnected float glass laminate (laminate A in Fig. 4.12).
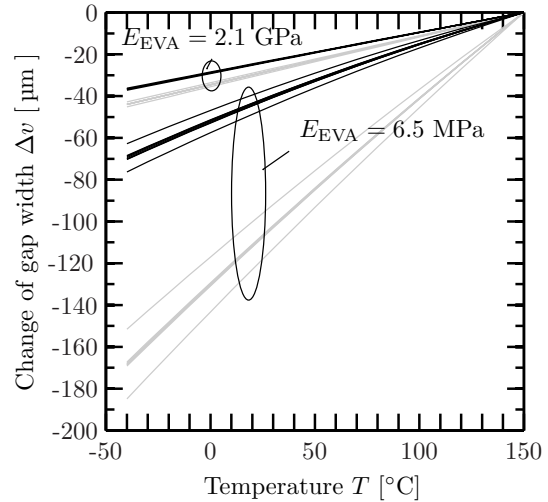

Figure 4.19: Simulated changes in the cell gap width for non-interconnected borosilicate glass (black) compared to float glass (gray).
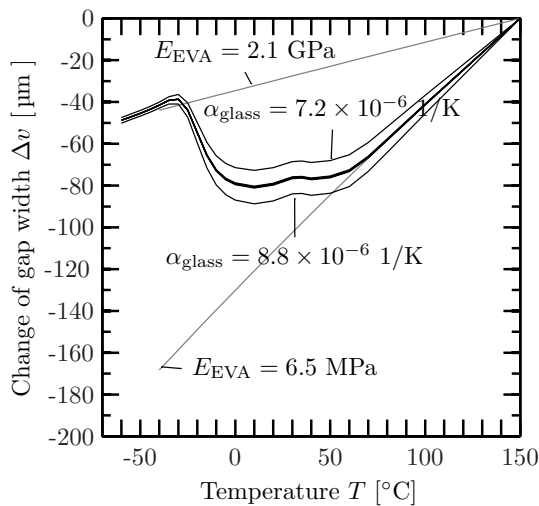

Figure 4.20: Simulated changes in the cell gap width for non-interconnected float glass laminates. The Young's modulus of EVA is a function of temperature $E(T)$ as plotted in Fig. 2.23. Gray lines are the linear elastic simulations for float glass from Fig. 4.16.
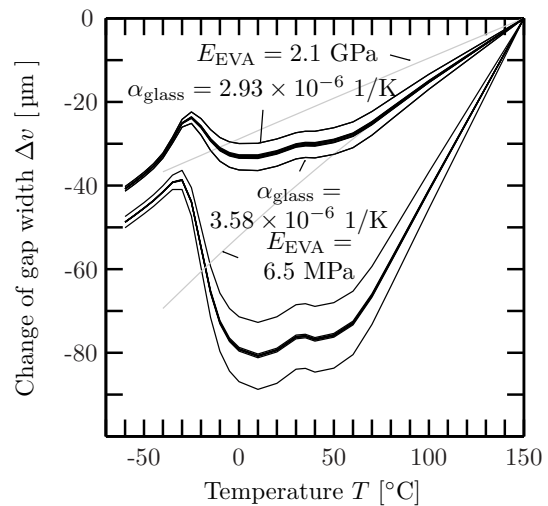
Figure 4.21: Simulated changes in the cell gap width for borosilicate glass laminate A with T-dependent E of EVA. The lower black lines correspond to the float glass results from Fig. 4.20. Gray lines are linear elastic simulations for borosilicate glass from Fig. 4.19.

Table 4.1: Mechanical material parameters for linear elastic simulations.

Sim.-	Glass	EVA	Back sheet		
No.	α	E	E	ν	α
	$[10^{-6}\frac{1}{K}]$	[MPa]	[GPa]	[-]	$[10^{-6}\frac{1}{K}]$
1	8	2100	2.80	0.4	50.4
2	8	2100	2.52	0.4	50.4
3	8	2100	3.08	0.4	50.4
4	8	2100	2.80	0.4	45.4
5	8	2100	2.80	0.4	55.4
6	8	2100	2.80	0.36	50.4
7	8	2100	2.80	0.44	50.4
8	7.2	2100	2.80	0.4	50.4
9	8.8	2100	2.80	0.4	50.4
10	8	6.5	2.80	0.4	50.4
11	8	6.5	2.52	0.4	50.4
12	8	6.5	3.08	0.4	50.4
13	8	6.5	2.80	0.4	45.4
14	8	6.5	2.80	0.4	55.4
15	8	6.5	2.80	0.36	50.4
16	8	6.5	2.80	0.44	50.4
17	7.2	6.5	2.80	0.4	50.4
18	8.8	6.5	2.80	0.4	50.4

Table 4.2: Mechanical material parameters for linear elastic simulations which are kept constant.

Sim.-	Glass		Silicon			EVA	
No.	E	ν	E	ν	α	ν	α
	[GPa]	[-]	[GPa]	[-]	$[10^{-6}\frac{1}{K}]$	[-]	$[10^{-6}\frac{1}{K}]$
1-18	73	0.23	130	0.28	2.49	0.4	270

Table 4.3: Modified parameters in Tables 4.1 and 4.2 for the borosilicate simulations.

Sim.-	Glass
No.	α $[10^{-6}\frac{1}{K}]$
1-7, 10-16	3.25
8, 17	2.93
9, 18	3.58
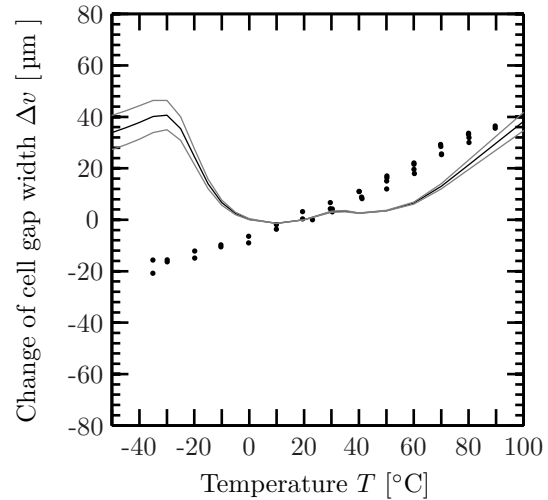
Figure 4.22: Comparison of laminate A float glass measurement and T-dependent linear elastic simulation.

4.3.2 Use of temperature-dependent linear elastic models

From the experimental determination of the mechanical properties of EVA in Subsection 2.3.5 a strong dependence of the Young's modulus E on temperature is found (Fig. 2.23), i.e. between 2.1 GPa and 6.5 MPa. So far, this information has only been used to motivate an upper and lower limit for the Young's modulus E of EVA in the purely linear elastic simulations above. Here, the T-dependent mechanical stiffness is modeled over the temperature range as $E(T)$, that is given in Fig. 2.23. The variations of the elastic material parameters are the same as for the linear elastic simulations and are given as simulation numbers 1-9 in Tables 4.1 and 4.2 neglecting column 'EVA E'.

The results of the gap displacement simulations are plotted in Fig. 4.20. The change of the gap width is now not monotonic so that a reduction of the cell distance is found for temperatures under 0°C from the T-dependent linear elastic simulation. In fact, the curve contains similar characteristics compared to the $E(T)$-curve for EVA shown in Fig. 2.23: the bump at 30°C and the strong increase between 0°C and -30°C. Again, only the variation of the CTE of glass has an impact on the simulation results as shown in Fig. 4.20. The linear elastic simulation results are plotted to allow a direct comparison to the previous simulation and seem to take the role of limits for the T-dependent curve.

The results for the borosilicate glass in Fig. 4.21 show that the shape of the T-dependent simulation curve is the compressed version of the float glass simulation. Similar to the linear elastic simulations, the gap displacement for borosilicate glass is significantly less than for float glass and its shape is bounded between the two linear elastic simulations for borosilicate glass (gray lines in Fig. 4.21).

Shifting the simulation curve to zero displacement at 20°C (Fig. 4.22) reveals that the step from pure linear elasticity to T-dependent elasticity for EVA does not improve the replication of the experimental data. Neither the actual values nor the shape of the curve agree well with the experimental values. The T-dependent simulation does thus not help to better understand the thermomechanical characteristics of the laminate although the mechanical characteristics of the bulk material EVA are more adequately taken into account compared to pure linear elastic models.

4.3.3 Use of viscoelastic models

In Chapter 3 a viscoelastic model has been constructed for EVA. This model includes a time and temperature dependency. When simulating the experiments from Section 4.2 the whole temper-
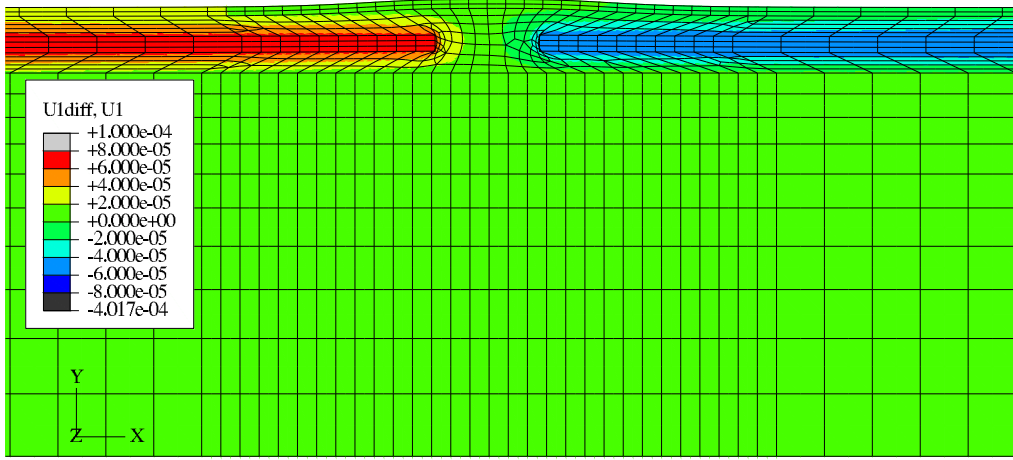
Figure 4.23: Detail of the FEM-model for the viscoelastic gap simulation with Abaqus. The plotted variable u_{diff} is the x-displacement subtracted by the x-displacement value in the gap center. The deformation is scaled.

ature history of the laminate has to be considered, starting from the stress-free initial state of 150°C. Therefore, the temperature history that is fed as input data to the viscoelastic simulation consists of a cooling stage accounting for the time directly after lamination, a time of storage accounting for the time between lamination and experiment and the actual temperature curve during the experiment as plotted in Fig. 4.24. The cooling stage is shown in detail in Fig. 4.25. The data are measured by a thermocouple from a similar sample where the temperature evolution during and after lamination was monitored until the sample temperature reached approximately 20°C again. The time of storage is set to 24 h because the experiment was performed the day after the lamination. The data used for the actual experiment are identical to the temperatures shown in Fig. 4.11 but shifted in time to fit after the 'store'-stage. The viscoelastic simulation is performed with Abaqus. Figure 4.23 shows the region around the cell gap. The displacement is shown in a scaled view.

Selection of the generalized Maxwell model

The viscoelastic model for EVA from Chapter 3 is given in form of a generalized Maxwell model that describes the shear relaxation modulus G_{rel} as a function of the reduced time t_{red}. The reduced time t_{red} is the quantity that contains the information of temperature and relaxation time according to the time-temperature-superposition explained in Section 3.5. The generalized Maxwell model from Chapter 3 covers the complete range of the mastercurve that was constructed from all performed relaxation and creep measurements, beginning with reduced times at $\tau_1 = 10^{-4}$ s and ending at $\tau_{25} = 10^{20}$ s. The question arises whether it is necessary to feed the complete model with 25 Maxwell arms to the simulation or whether a subset of the model is sufficient to simulate the gap displacement. This question can be answered prior to the simulation by inspecting the range of the reduced time that will be crossed during the simulation. The input data of the temperature history shown in Fig. 4.24 determine the range of the reduced time. In the T-dependent viscoelastic constitutive equation

$$\sigma(t, T) = \int_0^t E(t - s, T_{\text{ref}}) \, \dot{\varepsilon}(s) ds = \int_0^t E(\xi(t) - \xi(s)) \, \dot{\varepsilon}(s) ds$$
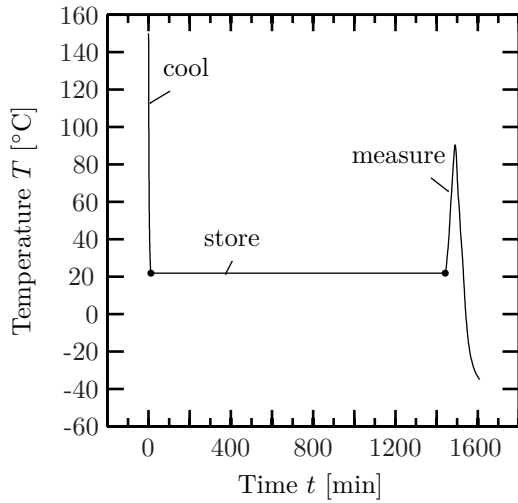
65

Figure 4.24: Full temperature history of measured laminate A. 'Cool' is the cooling stage after lamination, 'store' the time of 24 h between lamination and experiment and 'measure' are the time-temperature data from Fig. 4.11.
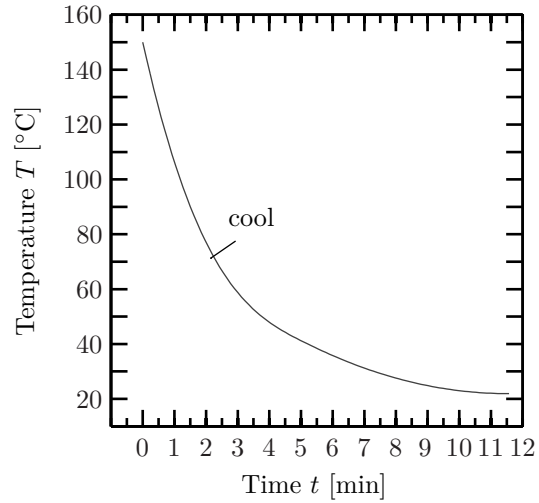

Figure 4.25: Time-temperature curve of the cooling stage from Fig. 4.24 in more detail. The data are read from a thermocouple which has monitored the sample temperature during and after lamination.
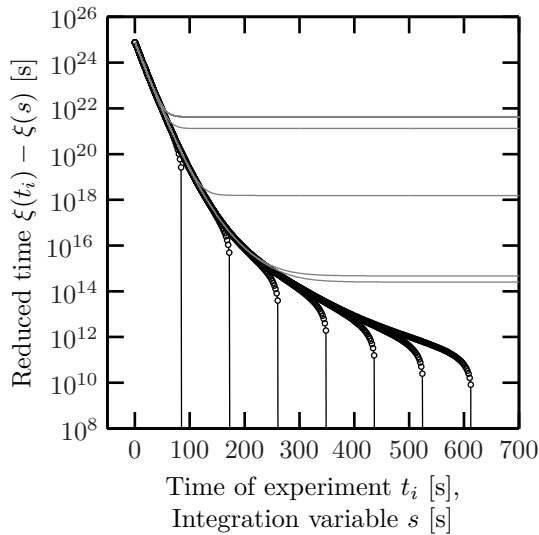

Figure 4.26: Reduced times calculated from time-temperature curve of the cooling stage shown in Fig. 4.25. The gray curves range from $s = 0$ to times t_i in the measurement stage outside of this graph.
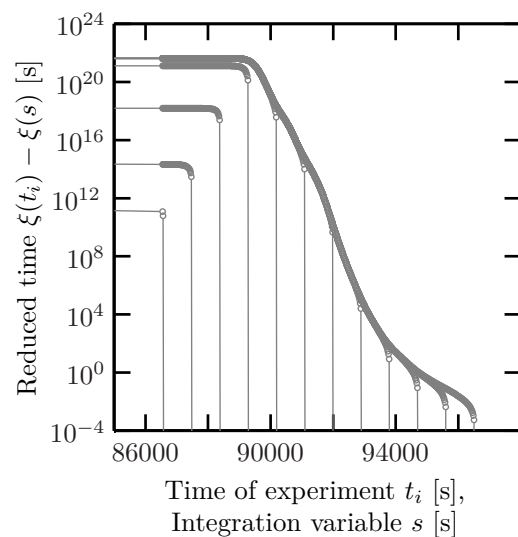
Figure 4.27: Reduced times calculated from time-temperature curve of the measurement stage shown in Fig. 4.24. As $s \in [0, t_i]$ for each t_i, the gray curves begin at 0 as shown in Fig. 4.26.

Table 4.4: Viscoelastic material model for EVA with 26 Maxwell arms.

	Maxwell parameters	
	τ_i	G_i
	[s]	[MPa]
0		0.24
1	10^{-3}	90
2	10^{-2}	40
3	10^{-1}	19
4	10^{0}	11
5	10^{1}	7
6	10^{2}	4
7	10^{3}	2.5
8	10^{4}	1.4
9	10^{5}	1
10	10^{6}	0.8
11	10^{7}	0.6
12	10^{8}	0.7
13	10^{9}	0.8
14	10^{10}	0.8
15	10^{11}	0.7
16	10^{12}	0.6
17	10^{13}	0.56
18	10^{14}	0.48
19	10^{15}	0.5
20	10^{16}	0.3
21	10^{17}	0.25
22	10^{18}	0.12
23	10^{19}	0.07
24	10^{20}	0.03
25	10^{21}	0.02
26	10^{22}	0.02

the argument for the relaxation modulus is

$$\xi(t) - \xi(s) = \int_0^t \frac{1}{\alpha_{T_{\text{ref}}}(T(u))} \, du - \int_0^s \frac{1}{\alpha_{T_{\text{ref}}}(T(u))} \, du$$

and can be computed as a function of $s \in [0, t]$ for every t in Fig. 4.24. In order to visualize this function, a number of experimental times $t_i \leq t$ is chosen and a family of functions $\xi(t_i) - \xi(s)$ is plotted in Figs. 4.26 and 4.27. As s runs from 0 to t_i, each curve ends at $s = t_i$, leading to $\xi(t_i) - \xi(s = t_i) = 0$. The times t_i can thus be read from the graphs as the intersections of the x-axis. The left graph shows the calculated reduced times of the cooling stage and the right graph the reduced times of the measurement.

It is found that the reduced time for the complete temperature history ranges from 10^{-3} to 10^{25}. For this gap displacement simulation the generalized Maxwell model can thus not be significantly reduced. The model used here consists of 26 Maxwell arms, setting the values for τ to one per decade between 10^{-3} and 10^{22}, and is shown in Fig. 4.28. The parameters of the generalized Maxwell model are given in Table 4.4.

The viscoelastic simulation of the gap displacement is shown in Fig. 4.29. The results from previous simulations, using linear elasticity and T-dependent linear elasticity, are plotted in gray. The viscoelastic curve is monotonically decreasing when moving from hot to cold temperatures. During the 24 h of storage at 20°C the gap width remains almost constant so no major creep
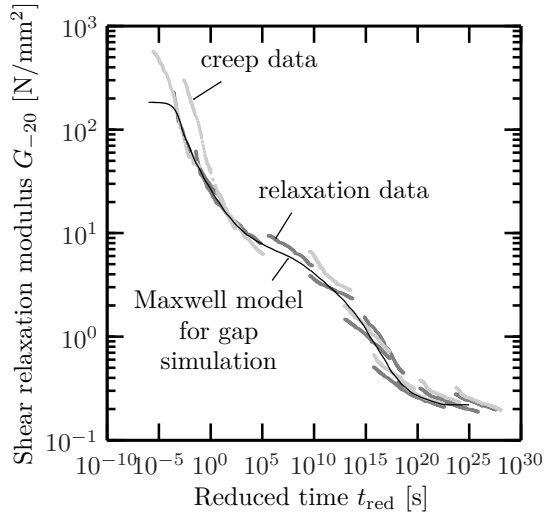
Figure 4.28: Generalized Maxwell model with 26 arms used for viscoelastic gap simulation. The shear relaxation data at reduced times less than 10^{-3} are not modeled.
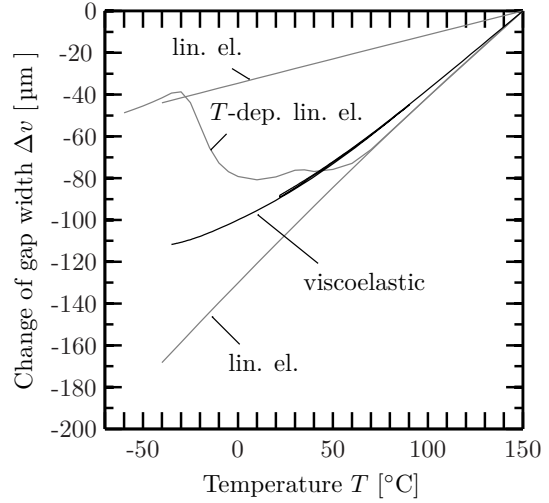

Figure 4.29: Viscoelastic gap simulation in comparison to linear elastic and T-dependent linear elastic simulations from Figs. 4.16 and 4.20.
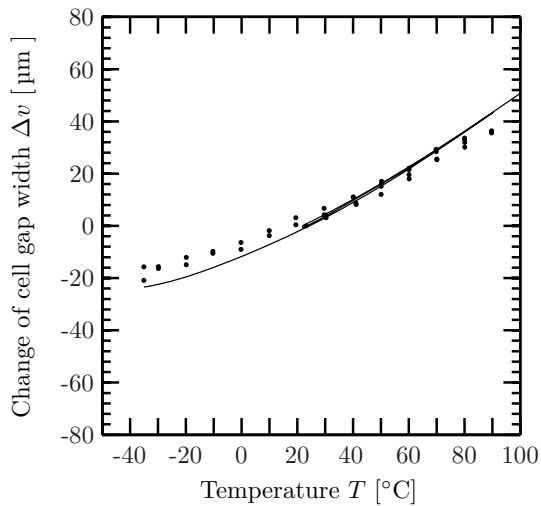

Figure 4.30: Comparison of laminate A float glass measurement and viscoelastic simulation.
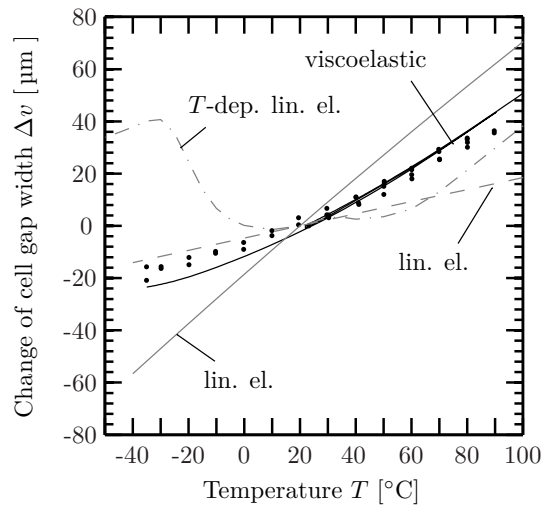

Figure 4.31: Comparison of all three simulation models to experimental gap displacement data.

processes are found. When the laminate is then heated to 90°C and cooled down to -35°C in the simulation, the slope of the curve diminishes at cold temperatures.

When comparing the simulation to the experiment in Fig. 4.30 it is found that the viscoelastic simulation data agree quite well with the measured data. Again, the simulation results were shifted along the y-axis until the gap equals zero at room temperature in order to allow a direct comparison. At temperatures above 20°C the simulation curve reproduces the measurement data particularly well while at cold temperatures the simulated and experimental data exhibit a very similar shape of a decreasing slope. However, the global slope of the simulation curve is slightly higher than the one of the measurement data. Compared to the other simulation results in Figs. 4.18 and 4.22 the viscoelastic model gives by far the most consistent results with the experiment, see Fig. 4.31.

4.4 Simulation of a PV module in 3D

In Chapters 2 and 3 the mechanical material properties of the module materials are determined. In the previous section we find the viscoelastic material model for EVA to give the best agreement with experimental data. We now use the results of these preliminary steps to approach the central part of this work which is to characterize the thermomechanics of a PV module. In the 3-dimensional simulation model we subject an unframed module to one temperature cycle of the IEC 61215 test and inspect the stresses and strains in the different module materials. The initial stress free state is again set to lamination temperature so that prior to the temperature cycle the module cools down to room temperature and is then held at 21°C for 24 h. The solar cells in the module are not interconnected. The three-dimensional FEM-simulation is carried out with the software package Abaqus.

4.4.1 Geometry, boundary conditions and material properties

The module contains 60 solar cells grouped in 6 lines made of 10 cells. The cell size is 125 mm × 125 mm pseudo-square. The gap between two cells is 2 mm and the outer cells have a distance of 20 mm to the module edges. We use a 4 mm thick float glass and choose the 350 μm thick Isovolta Icosolar 2442 for the back sheet. We regard it as a widely used standard material whose mechanical stiffness is measured in Subsection 2.3.4. We do not measure the module with the DIC sytem so that we are no longer restricted to use a transparent back sheet. The symmetry of the module is exploited by modeling only the lower left hand quarter of the complete module and by applying symmetric boundary conditions to the top and right hand faces as shown in Fig. 4.33. The outer surface of the glass is constrained to zero out-of-plane-displacement, thereby preventing possible bending of the module. The material layers have constant initial thicknesses over the module length and width. In the layer of the solar cells the space between the cells is filled with EVA. The thickness of each layer at 150°C is given in Table 4.5.

Table 4.5: Material properties used for the 3D-simulation of a PV module

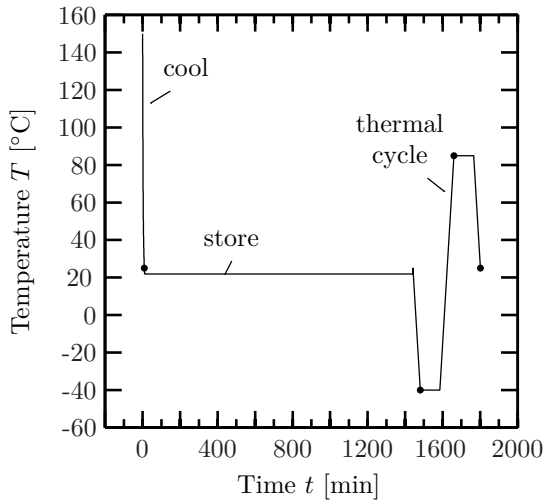|	Thickness d [μm]	Density ρ [g/cm^3]	El. modulus E [GPa]	Poisson's ratio ν [-]	CTE α [$10^{-6}\frac{1}{K}$]
Float glass	4000	2.5	73	0.23	8
Back sheet	350	2.52	3.5	0.29	50.4
EVA	500	0.96	viscoelastic model (Table 4.4)		270
Solar cells	200	2.329	anisotr. stiffness matrix (Eq. (2.20))		T-dep. (Table 2.6)

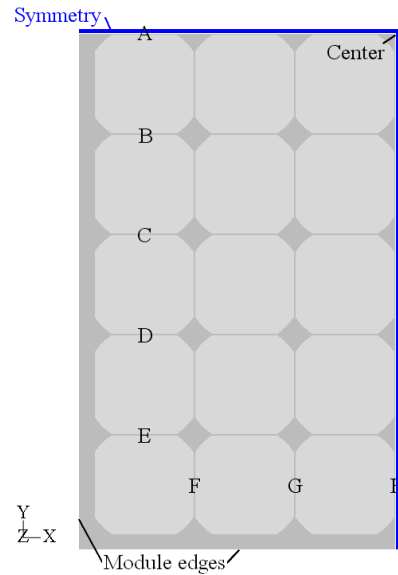Figure 4.32: Temperature profile for the module simulation

Figure 4.33: Simulation model of a 60 cell module with symmetric boundary conditions. Letters indicate the gaps between cells.

As in the viscoelastic gap simulation, the properties of the float glass and the back sheet are set to isotropic linear elastic and are listed in Table 4.5. For EVA, the viscoelastic model from Table 4.4 with WLF parameters from Table 3.1 is chosen. In order to model standard oriented monocrystalline solar cells (cf. Section 2.3.3) we use the stiffness matrix C from eq. (2.20) with constant values for C_{11}, C_{12} and C_{44} from Table 2.6. Here the coefficient of thermal expansion of silicon is made temperature-dependent with the values given in Table 2.6.

The PV module is exposed to a homogeneous temperature profile that consists of a cooling stage from lamination temperature of 150°C down to 21°C, a 24 h storing time at room temperature and a subsequent temperature cycle according to IEC 61215. The cooling profile is identical to the one used for the viscoelastic gap simulation in Fig. 4.25. The complete profile is plotted in Fig. 4.32. The module is stress free at the inital temperature of 150°C.

4.4.2 Simulated stresses and strains

Numerical results

When the module cools down from the initial stress free state at 150°C the material assembly contracts. At -40°C we find the stresses in the mid-plane of the glass to be compressive with the third principal stress σ_{III} between -4.2 MPa and -0.003 MPa. In contrast, the back sheet on the other outer face is in high tension. Over large regions the first principal stress σ_I reaches values of up to 41.7 MPa (Fig. 4.35). The embedded solar cells are under high compressive stress which is visualized in Fig. 4.37 by the third principal stress σ_{III} ranging from -84.4 MPa to -14.5 MPa. Inspecting the different components of the stress tensor reveals that the in-plane stresses are one to two orders higher than the out-of-plane stress components which are thus not shown here. Figures 4.38(σ_{11}) and 4.39(σ_{22}) illustrate the compressive character of the normal stresses σ_{11} (-76.4 MPa to -3.8 MPa) and σ_{22} (-84.4 MPa to -3.9 MPa). In Fig. 4.40 we find the shear stress σ_{12} in the cells to range from -14.3 MPa to 13.9 MPa. In the mid-planes of the EVA layers the absolute values of the stresses are very low. However, large strains are present in the EVA at -40°C as is shown in Figs. 4.43, 4.42 and 4.41 where the first principal strain ε_I is shown. The highest values
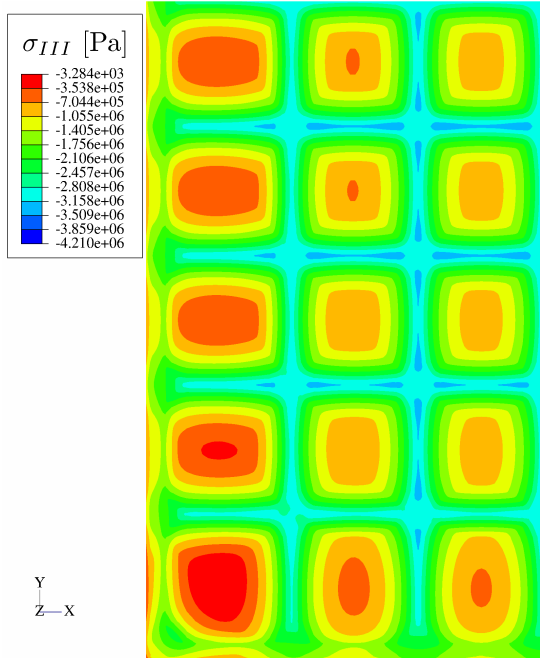
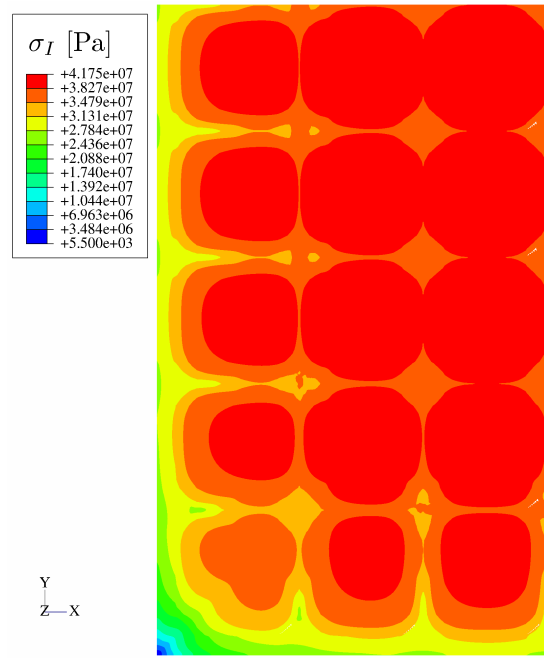Figure 4.34: Third principal stress σ_{III} in the mid-plane of the glass at -40°C.

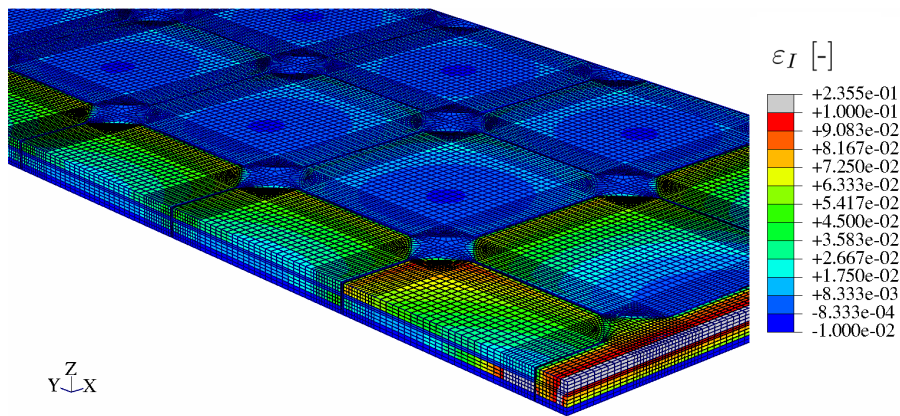Figure 4.35: First principal stress σ_I in the mid-plane of the back sheet at -40°C.

Figure 4.36: First principal strain ε_I at -40°C. The structure is scaled in z-direction and glass on top is hidden. The front surface is a yz-cutting plane through the centers of the solar cells in the left column of module.

71

are found in the layer between the cells and the back sheet exceeding 18% tensile strain (Fig. 4.43). The strain in the EVA between the glass and the solar cells is significantly lower, reaching 7% strain (Fig. 4.43). In each of the mentioned figures the local influence of the solar cells is visible. The maximum compressive stress in the glass arises at the gap between the cells whereas under the cells that are close the module edges the stress is close to zero ($\sigma_{III} = -0.003$ MPa, Fig. 4.34). In the back sheet, the tensile stress increases when moving to the center of the module (Fig. 4.35). Additionally this increase is superimposed by a stress increase in the back sheet towards the center of each solar cell. In the solar cells themselves the stress distribution is similar for all cells as it increases towards the center of each cell but the stress amplitudes decrease when moving from the module edges to the module center (Figs. 4.37-4.40). The position of a solar cell in the module is thus relevant for the level of stress in the cell. In the strain distribution of the EVA the footprint of the solar cells is clearly visible as well (Fig. 4.41 and 4.43).

For the other temperatures 25°C and 85°C the distributions of stresses and strains in the material layers exhibit similar characteristics but are significantly lower in their absolute values. For theses temperatures the difference to the stress free state at 150°C is still negative but smaller than to the state of -40°C so that the compressive character of the cell stresses remains as well as the tensile character of the stresses in the back sheet.

Discussion

The glass, which makes 72% of the module thickness and which has a high mechanical stiffness of 73 GPa, dominates the contraction of the module. Thereby it forces the laminated layers to follow the pure thermal shrinkage of the glass. The back sheet on the rear side can thus not contract as much as its high CTE ($\alpha_{\text{back sheet}} \gg \alpha_{\text{glass}}$) demands, thereby leading to the large tensile stress. We discuss this fact in more detail with the help of the definitions given in Subsections 2.1.3 and 2.1.4 and keep in mind that the total strain $\boldsymbol{\varepsilon}$ is continuous in the complete module structure due to continuous displacements $\boldsymbol{u}$ while the stress $\boldsymbol{\sigma}$ is not. The absolute value of the pure thermal strain $|\varepsilon_{\text{th}}|$ is higher than the total strain $|\varepsilon|$ in the back sheet by which it actually contracts. Both strains are negative, which leads to a positive mechanical strain $\varepsilon_{\text{mech}} = \varepsilon - \varepsilon_{\text{th}}$. It is the mechanical strain that determines the stress, i.e. $\sigma = E \varepsilon_{\text{mech}}$, so that we obtain tensile stress $\sigma > 0$ in the linear elastic back sheet. The tensile stress in the back sheet becomes lower at the module edges because the back sheet is in these regions only held by 1.2 mm thick EVA to the glass. There, the large strain of the compliant EVA allows a larger contraction of the back sheet and thus less mechanical strain.

The tensile character of the back sheet sets the glass under slight compression because the boundary condition forces the glass to remain planar and prohibits possible bending. The compression in the glass is extremal at the cell edges because there the tensile strain of the back sheet and the closing of the gap have a very local effect on the glass. The solar cells contract much less than the back sheet and, from a glass persective, they thereby buffer the higher compressive strains that originate from the back sheet. In between the cells this buffer layer is interrupted so that the compressive strains reach into the glass.

The solar cells exhibit the lowest CTE of the module materials. The cells contract thus less than the glass on top and less than the back sheet under the cells. The cells are forced to shrinks more than the pure thermal strain ($|\varepsilon| > |\varepsilon_{\text{th}}|$) which leads to negative mechanical strain. As silicon is a stiff material we obtain high compressive stress in the solar cells.

The EVA takes the function of a compliant buffer layer. The consequence is the large strain in the EVA layers.

4.4.3 Gap displacements

In the previous subsection we found the stresses and strains in the module to depend on their local position in xy-plane. It is thus not possible to reproduce the results above by a 'unit module', i.e.
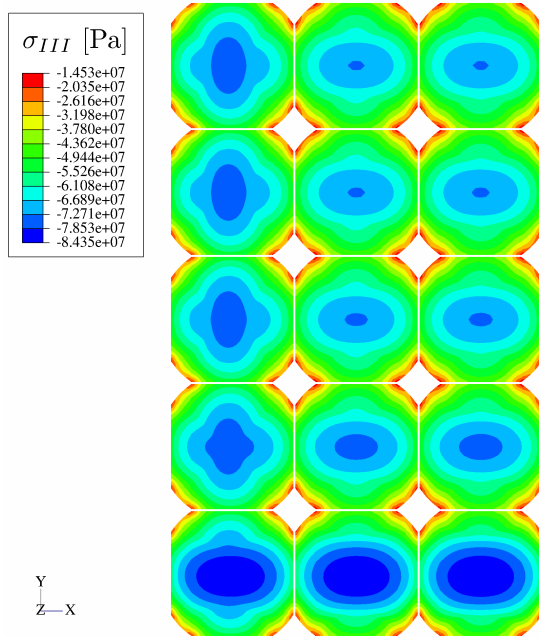
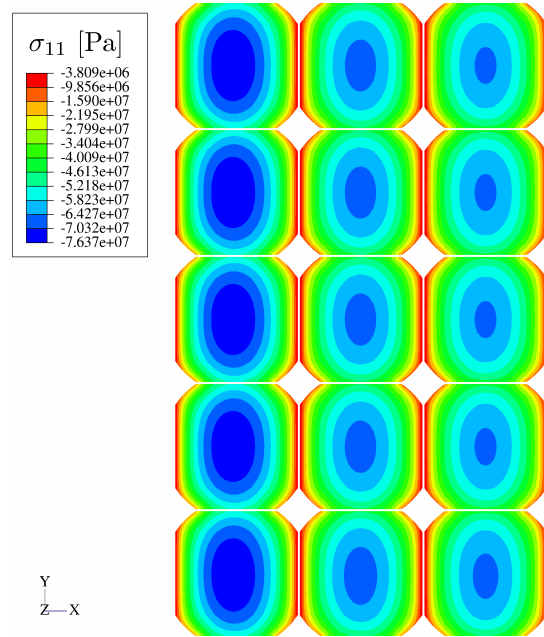Figure 4.37: Third principal stress σ_{III} in the mid-plane of the solar cells at -40°C.

Figure 4.38: Normal stress in x-direction σ_{11} in the mid-plane of the solar cells at -40°C.
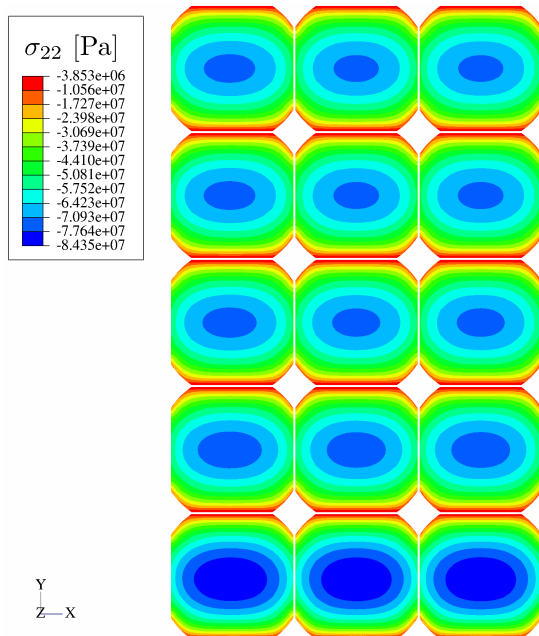

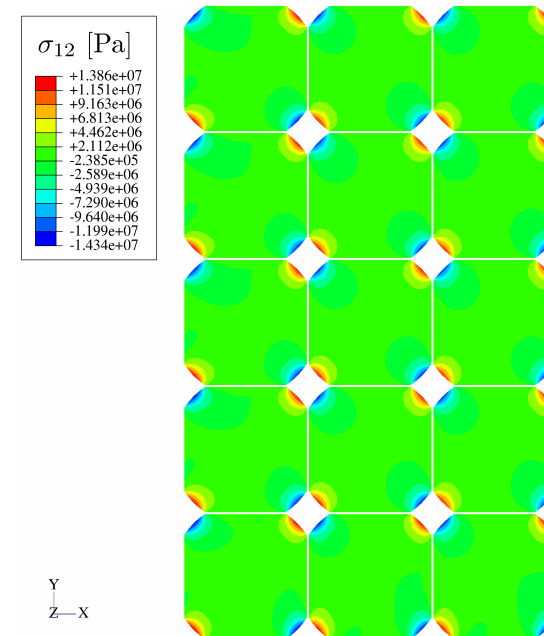Figure 4.39: Normal stress in y-direction σ_{22} in the mid-plane of the solar cells at -40°C.

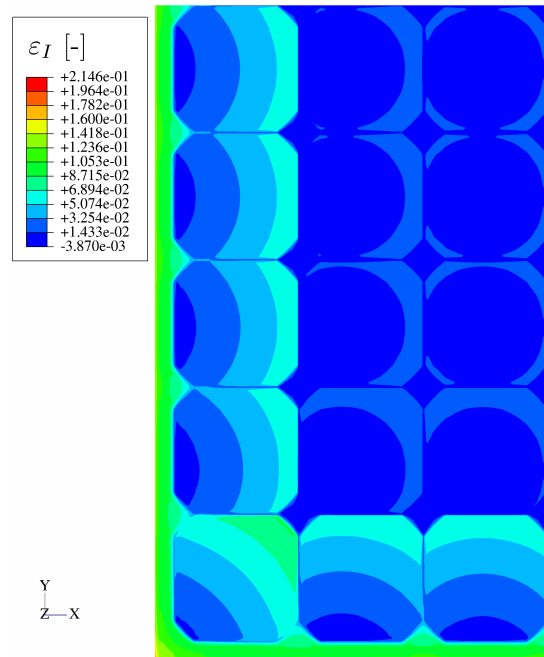Figure 4.40: Shear stress in the xy-plane σ_{12} in the mid-plane of the solar cells at -40°C.

Figure 4.41: First principal strain ε_I in the EVA between the glass and the cells at -40°C.
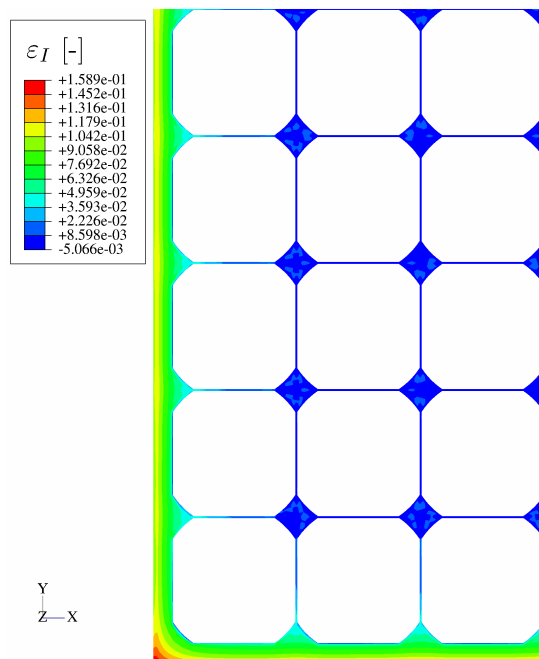
Figure 4.42: First principal strain ε_I in the EVA in the layer of the cells at -40°C.
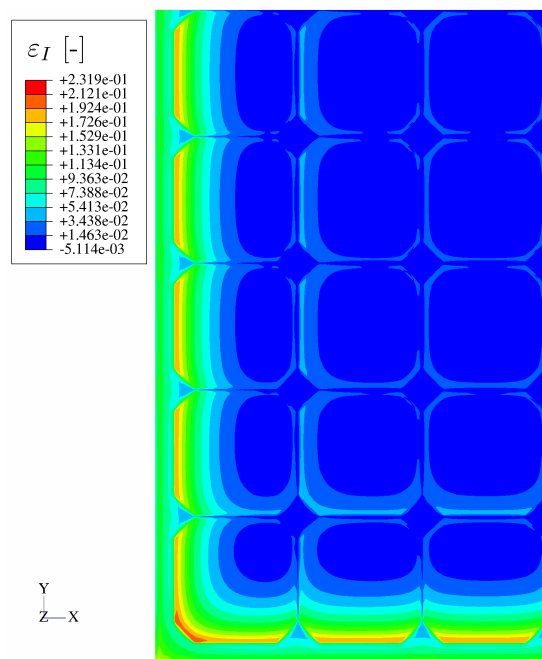
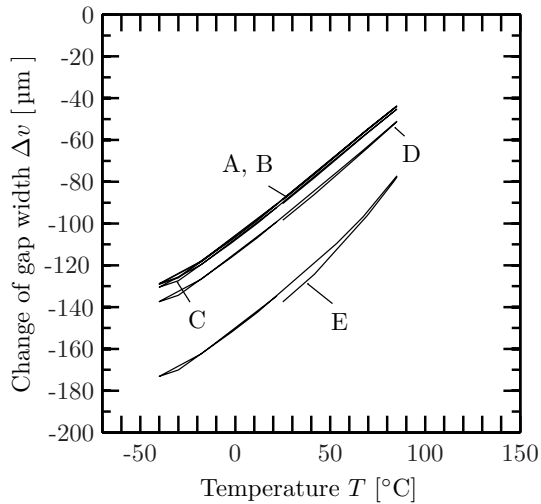Figure 4.43: First principal strain ε_I in the EVA between the back sheet and the cells at -40°C.

Figure 4.44: Change of the cell gaps at positions A to E from Fig. 4.33 during the temperature cycle shown in Fig. 4.32.
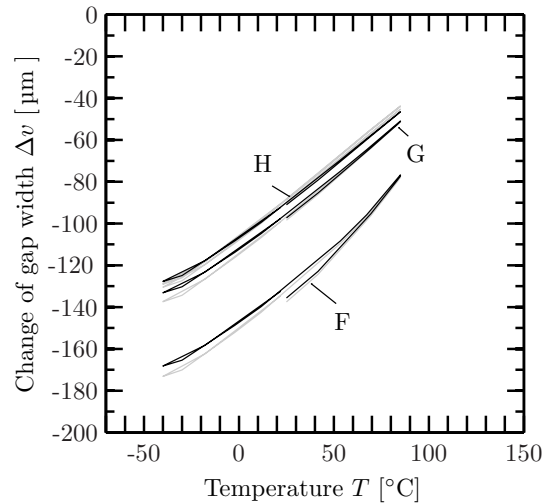
Figure 4.45: Change of the cell gaps at positions F to H (black) compared to positions A to E (gray) during the temperature cycle.

a geometrical subset of a complete module that should give universally valid results. Consequently, the question arises whether the gap displacement is also dependent on the position of the gap in the module. We therefore inspect the gap displacement along the left column and the bottom row of cells indicated by the 8 positions from A to H in Fig. 4.33. Figure 4.44 shows these gap displacements for the positions A to E during temperature cycling. Not all curves coincide so that we find a significant dependence of the gap displacement on the position of the gap in the module. The gap in positions A and B shrinks by 180 μm at -40°C compared to the initial gap length of 2 mm and zero gap displacement at 150°C. The further the gap position is away from the central axis of the module the larger is the change of the gap during the thermal cycle. The gap E exhibits the largest change which reaches 180 μm at -40°C compared to 150°C. Furthermore, we find an offset in the curves for the temperature of 25°C which is highest for the gap E with 5 μm. In Fig. 4.45 we compare these results to the gap displacements at positions F to H. It is found that the 3 curves are in the same region than the 5 curves A to E so that H coincides with A and B while F coincides with E.

These results clarify that the position of the cell gap in the module is highly relevant for the gap displacement meaning less activities in the cell gaps which are closest to the central axes of the module and a higher gap displacement for the cell in the corner. For standard modules we may thus expect that the interconnectors are most stressed at the top and bottom cells of the module. The offset in the gap displacement curves is due to the viscoelasticity of the EVA as all other materials are modeled by fully reversible elasticity. It is thus the viscoelasticity of the EVA that causes one temperature cycle to slightly shift the cells apart from each other. This effect is obviously more relevant for the cells at the module edges.

Summary and outlook

In this work the thermomechanics of crystalline PV modules are investigated. We therefore set up mechanical material models for every module component and evaluate the quality of the model by comparing the FEM-simulations to experiments performed with specially designed laminate structures. We then use the material model with best agreement to the experimental data to calculate the stress and strain distribution in a 60 cell module with non-interconnected solar cells.

We use linear elastic material models for the substrate glass, the solar cells and the back sheet. For glass, we rely on literature data except for the CTE which we measure to be 7.8×10^{-6} 1/K. The 3-point bending test is used to compare the Young's modulus of RISE-EWT solar cells to bulk silicon. We find a reasonable agreement between the experimentally determined values for E and the literature data. The groove structure of the RISE-EWT cells features a nonhomogeneous thickness that varies by $\pm 10 \, \mu$m. Including this thickness range in the experimental analysis leads to a 30 GPa-wide range for the Young's modulus that includes the theoretical value of 130 GPa in 14 out of 15 tests. We thus decide to model monocrystalline silicon solar cells with an anisotropic stiffness matrix for bulk silicon. The back sheet and the EVA are tensile tested at -40°C, 20°C and 80°C thus measuring the Young's modulus and Poisson's ratio. In particular the EVA exhibits a vast dependency of the Young's modulus on temperature, which is between 6.5 MPa and 2.1 GPa. The dynamic mechanical analysis is a well suited technique to determine the Young's modulus or the shear modulus as a function of the temperature.

In addition, we find the EVA to depend on time so that we set up a viscoelastic material model consisting of a generalized Maxwell model with WLF parameters for the time-temperature-superposition. The model is constructed from a series of tensile relaxation and creep tests where we monitor the force, the temperature, the tensile and the transverse strain. In order to obtain shear relaxation data we apply an interconversion technique where we use Tikhonov's regularization. We first demonstrate that this regularization is applicable for non-equidistant points in time. The viscoelastic model consists of 26 Maxwell arms with relaxation times between 10^{-3} and 10^{22}.

With a first demonstration of the digital image correlation technique in the field of PV module technology we prove this contactless method to measure the gap displacement between laminated cells with an accuracy of $1.4 \, \mu$m as we reported in [39]. In the laminate experiments with three solar cells we determine the gap displacement to be approximately $0.5 \, \mu$m/°C. A first investigation of borosilicate glass on the gap displacement reveals that the gap reduction may be eliminated by matching the CTE of the glass and the solar cells.

This experimental observation is confirmed by simulations where a variation of the CTE of glass has the largest impact on the gap displacement. However, to reproduce the experimental data of the gap displacement, an accurate mechanical model for EVA is essential. We find the viscoelastic model for EVA to give the best agreement with the measured data ($\pm 12 \, \mu$m) while the linear elastic and the temperature-dependent linear elastic model do not reproduce the shape of the experimental data.

In a 3-dimensional FEM-simulation of a 60 cell module without interconnects over one temperature cycle we identify the stresses in the solar cells to be compressive with σ_{III} between -84.4 MPa and

-14.4 MPa at -40°C. The back sheet is under tension with σ_I reaching 41.7 MPa. The EVA takes the function of a compliant buffer layer with large strains that exceed 18%. All module materials experience higher stress and strain values at the edges of the module. The footprint of the solar cells is visible in the stress and strain distribution of all material layers. In the investigation of the simulated gap displacements we find a dependency on the position of the gap in the module. The further the gap is located from the mid-axis of the module, the higher are the gap displacements. The gap next to the cell in the corner shrinks by 180 µm (-40°C) compared to zero displacement at lamination temperature of 150°C while the gap displacement in the mid-axis of the module is -130 µm at -40°C. Furthermore, the offset in the gap displacement at 25°C which is 5 µm for the gap in the corner of the module originates from the viscoelastic material behaviour of EVA. For an optimal interconnection design these different gap displacements have to be taken into account, i.e. maintaining purely elastic strains of the copper ribbon when the gap decreases by 180 µm.

In future research the impact of the standard interconnection technique may be included in the simulation models to determine the stresses that are generated by the standard concept. Therefore the simulation has to be split into two parts. First, a modeling of the soldering process with subsequent cooling and second the simulation of the lamination step with the prestressed interconnected cell strings as initial configuration. It would be a large step towards a complete understanding of the complex mechanical behavior of a PV module if the simulation includes the creation of stresses that start to build up in the soldering process. With the material models and parameters provided in this work the impact of thinner cells or other material choices can already be studied in more detail aiming to develop mechanically stable future module concepts. By simply modifying the boundary conditions the FEM-model presented in this work can also be used to simulate module bending and oscillation. The material model for EVA can be improved by measuring at intermediate temperatures to create a denser mastercurve. The dynamic mechanical analysis is a well suited tool to efficiently measure such viscoelastic material parameters and reduces the experimental effort in comparison to the relaxation and creep tests performed in this work. More attention has to be drawn to the specific material properties of the solar cells to improve the comparison with bulk silicon data, for example taking into account the cell bow after firing, a multicrystalline structure instead of the monocrystalline structure or the impact of the front grid. In all these suggested topics the productive combination of experiment and simulation has to be preserved.

Bibliography

[1] IEC 61215:2005, *Crystalline silicon terrestrial photovoltaic (PV) modules - Design qualification and type approval.* International Electrochemical Commission, 2005.

[2] SOLON präsentiert mit dem neuen SOLON Black 280/12 das erste kristalline Modul zum Kleben für Metalldächer. `http://www.solon.com/de/presse/detail.html?ID=391`. Retrieved November 22, 2010.

[3] Global Market Outlook for Photovoltaics until 2014. Tech. rep., EPIA - European Photovoltaic Industry Association, May 2010.

[4] H. Altenbach, J. Altenbach and W. Kissing. *Mechanics of Composite Structural Elements.* Springer, 2004.

[5] H. Altenbach, J. Altenbach and K. Naumenko. *Ebene Flächentragwerke: Grundlagen der Modellierung und Berechnung von Scheiben und Platten.* Springer, 1998.

[6] H. Altenbach and K. Naumenko. *Höhere Technische Mechanik.* Script of Lecture at University of Halle, 2009.

[7] J. Althaus. Quality assurance for PV modules: experience from type approval testing. *Photovoltaics International*, vol. 3: pp. 120–127, 2009.

[8] R. D. Andrews and A. V. Tobolsky. Elastoviscous properties of polyisobutylene. IV. Relaxation time spectrum and calculation of bulk viscosity. *Journal of Polymer Science*, vol. 7(2-3): pp. 221–242, 1951.

[9] H. Balke. *Einführung in die Technische Mechanik: Festigkeitslehre.* Springer, 2008.

[10] H.-J. Bargel, G. Schulze, H. Hilbrans, K.-H. Hübner and O. Krüger. *Werkstoffkunde.* Springer, 2008.

[11] H. Behnken, M. Apel and D. Franke. Simulation of mechanical stress during bending tests for crystalline wafers. In: *Proceedings of 3rd World Conference on Photovoltaic Energy Conversion*, pp. 1308–1311. 2003.

[12] I. J. Bennett, P. C. de Jong, M. J. H. Kloos, C. N. J. Stam, A. Henckens, J. Schuermans, R. J. Gomez, P. Sánchez-Friera, B. Lalaguna and H. Schmidt. Low-stress interconnection of solar cells. In: *Proceedings of the 22nd European Photovoltaic Solar Energy Conference*, pp. 2674–2678. Milan, 2007.

[13] U. Blieske, T. Doege, P. Gayout, M. Neander, D. Neumann and A. Prat. Light-trapping in solar modules using extra-white textured glass. In: *Proceedings of 3rd World Conference on Photovoltaic Energy Conversion*, pp. 188 – 191. 2003.

[14] A. F. Bower. *Applied Mechanics of Solids.* CRC Press, 2009.

[15] R. Bradshaw and L. Brinson. A Sign Control Method for Fitting and Interconverting Material Functions for Linearly Viscoelastic Solids. *Mechanics of Time-Dependent Materials*, vol. 1: pp. 85–108, 1997.

[16] G. S. Brady, H. R. Clauser and J. A. Vaccari. *Materials Handbook.* McGraw-Hill Professional, 2002.

[17] D. Braess. *Finite Elemente: Theorie, schnelle Löser und Anwendungen in der Elastizitatstheorie.* Springer, 2003.

[18] R. Brueckner. *Materials Science and Technology: A Comprehensive Treatment, Vol. 9, Glasses and Amorphous Materials*, chap. Mechanical properties of Glasses. Wiley-VCH, 1991.

[19] M. Cable. *Materials Science and Technology: A Comprehensive Treatment, Vol. 9, Glasses and Amorphous Materials*, chap. Classical Glass Technology. Wiley-VCH, 1991.

[20] W. Carroll, E. Cuddihy and M. Salama. Material and design considerations of encapsulants for photovoltaic arrays in terrestrial applications. In: *Proceedings of the 12th IEEE PVSC*, pp. 332–339. Baton Rouge, 1976.

[21] C. Carter and M. Norton. *Ceramic Materials: Science and Engineering.* Springer, 2007.

[22] R. Christensen. *Mechanics of Composite Materials.* Dover Publications, 2005.

[23] F. Clement, M. Menkoe, T. Kubera, C. Harmel, R. Hoenig, W. Wolke, H. Wirth, D. Biro and R. Preu. Industrially feasible multi-crystalline metal wrap through (MWT) silicon solar cells exceeding 16% efficiency. *Solar Energy Materials and Solar Cells*, vol. 93(6-7): pp. 1051–1055, 2009.

[24] Comsol AB. *Comsol Multiphysics User's Guide*, 2008.

[25] N. L. Corvec and T. R. Walter. Volcano spreading and fault interaction influenced by rift zone intrusions: Insights from analogue experiments analyzed with digital image correlation technique. *Journal of Volcanology and Geothermal Research*, vol. 183(3-4): pp. 170–182, 2009.

[26] E. Cuddihy. Development of reduced-variable master curves for estimating tensile stresses of encapsulated solar cells caused by module deflection or thermal expansion. Tech. rep., Jet Propulsion Laboratory, 1981.

[27] E. Cuddihy, W. Carroll, C. Coulbert, A. Gupta and R. H. Liang. Photovoltaic module encapsulation design and materials selection, volume 1. Tech. rep., Jet Propulsion Laboratory, 1982.

[28] E. Cuddihy, C. Coulbert, A. Gupta and R. Liang. Flat-plate solar array project. Volume 7: Module encapsulation. Tech. rep., Jet Propulsion Laboratory, 1986.

[29] A. W. Czanderna and F. J. Pern. Encapsulation of PV modules using ethylene vinyl acetate copolymer as a pottant: A critical review. *Solar Energy Materials and Solar Cells*, vol. 43(2): pp. 101–181, 1996.

[30] Dassault Systemes. *Abaqus/CAE User Manual 6.10*, 2010.

[31] R. J. Davies, S. J. Eichhorn, J. A. Bennett, C. Riekel and R. J. Young. Imaging microstructure and stress fields within a cross-ply composite laminate. *Composites Science and Technology*, vol. 69(5): pp. 567–574, 2009.

[32] A. B. de Castro. *Continuum Thermomechanics.* Birkhäuser Basel, 2005.

[33] P. de Jong. Achievements and challenges in crystalline silicon back-contact module technology. *Photovoltaics International*, vol. 7: pp. 138–144, 2010.

[34] S. Dietrich, M. Pander and M. Ebert. Mechanical Challenges of PV - Modules and its Embedded Cells - Experiment and Finite Element Analysis. In: *Proceedings of the 24th European Photovoltaic Solar Energy Conference*, pp. 3427–3431. Hamburg, 2009.

[35] G. Ehrenstein. *Polymer-Werkstoffe. Struktur - Eigenschaften - Anwendung.* Hanser Fachbuch, 1999.

[36] D. Eikelboom, J. Bultman, A. Schoenecker, M. Meuwissen, M. van den Nieuwenhof and D. Meier. Conductive adhesives for low-stress interconnection of thin back-contact solar cells. In: *Proceedings of the International Conference PV in Europe*, pp. 291–294. Rome, 2002.

[37] U. Eitner, P. P. Altermatt, M. Köntges, R. Meyer and R. Brendel. A modeling approach to the optimization of interconnects for back contact cells by thermomechanical simulations of photovoltaic modules. In: *Proceedings of the 23rd European Photovoltaic Solar Energy Conference*, pp. 2815–2817. Valencia, 2008.

[38] U. Eitner, M. Köntges and R. Brendel. Measuring thermomechanical displacements of solar cells in laminates using digital image correlation. In: *Proceedings of the 34th IEEE PVSC*, pp. 1280–1284. Philadelphia, 2009.

[39] U. Eitner, M. Köntges and R. Brendel. Use of digital image correlation technique to determine thermomechanical deformations in photovoltaic laminates: Measurements and accuracy. *Solar Energy Materials and Solar Cells*, vol. 94(8): pp. 1346–1351, 2010.

[40] I. Emri and N. Tschoegl. Generating line spectra from experimental responses. Part I: Relaxation modulus and creep compliance. *Rheological Acta*, vol. 32: pp. 311–322, 1993.

[41] P. Engelhart. *Lasermaterialbearbeitung als Schlüsseltechnologie zum Herstellen rückseitenkontaktierter Siliciumsolarzellen.* Ph.D. thesis, Gottfried Wilhelm Leibniz Universität Hannover, 2007.

[42] P. Engelhart, N.-P. Harder, A. Merkle, R. Grischke, R. Meyer and R. Brendel. RISE: 21.5% efficient back junction silicon solar cells with laser technology as a key processing tool. In: *Proceedings of the 4th World Conference on Photovoltaic Energy Conversion*, pp. 773–776. Hawaii, 2006.

[43] P. Engelhart, A. Teppe, A. Merkle, R. Grischke, R. Meyer, N.-P. Harder and R. Brendel. The RISE-EWT Solar Cell - A new approach towards simple high efficiency silicon solar cells. In: *Technical Digest of the 15th International Photovoltaic Science and Engineering Conference*, pp. 802–803. Shanghai, 2005.

[44] J. D. Ferry. *Viscoelastic Properties of Polymers.* Wiley, 1980.

[45] M. Gast, M. Köntges and R. Brendel. Lead-free on-laminate laser soldering: a new module assembling concept. *Progress in Photovoltaics: Research and Applications*, vol. 16(2): pp. 151–157, 2008.

[46] J. Gee, S. Garrett and W. Morgan. Simplified module assembly using back-contact crystalline-silicon solar cells. In: *Proceedings of the 26th IEEE PVSC*, pp. 1085–1088. Anaheim, 1997.

[47] J. Gee, D. Meakin, S. Southimath, M. Spath and I. Bennett. Development of commercial-scale photovoltaic modules using monolithic module assembly. In: *Proceedings of the 34th IEEE PVSC*, pp. 2133–2137. Philadelphia, 2009.

[48] A. Goetzberger, B. Voß and J. Knobloch. *Sonnenenergie: Photovoltaik. Physik und Technologie der Solarzelle.* Teubner, 1997.

[49] M. A. Green. *Solar Cells : Operating Principles, Technology and System Applications.* University of New South Wales, 1986.

[50] M. A. Green. *Silicon Solar Cells Advanced Principles and Practice.* Centre Photovoltaic Devices&Systems, 1995.

[51] J. C. Greenwood. Silicon in mechanical sensors. *Journal of Physics E: Scientific Instruments*, vol. 21(12): pp. 1114–1128, 1988.

[52] W. Grellmann. *Polymer Testing.* Carl Hanser, 2007.

[53] R. Greve. *Kontinuumsmechanik: Ein Grundkurs für Ingenieure und Physiker.* Springer, 2003.

[54] D. Gross, W. Hauger and W. Schnell. *Technische Mechanik 1: Statik.* Springer, 2002.

[55] D. Gross, W. Hauger and W. Schnell. *Technische Mechanik 2: Elastostatik.* Springer, 2002.

[56] D. Gross, W. Hauger and P. Wriggers. *Technische Mechanik 4: Hydromechanik, Elemente der Höheren Mechanik, Numerische Methoden.* Springer, 2009.

[57] G. Habenicht. *Kleben: Grundlagen, Technologien, Anwendungen.* Springer, 2006.

[58] B. Han and D. Post. *Springer Handbook of Experimental Solid Mechanics*, chap. Geometric Moiré, pp. 601–626. Springer, 2008.

[59] H. Häberlin. *Photovoltaik: Strom aus Sonnenlicht für Verbundnetz und Inselanlagen.* Electrosuisse, 2010.

[60] E. Hornbogen and H. Warlimont. *Metalle: Struktur und Eigenschaften der Metalle und Legierungen.* Springer, 2006.

[61] P. Ifju. *Springer Handbook of Experimental Solid Mechanics*, chap. Composite Materials, pp. 97–124. Springer, 2008.

[62] B. Ilschner and R. Singer. *Werkstoffwissenschaften und Fertigungstechnik: Eigenschaften, Vorgänge, Technologien.* Springer, 2004.

[63] G. Jorgensen, K. Terwilliger, J. DelCueto, S. Glick, M. Kempe, J. Pankow, F. Pern and T. McMahon. Moisture transport, adhesion, and corrosion protection of PV module packaging materials. *Solar Energy Materials and Solar Cells*, vol. 90(16): pp. 2739 – 2775, 2006.

[64] D. Karalekas, J. Cugnoni and J. Botsis. Monitoring of hygrothermal ageing effects in an epoxy resin using FBG sensor: A methodological study. *Composites Science and Technology*, vol. 69(3-4): pp. 507–514, 2009.

[65] L. L. Kazmerski. Photovoltaics: A review of cell and module technologies. *Renewable and Sustainable Energy Reviews*, vol. 1(1-2): pp. 71–170, 1997.

[66] L. L. Kazmerski. Solar photovoltaics R&D at the tipping point: A 2005 technology overview. *Journal of Electron Spectroscopy and Related Phenomena*, vol. 150(2-3): pp. 105–135, 2006.

[67] M. Kempe. Design criteria for photovoltaic back-sheet and front-sheet materials. *Photovoltaics International*, vol. 2: pp. 100–104, 2008.

[68] M. Kempe. Evaluation of encapsulant materials for PV applications. *Photovoltaics International*, vol. 9: pp. 170–176, 2010.

[69] E. V. Kerschaver and G. Beaucarne. Back-contact solar cells: a review. *Progress in Photovoltaics: Research and Applications*, vol. 14(2): pp. 107–123, 2006.

[70] R. Kienzler and R. Schröder. *Einführung in die Höhere Festigkeitslehre.* Springer, 2009.

[71] D. L. King, M. A. Quintana, J. A. Kratochvil, D. E. Ellibee and B. R. Hansen. Photovoltaic module performance and durability following long-term field exposure. *Progress in Photovoltaics: Research and Applications*, vol. 8: p. 241–256, 2000.

[72] B. Klein. *FEM*. Vieweg+Teubner Verlag, 2007.

[73] W. Knauss, I. Emri and H. Lu. *Springer Handbook of Experimental Solid Mechanics*, chap. Mechanics of Polymers: Viscoelasticity, pp. 49–96. Springer, 2008.

[74] R. S. Lakes. Viscoelastic measurement techniques. *Review of Scientific Instruments*, vol. 75(4): pp. 797–810, 2004.

[75] P. Lall, D. Iyengar, S. Shantaram, P. Gupta, P. D. and S. J. Feature extraction and health monitoring using image correlation for survivability of leadfree packaging under shock and vibration. In: *Proceedings of the 9th International Conference on Thermal, Mechanical and Multi-Physics Simulation and Experiments in Microelectronics and Microsystems (EuroSimE)*, pp. 594–608. Freiburg, 2008.

[76] A. Luque and S. Hegedus (editors). *Handbook of Photovoltaic Science and Engineering*. Wiley, 2003.

[77] K. G. Lyon, G. L. Salinger, C. A. Swenson and G. K. White. Linear thermal expansion measurements on silicon from 6 to 340 K. *Journal of Applied Physics*, vol. 48(3): pp. 865–868, 1977.

[78] C. Macosko. *Rheology: Principles, Measurements and Applications*. VHC Publishers, 1994.

[79] D. W. Mead. Numerical interconversion of linear viscoelastic material functions. *Journal of Rheology*, vol. 38(6): pp. 1769–1795, 1994.

[80] R. Meier, F. Kraemer, S. Schindler and S. W. J. Bagdahn. Thermal and mechanical induced loading on cell interconnectors in crystalline photovoltaic modules. In: *Proceedings of the 25th European Photovoltaic Solar Energy Conference*, pp. 3740–3744. Valencia, 2010.

[81] R. Meier, F. Kraemer and S. Wiese. Thermo-Mechanical Behaviour of Copper-Ribbon Materials. In: *Proceedings of the 24th European Photovoltaic Solar Energy Conference*, pp. 3413–3419. Hamburg, 2009.

[82] G. Menges, E. Haberstroh, W. Michaeli and E. Schmachtenberg. *Werkstoffkunde Kunststoffe*. Hanser Fachbuch, 2002.

[83] M. Merkel and A. Öchsner. *Eindimensionale Finite Elemente: Ein Einstieg in die Methode*. Springer, 2010.

[84] B. Metz, O. Davidson, P. Bosch, R. Dave and L. M. (editors). *Climate change 2007: Working group III: Mitigation of climate change*. Tech. rep., IPCC (Intergovernmental panel on climate change), 2007.

[85] E. Moeller (editor). *Handbuch Konstruktionswerkstoffe*. Hanser Fachbuchverlag, 2008.

[86] P. Morgensen, E. Mahe, U. Blieske, M. Neander, R. Toelle and J. Palm. Large area glass coating for thin film CIGS module production. In: *Proceedings of the 19th European Photovoltaic Solar Energy Conference*, pp. 1905–1908. Paris, 2004.

[87] MSC.Software Corporation. *MSC.Marc User's Guide*, 2003.

[88] M. Neander, F. Gromball, D. Neumann, N.-P. Harder and W. A. Nositschka. Anti-Reflective-Coating Tuned for Higher Solar Module Voltage. In: *Conference Record of the 2006 IEEE 4th World Conference on Photovoltaic Energy Conversion*, vol. 2, pp. 2070 –2072. 2006.

[89] L. Nielsen and R. Landel. *Mechanical Properties of Polymers and Composites*. Marcel Dekker, Inc., 1994.

[90] A. Nikonov, A. R. Davies and I. Emri. The determination of creep and relaxation functions from a single experiment. *Journal of Rheology*, vol. 49(6): pp. 1193–1211, 2005.

[91] N. Noda, R. Hetnarski and Y. Tanigawa. *Thermal Stresses*. Taylor & Francis, 2002.

[92] J.-J. Orteu. 3-D computer vision in experimental mechanics. *Optics and Lasers in Engineering*, vol. 47(3-4): pp. 282–291, 2009. Optical Measurements.

[93] M. Osborne. Developments in high throughput integrated cell connection equipment. *Photovoltaics International*, vol. 3: pp. 128–131, 2009.

[94] M. Osborne. Trends and developments in the lamination process of PV modules (part 1). *Photovoltaics International*, vol. 5: pp. 160–164, 2009.

[95] M. Osborne. Trends and developments in the lamination process of PV modules (part 2). *Photovoltaics International*, vol. 6: pp. 140–145, 2009.

[96] W. Osten. *Springer Handbook of Experimental Solid Mechanics*, chap. Digital Image Processing for Optical Metrology, pp. 481–564. Springer, 2008.

[97] C. R. Osterwald and T. J. McMahon. History of accelerated and qualification testing of terrestrial photovoltaic modules: A literature review. *Progress in Photovoltaics: Research and Applications*, vol. 17: pp. 11–33, 2009.

[98] J. Pang, X. Shi, X. Zhang and Q. Liu. Application of digital speckle correlation to microdeformation measurement of a flip chip assembly. In: *Proceedings of 53rd Electronic Components and Technology Conference*, pp. 926–932. New Orleans, 2003.

[99] T. Pintat, K. Wellinger and P. Gimmel. *Werkstofftabellen der Metalle*. Kröner, 2000.

[100] R. C. Progelhof and J. L. Throne. *Polymer Engineering Principles: Properties, Processes and Tests for Design*. Hanser Gardner Publications, 1993.

[101] Purvis. *Handbook of Industrial Materials*. Elsevier Science Ltd, 1992.

[102] R. B. Roberts. Thermal expansion reference data: silicon 300-850 K. *Journal of Physics D: Applied Physics*, vol. 14(10): pp. L163–L166, 1981.

[103] E. Roos and K. Maile. *Werkstoffkunde für Ingenieure: Grundlagen, Anwendung, Prüfung*. Springer, 2008.

[104] H. Salmang and H. Scholze. *Keramik*. Springer, 2006.

[105] SAS IP, Inc. *Ansys Workbench 12.0*, 2009.

[106] S. Schoenfelder, A. Bohne and J. Bagdahn. Comparison of test methods for strength characterization of thin solar wafers. In: *Proceedings of the 22th European Photovoltaic Solar Energy Conference*. Milan, 2007.

[107] T. Schreier-Alt. *Polymer encapsulation of mechatronic systems – Characterization by embedded Fibre Bragg Gratings*. Ph.D. thesis, Technische Universität Berlin, 2007.

[108] T. P. Seward and T. Vascott. *High Temperature Glass Melt Property Database for Process Modeling*. Wiley-American Ceramic Society, 2005.

[109] J. F. Shackelford and W. Alexander (editors). *CRC Materials Science and Engineering Handbook, Third Edition*. CRC Press, 2000.

[110] M. T. Shaw and W. J. MacKnight. *Introduction to Polymer Viscoelasticity*. Wiley-Interscience, 2005.

[111] A. Słuzalec. *Introduction to Nonlinear Thermomechanics: Theory and Finite-Element Solutions*. Springer, 1991.

[112] A. Słuzalec. *Theory of Thermomechanical Processes in Welding*. Springer, 2005.

[113] J. Sorvari and M. Malinen. Numerical interconversion between linear viscoelastic material functions with regularization. *International Journal of Solids and Structures*, vol. 44(3-4): pp. 1291 – 1303, 2007.

[114] J. Sorvari and M. Malinen. On the direct estimation of creep and relaxation functions. *Mechanics of Time-Dependent Materials*, vol. 11: pp. 143–157, 2007.

[115] E. Suhir. Predicted Bow of Plastic Packages of Integrated Circuit (IC) Devices. *Journal of Reinforced Plastics and Composites*, vol. 12(9): pp. 951–972, 1993.

[116] J. Suhling and P. Lall. *Springer Handbook of Experimental Solid Mechanics*, chap. Electronic Packaging Applications, pp. 1015–1044. Springer, 2008.

[117] M. Sutton. *Springer Handbook of Experimental Solid Mechanics*, chap. Digital Image Processing for Shape and Deformation Measurements, pp. 565–600. Springer, 2008.

[118] M. A. Sutton, J.-J. Orteu and H. Schreier. *Image Correlation for Shape, Motion and Deformation Measurements: Basic Concepts, Theory and Applications.* Springer, 2009.

[119] I. Tobias, C. del Canizo and J. Alonso. *Handbook of Photovoltaic Science and Engineering*, chap. Crystalline Silicon Solar Cells and Modules, pp. 255–306. Wiley, 2003.

[120] N. Tschoegl and I. Emri. Generating line spectra from experimental responses. Part II: Storage and loss functions. *Rheological Acta*, vol. 32: pp. 322–327, 1993.

[121] N. Tschoegl and I. Emri. Generating line spectra from experimental responses. Part IV: Application to experimental data. *Rheological Acta*, vol. 33: pp. 60–70, 1994.

[122] N. Tschoegl, W. Knauss and I. Emri. The Effect of Temperature and Pressure on the Mechanical Properties of Thermo- and/or Piezorheologically Simple Polymeric Materials in Thermodynamic Equilibrium – A Critical Review. *Mechanics of Time-Dependent Materials*, vol. 6: pp. 53–99, 2002.

[123] N. W. Tschoegl. *The Phenomenological Theory of Linear Viscoelastic Behavior: An Introduction.* Springer, 1989.

[124] W. D. van Driel, J. H. J. Janssen, G. Q. Zhang, D. G. Yang and L. J. Ernst. Packaging Induced Die Stresses - Effect of Chip Anisotropy and Time-Dependent Behavior of a Molding Compound. *Journal of Electronic Packaging*, vol. 125(4): pp. 520–526, 2003.

[125] J. E. Webb, D. I. Wilcox, K. L. Wasson and S. T. Gulati. Specialty thin glass for PV modules: mechanical reliability considerations. In: *Proceedings of the 24th European Photovoltaic Solar Energy Conference*, pp. 3253–3257. Hamburg, 2009.

[126] G. White. Thermal expansion of reference materials: copper, silica and silicon. *Journal of Physics D: Applied Physics*, vol. 6(17): pp. 2070–2078, 1973.

[127] S. Wiederhorn. Fracture Surface Energy of Glass. *Journal of the American Ceramic Society*, vol. 52(2): pp. 99–105, 1969.

[128] S. Wiese, R. Meier, F. Kraemer and J. Bagdahn. Constitutive behaviour of copper ribbons used in solar cell assembly processes. In: *Proceedings of the 6th International Conference on Thermal, Mechanical and Multi-Physics Simulation and Experiments in Microelectronics and Microsystems (EuroSimE)*, pp. 44–51. Delft, 2009.

[129] M. L. Williams, R. F. Landel and J. D. Ferry. The Temperature Dependence of Relaxation Mechanisms in Amorphous Polymers and Other Glass-forming Liquids. *Journal of the American Chemical Society*, vol. 77: pp. 3701–3707, 1955.

[130] A. S. Wineman and K. R. Rajagopal. *Mechanical Response of Polymers: An Introduction.* Cambridge University Press, 2000.

[131] J. Wohlgemuth, M. Conway and D. Meakin. Reliability and performance testing of photovoltaic modules. In: *Proceedings of the 28th IEEE PVSC*, pp. 1483–1486. 2000.

[132] J. Wohlgemuth and R. Petersen. Reliability of EVA modules. In: *Proceedings of the 23rd IEEE PVSC*, pp. 1090–1094. 1993.

[133] J. H. Wohlgemuth, D. W. Cunningham, N. V. Placer, G. J. Kelly and A. M. Nguyen. The effect of cell thickness on module reliability. In: *Proceedings of the 23rd IEEE PVSC*, pp. 1–4. 2008.

[134] P. Wriggers. *Nichtlineare Finite-Element-Methoden*. Springer, 2001.

[135] J. Wurm. *Glass Structures: Design and Construction of Self-supporting Skins*. Birkhäuser Basel, 2007.

[136] Z. Xia, D. Cunningham and J. H. Wohlgemuth. A new method for measuring cross-link density in ethylene vinyl acetate-based encapsulant. *Photovoltaics International*, vol. 5: pp. 150–159, 2009.

[137] D. Zhang and D. D. Arola. Applications of digital image correlation to biological tissues. *Journal of Biomedical Optics*, vol. 9(4): pp. 691–699, 2004.

[138] G. Zhang, W. van Driel and X. Fan. *Mechanics of Microelectronics*. Springer, 2006.

[139] O. C. Zienkiewicz and R. L. Taylor. *Finite Element Method*, vol. 1. Butterworth-Heinemann, 2000.

[140] O. C. Zienkiewicz and R. L. Taylor. *Finite Element Method*, vol. 2. Butterworth-Heinemann, 2000.

Danksagung

Lebenslauf

Persönliche Daten

Name	Ulrich Eitner
Adresse	Kissinger Str. 25, 40229 Düsseldorf
Geburtsdatum	1. Februar 1980 in Meerbusch
Staatsangehörigkeit	deutsch
Familienstand	verheiratet

Ausbildung

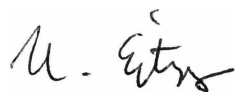|	
09/1986 - 06/1990	Kath. Grundschule Fuldaer Straße, Düsseldorf
08/1990 - 06/1999	St.-Ursula-Gymnasium, Düsseldorf (Abschluss: Abitur)
08/1996 - 01/1997	Austauschschüler an der Service High School, Anchorage, Alaska (USA)
08/1999 - 06/2000	Mobiler Sozialer Hilfsdienst bei den Johannitern, Düsseldorf
10/2000 - 08/2006	Studium der Diplom-Technomathematik
	an der Universität Karlsruhe (TH)
	Diplomarbeit am Institut für Technische Mechanik:
	"Ein Simulationsverfahren für die Mehrkörperdynamik
	mit Reibung und Stößen"
10/2003 - 06/2004	Studienjahr in Frankreich
	Mathématiques, Université Joseph Fourier, Grenoble

Berufstätigkeit

12/2006 - 01/2011	Institut für Solarenergieforschung Hameln (ISFH)
	Bereich PV-Modultechnik
	Wissenschaftlicher Mitarbeiter und Doktorand

Erklärung

Hiermit erkläre ich, dass ich meine Arbeit selbständig und ohne fremde Hilfe verfasst, andere als die von mir angegebenen Quellen und Hilfsmittel nicht benutzt und die den benutzten Werken wörtlich oder inhaltlich entnommenen Stellen als solche kenntlich gemacht habe.

Halle, den 21. Januar 2011

Ulrich Eitner